University of Alberta

The Field Line Resonance: Observation and Theory

by

France Rose Erna Fenrich ©

A thesis submitted to the Faculty of Graduate Studies and Research in partial fulfillment of the requirements for the degree of **Doctor of Philosophy**.

Department of Physics

Edmonton, Alberta

Spring 1997

National Library of Canada
Acquisitions and Bibliographic Services
395 Wellington Street
Ottawa ON K1A 0N4
Canada

Bibliothèque nationale du Canada
Acquisitions et services bibliographiques
395, rue Wellington
Ottawa ON K1A 0N4
Canada

Your file Votre référence

Our file Notre référence

The author has granted a non-exclusive licence allowing the National Library of Canada to reproduce, loan, distribute or sell copies of his/her thesis by any means and in any form or format, making this thesis available to interested persons.

The author retains ownership of the copyright in his/her thesis. Neither the thesis nor substantial extracts from it may be printed or otherwise reproduced with the author's permission.

L'auteur a accordé une licence non exclusive permettant à la Bibliothèque nationale du Canada de reproduire, prêter, distribuer ou vendre des copies de sa thèse de quelque manière et sous quelque forme que ce soit pour mettre des exemplaires de cette thèse à la disposition des personnes intéressées.

L'auteur conserve la propriété du droit d'auteur qui protège sa thèse. Ni la thèse ni des extraits substantiels de celle-ci ne doivent être imprimés ou autrement reproduits sans son autorisation.

0-612-21568-7

Canada

University of Alberta

Library Release Form

Name of Author: Frances Rose Erna Fenrich

Title of Thesis: The Field Line Resonance: Observation and Theory

Degree: Doctor of Philosophy

Year this Degree Granted: 1997

Permission is hereby granted to the University of Alberta Library to reproduce single copies of this thesis and to lend or sell such copies for private, scholarly, or scientific research purposes only.

The author reserves all other publication and other rights in association with the copyright in the thesis, and except as hereinbefore provided, neither the thesis nor any substantial portion thereof may be printed or otherwise reproduced in any material form whatever without the author's prior written permission.

Frances Fenrich

Department of Physics
University of Alberta
Edmonton, AB
T6G 2J1

Date: Nov 29, 1996

University of Alberta

Faculty of Graduate Studies and Research

The undersigned certify that they have read, and recommend to the Faculty of Graduate Studies and Research for acceptance, a thesis entitled **The Field Line Resonance: Observation and Theory** submitted by **Frances Rose Erna Fenrich** in partial fulfillment of the requirements for the degree of **Doctor of Philosophy.**

Dr. J. C. Samson, Supervisor

Dr. C. Capjack

Dr. M. Freeman

Dr. M. K. Hudson

Dr. G. Rostoker

Dr. W. Rozmus

Date: Nov 29, 1996

In loving memory of my father
Ralph Andrew Fenrich

Abstract

This thesis is an observational and theoretical study of field line resonances (FLRs) found to occur on magnetic shells in the Earth's magnetosphere. These resonances are actually standing shear Alfvén waves in the ultra-low frequency (ULF) regime, generated through mode coupling to fast compressional magnetohydrodynamic waves in the outer magnetosphere. FLRs may be signatures of fundamental processes by which energy is transported from the solar wind to the ionosphere and it is therefore important to study their characteristics and fully understand their generation mechanisms.

Numerous FLR events have been identified and analyzed using the Super Dual Auroral Radar Network (SuperDARN). This network is a system of high-frequency (HF) radars which provides a global-scale view of the plasma convection in the F-region of the high-latitude ionosphere. The oscillations in plasma flow associated with an FLR are superimposed upon the background convective flow and can be used to determine many characteristics of the FLR such as frequency, phase, location, and propagation velocities. A compilation of the observations has yielded some very interesting results. The most notable of these is that the FLRs repeatedly occur at the same discrete and stable frequencies, i.e. 1.3, 1.9, and 2.5 mHz, independent of local time and azimuthal wave number, m. They are also classifiable into two distinct types: those with small azimuthal wave number (m<17), and those with large azimuthal wave number (m>17). The fact that the two different wave types have numerous similarities is very important since it suggests that the same driving mechanism is responsible for the initiation of both types of resonance.

The apparent growth rates of the FLRs show a striking correlation with the

azimuthal wave number of the resonance. The observed high-*m* resonances have amplitudes that increase with time, indicating positive growth rates, while the low-*m* resonances have decreasing amplitudes, indicating negative growth rates. The resonance growth rates and latitudinal phase shifts, a decrease for low-*m* modes and an increase for high-*m* modes, are found to be determined by the direction of the Poynting flux in the system. In the case of the high-*m* resonance, an internal driver is present which is able to couple to the system and give Poynting flux out of the resonance region. The internal driver is most likely in the form of a wave-particle interaction.

The final portion of this thesis concerns the development of a theoretical model for the FLR driving mechanism. The most commonly accepted theory, the magnetospheric waveguide/cavity mode model, postulates that the magnetosphere acts as a waveguide or cavity which can generate a set of monochromatic fast wave eigenmodes which then couple to the FLRs. A review of this theory has shown that it falls short of explaining many of the experimental observations. Thus alternate theories capable of explaining the observations are explored. A new model, the magnetosheath waveguide model, is examined in detail and is shown to be very successful in its ability to explain the existence of the discrete FLRs.

Acknowledgment

I would like to thank my supervisor Dr. John Samson for giving me the opportunity to complete this PhD. He provided me with a very interesting and challenging project as well as the freedom to explore my own ideas. His support of my work and attendance at numerous international scientific meetings is greatly appreciated. I also extend thanks to the other members of my supervisory committee, Gordon Rostoker, Clarence Capjack, Wojciech Rozmus, and Mark Freeman as well as my external examiner Mary Hudson for their careful examination of my thesis and their useful comments.

The SuperDARN team of principle investigators, researchers, and technicians have done an exceptional job of making the Super Dual Auroral Radar Network a reality. Without their dedication and hard work, the data base for this study would not have existed. In particular I would like to thank George Sofko, PI for the Saskatoon HF radar, and Ray Greenwald, PI for the Goose Bay and Kapuskasing radars, for their support of my work. I would also like to acknowledge Mike McKibben, Dieter Andre´, Don Danskin, Kile Baker, Mike Ruohoniemi, and Bill Bristow who have been responsible for the day to day maintenance of hardware, software and data distribution. I also acknowledge the Natural Sciences and Engineering Research Council of Canada for their funding of the Canadian component of SuperDARN.

To all of my friends and colleagues in the space sciences lab over the years, Hamid Al Nashi, Karen Apps, Sherwood Botsford, Martin Connors, Peter Damiano, Sarah Derr, Eric Donovan, Erena Friedrich, Przemek Frycz, Barry Harrold, Terry Kolber, Christine Lesiak, William Liu, Sandy MacAuley, John Manuel, Robert Rankin, Susan Skone, Vladimir Tichonchuk, Beth Tooley, James Wanliss, and Igor Voronkov, I extend my warmest thanks for helping to make my time spent here very enjoyable as well as productive. I would like to give special thanks to the lab secretaries, Sarah and Beth, for their help with manuscript preparation and all the little day to day things; to Eric for his help with the field line mappings and his attempt to get me into kayaking; to Przemek and Vladimir for their views on the reverse phase problem; and to the current graduate students Igor, Erena, Peter, James, and Martin for their friendship and support. I must also thank Lynn Chandler, the graduate student secretary, for all her help throughout the years. She is an invaluable asset to the Physics Department.

The space sciences lab suffered a terrible loss with the sudden death of Dr. Barry Harrold. His contributions to my work are greatly appreciated. He had so much more

to offer both professionally and personally. I regret not taking the time to get to know Barry better both as a scientist and an individual. His dedication to his work is an inspiration to me.

I would also like to thank the Seal Clubbers, M C Magnets, and Dead Dogs slow pitch teams for the many enjoyable ball games throughout the years.

One of the most important parts of my life here in Edmonton has been my experience with the Edmonton Ice Elite Precision Skating Team. The team has provided me with a much needed escape from the world of graduate studies and research. To the team executive, my teammates, and especially my roomy, Michele Rowein, thanks for all the wonderful memories.

My sister Melinda, her husband Brad; my brother Mark and his wife Lois have always given me wonderful places to get away to. I cherish the time spent with my nieces and nephews, Dianne, Evan, Colby and Brianne. Words cannot express the thanks I owe my mother, Virginia, and my late father, Ralph, for all they have given me. They have always supported my education.

I must thank my best friend and fiance', Christian, for all his love and support. Many times he had to listen to my complaints and doubts and always had words of encouragement for me. Although he was lost when it came to "magnetohydrodynamics" he was still able to give me useful and constructive criticism of my work.

I gratefully acknowledge the Natural Sciences and Engineering Research Council of Canada and the University of Alberta for providing my financial support.

Table of Contents

Chapter **Page**

1 Introduction 1

1.1 Preliminary Remarks 1

1.2 Background and Theory 3

1.2.1 Basic Definitions and Concepts 3

1.2.1.1 The Solar Wind 4

1.2.1.2 The Magnetosphere 4

1.2.1.3 The Ionosphere 6

1.2.1.4 Space Plasmas 7

1.2.2. MHD Theory 9

1.2.2.1 One-Fluid Equations 11

1.2.2.2 Maxwell's Equations 12

1.2.2.3 Ohm's Law 13

1.2.2.4 Ideal MHD 14

1.2.2.5 Equation of State 14

1.2.2.6 Cold Plasma Approximation 15

1.2.2.7 Summary of One-Fluid MHD 15

1.2.2.8 MHD Plasma Waves 16

1.2.3 Field Line Resonance Coupling 20

1.2.4 Field Line Resonance Characteristics 28

1.2.5 Discussion of Previous Work on FLRs 31

2 Observations of Discrete Field Line Resonances Using The Super Dual Auroral Radar Network 34

2.1 Data Acquisition and Analysis Methods 34

2.2 Observations 44

2.3 Discussion 56

2.4 Summary 60

3 Growth and Decay of Field Line Resonances 62

3.1. Methods of Growth Rate Measurement 63

3.2. Results and Discussion 68

3.2.1. Low-m Case 69
3.2.2. High-m case 75
3.2.3. Wave-Particle Coupling 78
3.3. Summary 81

4 Discussion of Theoretical Models 83
4.1 Problems with the Magnetospheric Waveguide/Cavity Model 83
4.1.1 Plasma Density Problem 83
4.1.2 The Problem Concerning Large Azimuthal Wave Numbers 84
4.1.3 Stability Problem 87
4.2 Other Possible Models 88
4.3 The Magnetosheath Waveguide Model 90
4.3.1 Fast Wave Reflection at Magnetopause and Bow Shock 92
4.3.2 Boundary Conditions 94
4.3.3 Magnetosheath Eigenmode Solutions 95
4.3.4. Stability of Eigenmode Frequencies 98
4.3.5 Coupling of Magnetosheath Eigenmodes to FLRs 104
4.3.6 Success of Magnetosheath Waveguide Model 106

5 Concluding Remarks 107

Bibliography 111

Appendix A. Reflection and Transmission at a Perpendicular Shock 116

List of Tables

Table		Page
1.1	Some Typical Space Plasma Parameters	8
2.1	FLR Study Analysis Results	46
4.1	Parameters For Three Low-m FLRs	86

List of Figures

Figure		Page
1.1	Three dimensional view of the Earth's magnetosphere	3
1.2	Schematic of shear Alfvén wave	18
1.3	Schematic of fast compressional Alfvén wave	19
1.4	Box model of magnetosphere	20
1.5	Small k_y solution for E_x near resonance	25
1.6	Schematic of field line resonance coupling	26
1.7	(a) Resonance absorption versus coupling parameter, Q (b) Plot of Q versus azimuthal wave number, m	28
1.8	Phase and amplitude of E_x across resonance	30
1.9	Fundamental wave fields of a toroidal FLR	30
1.10	Magnetospheric waveguide model	32
2.1	Fields-of-view of the Super Dual Auroral Radar Network	35
2.2	Illustration of the scattering of VHF and HF signals by the ionosphere	36
2.3	Range-time plot of the line-of-sight Doppler velocity along beam 8 of Goose Bay for the time interval 0500-0900 UT on September 28, 1988	37
2.4	Range-time plot of the line-of-sight Doppler velocity along beam 10 of Saskatoon for the time interval 1900-2300 UT on October 18, 1993	37
2.5	Contour plots of 32-point FFT power spectra for various FLR events	38
2.6	Contour plots of 64-point FFT power spectra for various FLR events	39
2.7	Latitude profiles of the spectral power and phase for (a) a low-m event (b) a high-m event	40
2.8	Stack plot of the analytic signal amplitude envelopes for various beams of Kapuskasing (K) and Saskatoon (T) at the range gates where the 1.3-mHz resonance was at its maximum on October 18, 1993	42

2.9 Plot of phase versus longitude measured at 2120 UT for the1.3-mHz resonance of October 18, 1993 43

2.10 Plot of lag times of the resonance wave packet versus longitude for the 1.3-mHz resonance of October 18, 1993 43

2.11 Plot of the Saskatoon-Kapuskasing merge grid 45

2.12 Mappings of the azimuthal phase velocities to the equatorial plane for each of the resonances listed in Table 2.1 for
(a) a dipole model and
(b) the Tsyganenko 87 model 48

2.13 Number of occurrences observed to date for the various FLR frequencies 49

2.14 Analytic signal amplitude and frequency for the 1.9-mHz and 2.5-mHz resonances of two different events:
(a) February 2, 1994 (low-*m*), and
(b) October 6, 1993 (high-*m*) 50

2.15 Plot of the line of sight velocity amplitude versus radar beam direction for
(a) the 1.9 mHz low-*m* FLR on 28 Sept 1988;
(b) the 1.9 mHz high-*m* FLR on 18 Oct 1993 52

2.16 Plot of total velocity polarization ellipses at the resonance maximum for
(a) the 2.6 mHz low-*m* FLR on 2 Feb 1994;
(b) the 1.3 mHz high-*m* FLR on 18 Oct 1993 53

2.17 Merge of the band-passed line-of-sight Doppler velocity data from the Saskatoon and Kapuskasing radars for
(a) the 2.6 mHz low-*m* FLR on 2 Feb 1994;
(b) the 1.3 mHz high-*m* FLR 18 Oct 1993 55

2.18 Schematic diagram of the equatorial magnetosphere illustrating the general locations and propagation directions of the observed high- and low-*m* resonances 58

3.1 Stackplot of the band-passed uncorrected velocity time series data for the 2.5 mHz resonance on October 18, 1993 64

3.2 Plot of the resonance contour, estimated flow direction, and radar beam direction for the 2.5 mHz resonance observed on October 18, 1993 65

3.3 Plot of power vs time and the exponential fits for (a) a 2.2 mHz low-m resonance (b) a 2.5 mHz high-m resonance....67

3.4 Plot of power growth rate versus azimuthal wave number....68

3.5 Plot of the amplitude and phase of E_x near the resonance at $x=x_r=10\ R_E$ for the low-m case....72

3.6 Plot of the time averaged radial component of the Poynting vector versus radial position for (a) $\varepsilon < 0$ and (b) $\varepsilon > 0$....74

3.7 Plot of the amplitude and phase of E_x near the resonance at $x=x_r=10\ R_E$ for the low-m case with ε taken as positive....75

3.8 Plot of the amplitude and phase of E_x near the resonance at $x=x_r=10\ R_E$ for the high-m case....77

3.9 Plot of spectral power and phase versus latitude for the 1.3 mHz high-m resonance on 18 October, 1993....78

4.1 Magnetospheric waveguide frequency variation as a function of k_y....85

4.2 Plot of turning point as a function of k_y....86

4.3 Waveguide eigenfrequency as a function of magnetopause position....88

4.4 Schematic of magnetosheath waveguide model in the equatorial plane....91

4.5 Illustration of boundary conditions at bow shock and magnetopause....95

4.6 Displacement amplitude versus frequency and L value for the magnetosheath waveguide eigenmodes....97

4.7 Comparison of magnetosheath eigenmode frequencies and observed FLR frequencies....97

4.8 Variation of magnetosheath eigenmode frequencies as a function of k_y....99

4.9 Variation of magnetosheath eigenmode frequencies as a function of k_z....99

4.10 Variation of magnetosheath eigenmode frequencies as a function of V_A....100

4.11 Variation of magnetosheath eigenmode frequencies as a function of C_s....100

4.12 Variation of magnetosheath eigenmode frequencies as a function of x_{mp}....101

4.13 Variation of magnetosheath eigenmode frequencies as a function of x_{bs}..... 101

4.14 Percentage change in the frequency of the 2nd odd eigenmode as a function of changes in the various plasma parameters.....102

4.15 Equatorial projection of best fitting curves for observed bow shock locations..... 103

4.16 Plots of (a) $|\xi_{yx}|$ and (b) $|E_x|$ as a function of frequency and L value calculated from numerical solutions to the warm MHD equations and matching the magnetosheath eigenmodes at the magnetopause..... 105

List of Symbols and Abbreviations

$\boldsymbol{B}$	magnetic induction vector
β	plasma beta parameter
C_s	speed of sound
$\boldsymbol{D}$	electric displacement vector
$\boldsymbol{E}$	electric field vector
ELF	extremely low frequency
ε_o	dielectric constant in vacuum
FFT	fast Fourier transform
FLR	field line resonance
Φ	magnetic flux
g	plasma parameter
γ	ratio of specific heats
$\boldsymbol{H}$	magnetic field vector
HF	high frequency
IGRF	international geomagnetic reference field
$\boldsymbol{J}$	current density
$\boldsymbol{k}$	wave vector
K_B	Boltzmann constant
Kp	planetary magnetic index of solar wind disturbance
L	length scale or radial distance measured in Earth radii.
λ_D	Debye length
m	mass
m	azimuthal wave number
M_A	Alfvén Mach number
MHD	magnetohydrodynamic
μ_o	magnetic permeability of free space
n	number density
N_D	number of particles in a Debye sphere
$\boldsymbol{P}$	pressure tensor
p	scalar pressure
PACE	polar Anglo-American conjugate experiment
Pc	continuous pulsation
Pi	irregular pulsation
q	charge
$\boldsymbol{r}$	particle displacement vector
R_E	1 Earth radius
RF	radio frequency
R_m	magnetic Reynolds number
ρ	mass density
ρ_c	charge density
$\boldsymbol{S}$	Poynting flux
Σ_P	height integrated Pedersen conductivity
Σ_H	height integrated Hall conductivity

σ	ionospheric conductivity
T	temperature
ULF	ultra low frequency
v	particle velocity
V	center of mass velocity
V_A	Alfvén velocity
v_g	group velocity
v_p	phase velocity
VLF	very low frequency
ω	wave frequency
x_{bs}	bow shock position
x_{mp}	magnetopause position
x_{pp}	plasmapause position
x_r	resonance position
ξ_x	radial displacement

1

Introduction

1.1 Preliminary Remarks

In general, the field of solar-terrestrial physics is concerned, as the name suggests, with the effects of the Sun upon our terrestrial environment. To the lay person the Sun's effects upon the Earth are manifested primarily in the weather patterns which affect our daily lives. However, the outflow of ionized and magnetized gas from the Sun called the solar wind also has a dramatic effect upon the Earth's magnetic environment, the magnetosphere. The most well known effect of this interaction between the solar wind and the magnetosphere is the colorful emission of light near the north and south poles called the aurora. There are three fundamental mechanisms by which the solar wind energy is transported into the magnetosphere. The first mechanism involves the dayside merging of the Earth's magnetic field with the solar wind's interplanetary magnetic field and the resulting reconnection of fields in the nightside tail of the magnetosphere. The energy transferred during dayside merging is stored in the tail of the magnetosphere. Eventually that energy is released and dissipated into the ionosphere during events known as substorms which are characterized by intense auroral activity. The second mechanism of energy transport is via a viscous interaction at the magnetopause boundary which results in a mixing of solar wind and magnetospheric plasmas. The third mechanism of energy transport involves the propagation of fast compressional magnetohydrodynamic (MHD) waves and their coupling to resonant shear Alfvén waves. This mechanism channels the wave energy into very localized, and thin, regions within the magnetosphere. Field lines resonances (FLRs) are the result and are the topic of this thesis.

FLRs are standing shear Alfvén wave oscillations of the Earth's magnetic field lines which are coupled to fast compressional MHD waves in the outer magnetosphere. The FLRs which are of interest in this work are those ultra low frequency (ULF) pulsations in the 0.5-5 mHz range which occur at discrete, stable and reproducible frequencies and which are localized in latitude as well as being extended azimuthally along a latitudinal contour. The body of observational evidence supporting the existence of the discrete, reproducible FLRs is growing steadily [*Ruohoniemi et al.*, 1991; *Samson et al.*, 1991;*Walker et al.*, 1992; *Ziesolleck and McDiarmid*, 1994]. Recent studies [*Samson et al.* 1992a, *Samson et al.*, 1996] have shown a possible

association between FLRs, auroral arcs, and substorm dynamics. If FLRs are involved in the generation of auroral arcs and the triggering of substorms then they are definitely a key player in the transport of energy from the solar wind to the ionosphere. Currently, there are many unknown aspects about the discrete FLR, including the fact that the driving mechanism responsible for them is not known. Thus the primary goals of this thesis are 1) to make experimental observations of FLRs in order to define their characteristics and 2) to develop a model of the FLR generation mechanism consistent with the experimental observations. Achieving these goals will bring us one step closer to a complete understanding of energy transport in the magnetosphere.

A detailed introduction to space physics can be found in a number of introductory text books, for example *Parks* [1991] and *Kivelson and Russell* [1995]. In the remaining sections of this chapter, the necessary background and theory concerning the FLR is presented. Here, basic concepts of space physics, space plasmas, magnetohydrodynamic (MHD) waves, and mode coupling are introduced. The equations governing the coupling of MHD compressional and shear Alfvén waves are derived and the characteristics of the FLR outlined. The chapter ends with a review of previous experimental observations and a discussion of the most commonly accepted theory concerning the source of the FLRs.

Before any conclusions about the source of the FLRs can be made it is essential to have a good basis of experimental observations from which a consistent set of FLR characteristics can be derived. Thus numerous FLR events have been identified with the Super Dual Auroral Radar Network (SuperDARN) and have been analyzed. Some new and exciting results, such as the observation of discrete FLRs with both large and small azimuthal wave number, have been found which are very important parameters in the identification of the FLR source. These results as well as a description of the observational methods are the topics of Chapter 2. In Chapter 3 the results and implications of a study on the growth and decay of the FLRs are presented. Given the new set of FLR characteristics arising from the observational study it has become apparent that the most commonly accepted theory, the waveguide/cavity mode model, falls far short of providing a model consistent with all observations. In Chapter 4 the limitations of the waveguide/cavity mode model are discussed and alternate theoretical models are considered. Finally, the conclusions of the thesis are reemphasized and some future directions discussed in Chapter 5.

1.2 Background and Theory

1.2.1 Basic Definitions and Concepts

The field line resonance phenomenon is a result of a multistep interaction between the solar wind, magnetosphere, and ionosphere. Therefore, I will begin with some basic definitions and concepts concerning these three regions of space. For a visual reference, Figure 1.1 is a simple schematic of the Earth's magnetosphere.

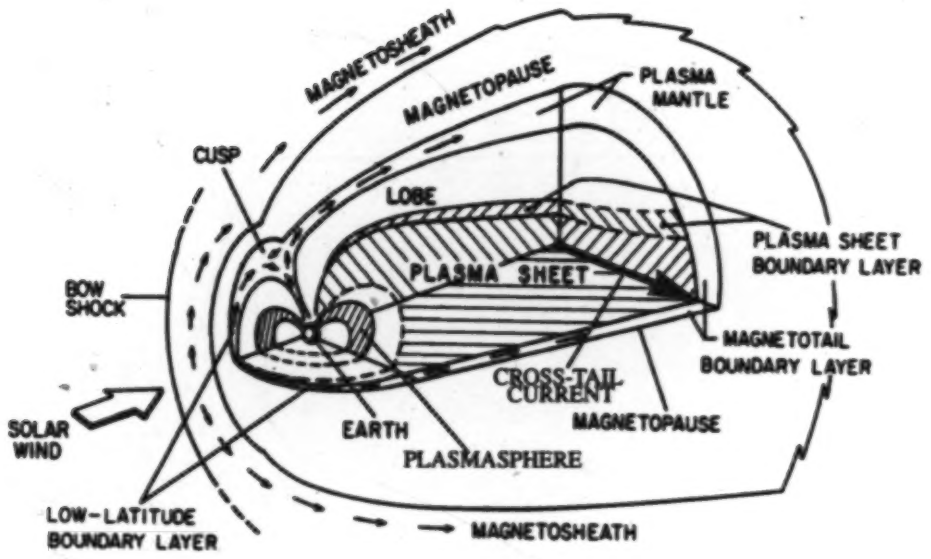

Figure 1.1. Three dimensional cutaway view of the Earth's magnetosphere [from *Eastman et al.*, 1985].

1.2.1.1 The Solar Wind

The solar wind is an extension of the Sun's outer atmosphere, the corona, which extends throughout the entire solar system. The existence of a dynamic coronal outflow was first predicted by *Parker* [1958] and later verified when the first space-borne instruments began to make measurements in the solar wind. It was discovered that the solar wind is a neutral plasma whose ion component is comprised mainly of protons, H^+, with densities on the order of 10 cm^{-3} at the Earth. Because of the frozen-in-field condition, to be discussed in a later section, the solar wind plasma carries the Sun's magnetic field with it which results in an interplanetary magnetic field strength of approximately 10 nT at the Earth. Solar wind speeds increase with increasing distance from the Sun and are typically 400 km/s at the Earth. This value can vary by 100s of km/s due to variations in solar activity. Since the solar wind speed exceeds both the speed of sound (~50km/s) and the Alfvén speed (~40km/s), the Earth's motion is supersonic and super Alfvénic in the rest frame of the solar wind. Thus a shock wave, called the bow shock, is formed in front of the Earth. The bow shock acts to slow and heat solar wind particles as they approach the Earth. Behind the bow shock is the region of shocked solar wind known as the magnetosheath.

1.2.1.2 The Magnetosphere

The region of space encompassing the Earth's magnetic field is the magnetosphere and it is bounded by the magnetopause. Although the Earth's magnetic field is dipolar, its interaction with the dynamic solar wind compresses it on the dayside while stretching it into a long tail on the nightside. Associated with the deformation of the Earth's magnetic field is a set of four current systems: the magnetopause current, the ring current, cross-tail current, and field-aligned current. The magnetopause current, as the name suggests, flows along the magnetopause and is due to the discontinuity in the magnetic field and plasma pressure across the magnetopause. The ring current is a clockwise current around the Earth which arises from the differential gradient-curvature drifts of ions and electrons within the dipole-like field region. In the magnetotail, the direction of the magnetic field reverses across the equatorial plane in association with a layer of current flowing from dawn to dusk called the cross-tail current. This current divides at the flanks and closes around the magnetopause. Field aligned currents are any currents which flow along the Earth's magnetic field lines. There are different types of field aligned current systems depending upon their location, and generation mechanism. Field aligned currents couple the magnetosphere to the ionosphere and can couple the

ionosphere directly to the solar wind in the polar region.

The magnetosphere is separated into various regions depending upon plasma and magnetic field characteristics. The plasma sheet is the region of the magnetosphere which is populated by particles of ionospheric or solar wind origin. These particles, if energetic enough, precipitate into the high-latitude ionosphere creating luminous auroral displays. The plasma sheet contains the cross-tail current region which is a region containing hot plasma and a weak B field. The magnetic tail lobe is the region adjacent to the plasma sheet where the plasma density is very much reduced. The plasmasphere corotates with the Earth and extends to the plasmapause at approximately 5 R_E.

The direction of the interplanetary magnetic field relative to the Earth's field has a dramatic effect upon the morphology of the magnetosphere. An interplanetary field with a negative B_z component produces an open magnetosphere with magnetic merging on the dayside and reconnection on the night side. The result is field lines with one foot on the sun and the other on the Earth. When the interplanetary field has a positive B_z component, the configuration is that of a closed magnetosphere. The processes of mass, momentum and energy transport from solar wind to magnetosphere for these two configurations differ greatly. It is during open magnetospheric configurations that the magnetosphere becomes most energized since the solar wind mass, momentum and energy can directly enter the magnetosphere and be stored in part in the magnetotail. Transitions of the magnetosphere from a highly energized state to a more relaxed state requires a release of energy. This release of energy is brought about through dipolarization of the magnetotail and the generation of large scale currents, in particular, field aligned currents which can generate brilliant auroral displays. Such intense dynamic transitions of the magnetosphere are referred to as substorms. Substorms can have many levels of intensity depending upon the initial and final energy states of the magnetosphere. Generally, substorms are a result of the transition from an open to a more closed magnetospheric configuration. The substorm and its triggering mechanisms are currently a topic of great debate in the space science community. A summary of the many substorm models is given by McPherron [1995]. The observations of FLRs in this work were almost all during periods of quiet magnetospheric conditions with no association with substorms. This does not imply that FLRs are not associated with substorms but only that FLRs are best observed and studied during periods of quiet conditions.

1.2.1.3 The Ionosphere

The ionosphere is the ionized portion of the Earth's atmosphere extending from ~60 km and upwards into the magnetosphere. The ionization is caused by incident solar radiation and is maintained because of the slow recombination rate. Some ionization is also due to energetic particle precipitation.

The ionosphere is classified into three regions according to height. At the lower edge, below ~90 km, is the D region. This region is ionized by only the most energetic ionization sources such as solar X-rays and cosmic ray particles. Because of higher collision frequencies and limited ionizing radiation, the electron densities in this part of the ionosphere are low at ~500 cm^{-3}. Between 90 and 130 km is the E region which is characterized by a sharp increase in electron density to ~10^5 cm^{-3}. Above 130 km is the F region which exhibits the maximum ionospheric electron density of ~10^6 cm^{-3} at ~300 km altitude. The above density values are taken from Kivelson and Russell [1995]. Because of its electron density profile, the ionosphere is very important for radio-wave communication and is also subject to intense study by means of radio frequency (RF) experiments. In particular, the experimental data presented in this thesis are that of high frequency (HF) radars which are designed to utilize the refraction and reflection properties of high frequency RF in the ionosphere to measure bulk plasma flows in the F region. The details of this radar technique are described in more detail in Chapter 2.

In the collisional ionosphere there are two types of current which flow perpendicular to the ambient magnetic field: the Pedersen current and the Hall current. The Pedersen current flows in the direction of the perpendicular electric field $\mathbf{E}_\perp$ and results from the acceleration of the ions and electrons under the influence of $\mathbf{E}_\perp$ between collisions. The Hall current flows perpendicular to both $\mathbf{E}_\perp$ and **B** in the direction of -**ExB**. It is due to the fact that although both ions and electrons are **ExB** drifting, the ions are slowed down much more than the electrons in their attempt to drift because of collisions with neutrals and other ions. The size of the height integrated perpendicular current depends upon the Hall and Pedersen conductivities, defined by Σ_P and Σ_H respectively, as well as $\mathbf{E}_\perp$.

The ionosphere also provides a major energy sink for any energy entering the magnetosphere from the solar wind. This energy is deposited into the ionosphere by the field aligned current systems. The field aligned current systems close through the perpendicular currents in the ionosphere and dissipate some of the energy in the form of Joule heating. The field aligned current is carried primarily by electrons. The most

energetic electrons can excite the ions and neutrals to various energized states. As the excited atmospheric constituents decay to lower energy states they emit electromagnetic radiation which constitutes, in part, the auroral emissions of light known as the aurora borealis or northern lights in the northern hemisphere and the aurora australis or southern lights in the southern hemisphere. The ionospheric emissions are generally localized to a band of latitudes approximately 5° wide at 20-25° from the poles known as the auroral zone. In open magnetospheric conditions, field aligned currents can flow along field lines which are directly linked to the solar wind. These field aligned currents can result in cusp and polar auroras. The visual colors which characterize the auroras are determined by the emission characteristics of the excited atmospheric constituents as well as the energies of the precipitating particles. In addition, the precipitated energy can be converted to bremsstrahlung X-ray radiation which make the auroras an X-ray source as well. The energy dissipated in a typical auroral event is on the order of 10^{14} Joules.

1.2.1.4 Space Plasmas

In order for the ionized gases which permeate the solar wind, magnetosphere and ionosphere to be classified as plasmas they must satisfy certain conditions. The density of particles in a plasma must be sufficiently low so that short range collisions are negligible while at the same time the total number of particles must be large enough for the system to act collectively. The collective nature of a plasma arises from the long-range electromagnetic forces present between the charged particles. A positively charged ion will attract electrons while repelling other positive ions which causes its electrostatic field to become shielded from the bulk of the plasma. Because of this collective interaction the force range of a charged particle has a characteristic length defined by the Debye length

$$\lambda_D = \sqrt{\frac{K_B T \varepsilon_o}{nq^2}} \tag{1.1}$$

where K_B is the Boltzmann constant, ε_o is the dielectric constant of free space and T, n, and q are the temperature, density, and charge, respectively, of the charged particle species generally taken to be the electron. A system of charged particles is correctly

characterized as a plasma only if a value known as the plasma parameter is much less than one. The plasma parameter is defined by

$$g = \frac{1}{N_D} \tag{1.2}$$

where N_D is the number of particles in a Debye sphere, i.e.

$$N_D = \frac{4\pi n \lambda_D^3}{3} \ . \tag{1.3}$$

Order of magnitude estimates for n, T, λ_D and g in the solar wind, magnetosphere and ionosphere are presented in Table 1.1. Since $g<<1$ for each of these regions they are correctly classified as space plasmas. The number of particles present in each of these systems is large enough to make Debye shielding effective, and since $\lambda_D<<L$ for each of the three regions, where L represents a characteristic length, the plasmas are essentially free of any significant electrostatic potentials and therefore are considered neutral.

Table 1.1: Some Typical Space Plasma Parameters*

	n (m^{-3})	T (^oK)	λ_D (m)	g
Solar Wind (near Earth)	10^7	10^5	10	10^{-11}
Magnetosphere	10^5-10^7	10^5-10^9	10^2-10^3	10^{-15}
Ionosphere	10^9-10^{12}	10^3-10^4	10^{-3}-$3x10^{-2}$	10^{-5}

*n and T values taken from *Parks* [1991].

Since the collision frequency decreases with decreasing density and with increasing temperature, those regions of space with low plasma density and high temperature such as the solar wind and magnetosphere are essentially collisionless. The

ionosphere, on the other hand, has significantly larger densities and lower temperatures, relative to the solar wind and magnetosphere, and cannot be considered collisionless. The ionosphere is a much more complicated plasma because it contains ion populations such as N_2^+, O^+, NO^+ as well as neutral molecules. The solar wind and magnetosphere are primarily electron-proton plasmas with H^+ being the dominant ion. However, the solar wind and magnetosphere contain some other ions such as He^{++}. Also, some of the ionospheric ions such as O^+ find their way into the magnetosphere.

1.2.2. MHD Theory

As discussed above space plasmas have fluid properties due to the fact that they behave as a non-interacting, neutral, collective system. However, because they consist of charged particles in motion through a background magnetic field, electromagnetic fields are also an integral part of the space plasma system. The combination of electromagnetic and fluid properties results in a class of waves known as magnetohydrodynamic or MHD waves. These waves are low frequency, i.e. their frequencies are much lower than any of the natural plasma frequencies, and can have both transverse and longitudinal modes. The FLRs studied in this thesis are a result of the coupling between longitudinal and transverse MHD wave modes. Thus a detailed discussion of the MHD wave description is the topic of this section.

Before introducing the details of the MHD theory some mention should be made of other ways of dealing with magnetized plasmas. The most general approach to the problem is to use a kinetic theory based upon the Boltzmann-Vlasov equations, which take into account the dynamics of the individual particles rather than the plasma fluid as a whole. The Boltzmann-Vlasov equation is given by

$$\frac{\partial f}{\partial t} + \boldsymbol{v} \cdot \frac{\partial f}{\partial \boldsymbol{r}} + \frac{q}{m} (\boldsymbol{E} + \boldsymbol{v} \times \boldsymbol{B}) \cdot \frac{\partial f}{\partial \boldsymbol{v}} = 0 \qquad (1.4)$$

where $f=f(\boldsymbol{r},\boldsymbol{v},t)$ represents the distribution function of particles in $(\boldsymbol{r},\boldsymbol{v})$ space with $\boldsymbol{r}$ the particle position and $\boldsymbol{v}$ its velocity. This equation defines the total time derivative of $f(\boldsymbol{r},\boldsymbol{v},t)$ for a system of collisionless particles subject only to electromagnetic forces. Equation (1.4) and Maxwell's equations are solved self-consistently in the kinetic approach.

The fluid treatment which follows is a simplification of the full kinetic treatment. In a fluid, macroscopic parameters are used to define the system. These macroscopic

parameters are obtained by averaging over all particles in velocity space. The fluid equations governing the macroscopic parameters such as the continuity of mass and momentum equations are then obtained by taking various moments of the Boltzmann-Vlasov equation. To arrive at the MHD fluid equations the distribution function used in taking the averages and moments is a Maxwellian,

$$f(r,v) = n\left(\frac{m}{2\pi KT}\right)^{3/2} exp\left[\frac{-m\,(v-\langle v\rangle)^2}{2KT}\right] \tag{1.5}$$

where <v> corresponds to the average particle velocity. This equation corresponds to a plasma in thermal equilibrium. In non-equilibrium situations where plasma instabilities can be driven by velocity-space anisotropies, an appropriate distribution function and a full kinetic formulation must be used.

In practice, the use of MHD generally requires certain assumptions to be made about the nature of the plasma. In deriving the MHD equations these assumptions will be pointed out and justification for their validity made. However, it should be emphasized that in instances where these assumptions do not hold, the associated MHD equations fail to provide the proper description for the plasma.

In the theory of the FLR the general approach is that of one-fluid MHD. This approach assumes that the plasma system contains only electrons and one species of ion with the conditions that $n_i=n_e=n$ and $q_i=-q_e=q$, where n represents number density and q the electrostatic charge. In the magnetosphere and the solar wind this assumption is quite valid as these regions are dominated by protons, with equal numbers of electrons.

In general when describing a plasma system, a fluid equation is required for each particle species in the system. For a plasma composed of electrons and one ion species, the system dynamics are described by the "two-fluid" equations. Since the ion and electron motions are coupled, the solutions to the two-fluid equations are not easily obtained. However, the two-fluid equations can be simplified to a set of one-fluid equations as will be shown in the following section. The one-fluid equations, though not as complete as the two-fluid equations, are quite successful in their description of the basic behavior of MHD plasma and they have the distinct advantage of being more easily solved.

1.2.2.1 One-Fluid Equations

Based on the conservation of mass, both the electron and ion species in a two-component plasma must satisfy the continuity equation as follows:

$$\frac{\partial \rho_i}{\partial t} + \nabla \bullet \rho_i v_i = 0$$
$$\frac{\partial \rho_e}{\partial t} + \nabla \bullet \rho_e v_e = 0 \qquad (1.6)$$

where ρ and v represent the mass density and the average fluid velocity, respectively, for the ions, i, and the electrons, e. One first defines the total mass density of the fluid as

$$\rho = n_i m_i + n_e m_e \qquad (1.7)$$

and the total fluid velocity as an effective center of mass velocity

$$V = \frac{n_i m_i v_i + n_e m_e v_e}{n_i m_i + n_e m_e} . \qquad (1.8)$$

Then adding together the ion and electron continuity equations in (1.6) and substituting (1.7) and (1.8) yields the one-fluid continuity equation:

$$\frac{\partial \rho}{\partial t} + \nabla \bullet \rho V = 0 . \qquad (1.9)$$

The fluid equation of motion for a given fluid species is given by

$$mn\frac{dv}{dt} = qn(E + v \times B) - \nabla \bullet P , \qquad (1.10)$$

where P represents a pressure tensor which in most general terms is anisotropic. This equation is just Newton's second law of motion, $F=ma$, where the forces are the Lorentz force, $q(E+v\times B)$ and the pressure gradient force, $-\nabla \bullet P$. Collisional and gravitational effects have been neglected. If the pressure is isotropic, $\nabla \bullet P$ becomes ∇p where p is the scalar pressure. Once again, for a plasma of electrons and one ion species, two equations of motion are required:

$$m_i n_i \frac{dv_i}{dt} = q_i n_i (E + v_i \times B) - \nabla \bullet P_i$$
$$m_e n_e \frac{dv_e}{dt} = q_e n_e (E + v_e \times B) - \nabla \bullet P_e . \qquad (1.11)$$

Making the aforementioned assumptions $n_i=n_e=n$ and $q_i=-q_e=q$, the above two equations can be added to give

$$\rho\frac{dV}{dt} = qn(v_i - v_e)\times B - \nabla\bullet(P_i + P_e) \ . \tag{1.12}$$

Defining the total pressure tensor as

$$P = P_i + P_e \tag{1.13}$$

and the current density as

$$J = n_i q_i v_i + n_e q_e v_e \tag{1.14}$$

and substituting into (1.12) yields the one-fluid momentum equation

$$\rho\frac{dV}{dt} = J\times B - \nabla\bullet P \ . \tag{1.15}$$

1.2.2.2 Maxwell's Equations

The electromagnetic fields in a plasma are governed by Maxwell's equations. In differential form these are:

Faraday's law:

$$\nabla\times E = \frac{\partial B}{\partial t} \tag{1.16}$$

Absence of magnetic monopoles:

$$\nabla\bullet B = 0 \tag{1.17}$$

Ampere's law:

$$\nabla\times H = J + \frac{\partial D}{\partial t} \tag{1.18}$$

Coulomb's law:

$$\nabla \bullet \boldsymbol{D} = \rho_c \tag{1.19}$$

Constitutive relations:

$$\boldsymbol{B} = \mu_o \boldsymbol{H} \qquad \boldsymbol{D} = \varepsilon_o \boldsymbol{E} \tag{1.20}$$

Since space plasmas are good electrical conductors, free charges generally do not accumulate. Therefore, the background charge density, ρ_c, in Coulomb's law is sometimes taken to be zero. However, if there is finite vorticity, ρ_c will not be zero. In addition, MHD is a low-frequency approximation where the displacement current, $\partial \boldsymbol{D}/\partial t$, is considered negligible compared to the conduction current, $\boldsymbol{J}$. This results in a modified Ampere's law

$$\nabla \times \boldsymbol{H} = \boldsymbol{J} \, . \tag{1.21}$$

1.2.2.3 Ohm's Law

In addition to the fluid and Maxwell's equations, further equations are required to solve the MHD equations. Since, an MHD fluid behaves as an electrical conductor, Ohm's law provides some of those equations. Ohm's law is an empirical law relating the current density, $\boldsymbol{J}$, to the total electric field, $\boldsymbol{E}$. Since the total electric field includes fields induced by the motion of the plasma across magnetic fields, Ohm's law is represented by

$$\boldsymbol{J} = \sigma(\boldsymbol{E} + \boldsymbol{V} \times \boldsymbol{B}) \tag{1.22}$$

where σ is the conductivity. It should be stressed that Ohm's law should only be used in regions where a conductivity can be defined such as in the ionosphere where collisions are frequent enough to actually calculate values for the conductivity. However, in regions such as the solar wind and magnetosphere where the plasma is essentially collisionless, the conductivity is assumed to be infinite and the ideal MHD

approximation is applied.

1.2.2.4 Ideal MHD

Ideal MHD fluids are those fluids which have infinite conductivity. Although an infinite conductivity can never exist in reality, some MHD fluids have such large conductivities that the ideal condition of $\sigma \to \infty$ describes the plasma behavior very well. In this limit Ohm's law becomes

$$E = -V \times B \ . \tag{1.23}$$

The ideal MHD approximation is also synonymous with the frozen-in-field concept where the magnetic flux through any closed loop moving with the plasma remains constant. In ideal MHD no induced electric fields can exist in the rest frame of the plasma. Then, according to the form of Faraday's law given by

$$\oint E \bullet dl = -\frac{d\Phi}{dt} \tag{1.24}$$

where Φ is the magnetic flux through the closed loop, there can also be no change in the magnetic flux.

Another way to look at the frozen-in-field condition is by considering the rate at which the magnetic field will diffuse through the plasma. A frozen-in-field corresponds to little or no diffusion of the magnetic field. A measure of magnetic field diffusion is given by the magnetic Reynolds number

$$R_m = \mu_o \sigma L V \tag{1.25}$$

where μ_o is the magnetic permeability of free space, and L is a characteristic length. In the case of ideal MHD $\sigma \to \infty$ and therefore $R_m \to \infty$ and magnetic field diffusion can be ignored.

1.2.2.5 Equation of State

In any fluid, including MHD fluids, the equation of state relates the fluid mass

density, ρ_m, pressure, p, and temperature, T. For an MHD plasma having an isotropic Maxwellian distribution, the equation of state is given by

$$\frac{d}{dt}(p\rho_m^{-\gamma}) = 0 \tag{1.26}$$

where γ=5/3 is the ratio of specific heats. Such a plasma behaves as an ideal adiabatic gas. An equation of state is necessary to close any system of fluid equations, which are coupled moments of the Boltzmann-Vlasov equation.

1.2.2.6 Cold Plasma Approximation

In the cold plasma approximation $T \to 0$ and any thermal effects are ignored. Therefore, in the equation of motion the ∇p term is negligible when compared to the $\boldsymbol{J}\times\boldsymbol{B}$ term. To compare these two terms rewrite $\boldsymbol{J}\times\boldsymbol{B}$ as

$$\boldsymbol{J}\times\boldsymbol{B} = \frac{(\nabla\times\boldsymbol{B})\times\boldsymbol{B}}{\mu_o} = \frac{\boldsymbol{B}\bullet\nabla\boldsymbol{B}}{\mu_o} - \frac{\nabla B^2}{2\mu_o} . \tag{1.27}$$

The first term on the right arises from magnetic field curvature while the second term is due to magnetic field pressure. Now, the beta of a plasma, β, is defined as the ratio of particle pressure to magnetic field pressure

$$\beta = \frac{p}{B^2/(2\mu_o)} . \tag{1.28}$$

In the cold plasma approximation $\beta \to 0$ and the plasma is dominated by the magnetic field pressure rather than the plasma particle pressure. Thus ∇p is negligible when compared to $\nabla(B^2/2\mu_o)$ and can be ignored in the equation of motion. The equation of state also becomes irrelevant.

1.2.2.7 Summary of One-Fluid MHD

The set of equations governing one-fluid MHD plasma under the ideal and cold plasma approximation are as follows:

Continuity equation:

$$\frac{\partial\rho}{\partial t} + \nabla\bullet\rho\boldsymbol{V} = 0 \tag{1.29}$$

Equation of motion:

$$\rho\frac{dV}{dt} = J \times B \tag{1.30}$$

Ohm's law:

$$E = -V \times B \tag{1.31}$$

Maxwell's equations:

$$\nabla \times E = -\frac{\partial B}{\partial t} \tag{1.32}$$

$$\nabla \times B = \mu_o J \tag{1.33}$$

These are the equations used to derive the coupling process between the shear Alfvén and compressional MHD wave modes in the magnetosphere which is responsible for the field line resonance phenomenon. Based upon the observations of FLRs discussed in this thesis, the region of the magnetosphere where the coupling process occurs is between approximately 8-12 Re in the equatorial plane. Thus it is assumed that all of the approximations that have gone into the derivation of the above equations are valid in this region of the magnetosphere. The validity of many of these approximations have already been previously discussed. However, a few comments should be made with respect to the cold plasma approximation and the neglect of particle pressure. Along the flanks of the magnetosphere, in the region between the plasmapause at ~5 Re and the magnetopause at ~14-15 Re, the plasma Beta parameter ranges from ~0.01 at the plasmapause to ~0.1 at the magnetopause. Thus in the region where the FLR coupling process occurs, the plasma can be considered a low-β plasma and the neglect of particle pressure is a reasonable approximation. In a later chapter, when the magnetosheath region is developed as a source of monochromatic compressional modes, the particle pressure is maintained since the plasma in this region is a "warm" plasma, i.e. it no longer satisfies the cold plasma approximation.

1.2.2.8 MHD Plasma Waves

There are three wave modes which can propagate in a warm MHD plasma. These are the shear Alfvén wave, the fast magnetoacoustic wave, and the slow

magnetoacoustic wave. Each of these wave modes is defined by a dispersion relation which relates the wave frequency, ω, to the wave vector, $\boldsymbol{k}$. The general dispersion relations for the MHD waves can be derived from the MHD equations defined in the previous section. For an example of the derivation see *Parks* [1991] or *Kivelson and Russell* [1995].

The shear Alfvén wave is a purely transverse wave with flow perturbations perpendicular to both the wave vector and the background magnetic field, $\boldsymbol{B}_o$. Its dispersion relation is given by

$$\frac{\omega^2}{k^2} = V_A^2 \cos^2\theta \tag{1.34}$$

where V_A is the Alfvén velocity defined by

$$V_A^2 = \frac{B_o^2}{\mu_o \rho} \tag{1.35}$$

and θ is the angle between $\boldsymbol{B}_o$ and the wave vector $\boldsymbol{k}$. A schematic of the electric field, magnetic field, flow and current polarizations for the shear Alfvén wave are shown in Figure 1.2. Because the flow perturbations are perpendicular to the propagation direction there are no plasma density perturbations associated with the wave. The magnitude of the magnetic field also remains constant because the field perturbations, $\boldsymbol{B}$, are normal to $\boldsymbol{B}_o$. Thus the shear Alfvén wave is non-compressional

The phase velocity of a wave is

$$\boldsymbol{v}_p = \frac{\omega}{k}\hat{\boldsymbol{k}} \tag{1.36}$$

and therefore according to equation (1.34) the shear Alfvén wave phase velocity is $V_A cos\theta$. The group velocity defined by

$$\boldsymbol{v}_g = \nabla_{\boldsymbol{k}}\omega \tag{1.37}$$

determines the direction of energy flow of the wave. This direction is coincident with the direction of the Poynting vector

$$\boldsymbol{S} = \frac{1}{\mu_o}\boldsymbol{E} \times \boldsymbol{B} \tag{1.38}$$

which for the shear Alfvén wave is along B_o. The magnitude of the group velocity for the shear Alfvén wave is $v_g=V_A$..

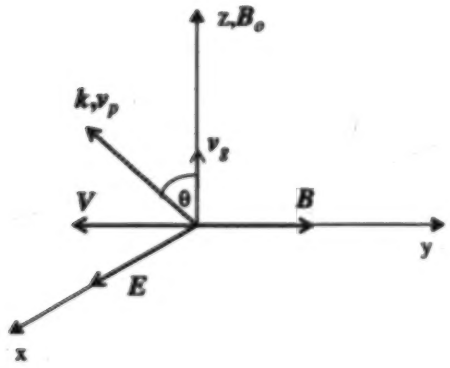

Figure 1.2 Schematic of shear Alfvén wave.

The dispersion equation defining the magnetoacoustic wave modes is

$$\frac{\omega^2}{k^2} = \frac{1}{2}\{V_A^2 + C_s^2 \pm \left[(V_A^2 + C_s^2)^2 - 4C_s^2 V_A^2 \cos^2\theta\right]^{1/2}\} \qquad (1.39)$$

where C_s is the speed of sound in the plasma. The positive sign corresponds to the fast wave mode and the negative sign to the slow wave mode. Both of these wave modes are compressional waves with perturbations in both plasma density and magnetic field magnitude. They are a result of the coupling of electromagnetic wave modes to acoustic wave modes in the plasma. Differences between the fast and slow modes include their phase and group velocities. As the names suggest, the fast mode propagates much faster than the slow mode. Group propagation for the fast mode is along the wave vector k, while group propagation for the slow mode remains predominantly aligned along B_o. Another distinguishing feature is found in their pressure perturbations. Pressure and magnetic perturbations are in phase for the fast wave, but out of phase for the slow wave.

In a cold plasma, where p=0, the acoustic contributions to the magnetoacoustic modes disappear as the C_s becomes zero. The dispersion equation describing the compressional modes reduces to

$$\frac{\omega^2}{k^2} = V_A^2 \tag{1.40}$$

for the fast mode, and

$$\frac{\omega^2}{k^2} = 0 \tag{1.41}$$

for the slow mode, i.e. the slow mode does not propagate in a cold plasma.

Figure 1.3 is a schematic of the wave perturbations associated with the fast compressional mode in a cold plasma. Both the phase and energy of the fast compressional wave propagate along the wave vector k with speed V_A.

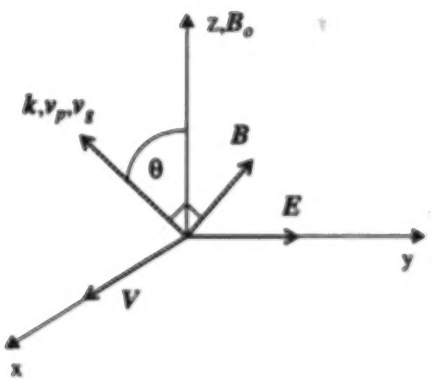

Figure 1.3. Schematic of fast compressional Alfvén wave.

1.2.3 Field Line Resonance Coupling

The coupling between the fast compressional and shear Alfvén waves in the magnetosphere has been developed by various authors [*Tamao*, 1966; *Southwood*, 1974;and *Chen and Hasegawa*, 1974]. In this section the cold, ideal MHD plasma equations discussed in the previous section will be used to derive the FLR coupling equations. A simple box model of the magnetosphere can provide the basic features of the coupling mechanism. A schematic of this box model is shown in Figure 1.4. The z-direction is aligned along *Bo*, the x-direction radially outward, and the y-direction is azimuthal to complete the right-handed coordinate system. The field line lengths are taken to be constant and are bounded by the ionospheres. The zeroth order mass density, ρ_o, is taken to vary radially such that the resulting Alfvén velocity decreases with x. The plasma perturbations of the system are assumed to be small with variations in time and the y and z directions given by

$$e^{i(\omega t - k_y y - k_z z)} \tag{1.42}$$

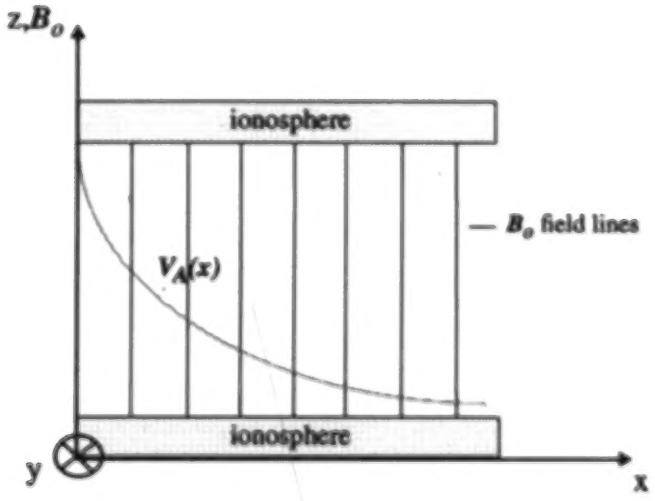

Figure 1.4. Box model of magnetosphere.

Note that k_z, the field-aligned wave vector, is taken to be inversely proportional to the field line length in order to correspond to a standing wave along the field line. Derivatives with respect to y, z and t can be expressed as follows.

$$\begin{aligned} \frac{\partial}{\partial t} &\rightarrow i\omega \\ \frac{\partial}{\partial y} &\rightarrow -ik_y \\ \frac{\partial}{\partial z} &\rightarrow -ik_z \end{aligned} \tag{1.43}$$

In the derivation which follows, the perturbed quantities are represented by the non-scripted variables while the background equilibrium quantities are denoted by the subscript "o". Note that the background flow and electric fields are assumed to be zero, i.e. V_o=E_o=0. In reality this is not necessarily the case, but in an ideal plasma one can always transform to the rest frame of the plasma where V_o and E_o are zero. The equations are linearized by keeping only those terms which are to first order in the perturbed quantities. The resulting linearized cold ideal MHD equations are as follows.

Continuity: $$i\omega\rho + \rho_o \nabla \bullet V = 0 \tag{1.44}$$

Equation of motion: $$i\omega\rho_o V = J \times B_o \tag{1.45}$$

Ohm's law: $$E = -V \times B_o \tag{1.46}$$

Maxwell's equations: $$\nabla \times E = -i\omega B \qquad \nabla \times B = \mu_o J \tag{1.47}$$

From the idealized Ohm's law

$$V_y = -\frac{E_x}{B_o} \qquad V_x = \frac{E_y}{B_o} \tag{1.48}$$

From the second equation in (1.47) J is of the form

$$J = \frac{1}{\mu_o}\left[\hat{x}\,(-ik_y B_z + ik_z B_y) - \hat{y}\,(\frac{\partial B_z}{\partial x} + ik_z B_x) + \hat{z}\,(\frac{\partial B_y}{\partial x} + ik_y B_x)\right] \tag{1.49}$$

Using equation (1.49) $\boldsymbol{J}\times\boldsymbol{B}$ can be evaluated as

$$\boldsymbol{J}\times\boldsymbol{B}_o = \frac{1}{\mu_o}\left[\hat{x}\left(-B_o\frac{\partial B_z}{\partial x} - iB_o k_z B_x\right) + \hat{y}\left(iB_o k_y B_z - iB_o k_z B_y\right)\right] \tag{1.50}$$

where only first order terms have been kept. Substituting (1.50) and (1.48) into the equation of motion (1.45) yields

$$i\omega\rho_o\frac{E_y}{B_o} = \frac{1}{\mu_o}\left(-B_o\frac{\partial B_z}{\partial x} - iB_o k_z B_x\right) \tag{1.51a}$$

$$-i\omega\rho_o\frac{E_x}{B_o} = \frac{1}{\mu_o}\left(iB_o k_y B_z - iB_o k_z B_y\right) . \tag{1.51b}$$

The first of Maxwell's equations in (1.47) provides the equations relating the components of $\boldsymbol{E}$ and $\boldsymbol{B}$:

$$B_x = -\frac{k_z}{\omega}E_y \tag{1.52a}$$

$$B_y = \frac{k_z}{\omega}E_x \tag{1.52b}$$

$$B_z = \frac{i}{\omega}\left[\frac{\partial E_y}{\partial x} + ik_y E_x\right] . \tag{1.52c}$$

Substituting (1.52) into (1.51) gives

$$\left[\frac{\mu_o\rho_o}{B_o^2}\omega^2 - k_z^2\right]E_y = -\frac{\partial}{\partial x}\left[\frac{\partial E_y}{\partial x} + ik_y E_x\right] \tag{1.53a}$$

$$\left[\frac{\mu_o\rho_o}{B_o^2}\omega^2 - k_z^2\right]E_x = -ik_y\left[\frac{\partial E_y}{\partial x} + ik_y E_x\right] . \tag{1.53b}$$

It is apparent in the above two equations that the shear and compressional wave components are coupled. The azimuthal component of the electric field, E_y, corresponds to the compressional or poloidal component while the radial electric field, E_x, corresponds to the shear or toroidal component of the coupled system. Rewriting equation (1.53b) as

$$E_x = \frac{-ik_y\left(\partial E_y/\partial x\right)}{\left[\dfrac{\omega^2}{V_A^2} - k_z^2 - k_y^2\right]} \tag{1.54}$$

and substituting into (1.53a) yields the differential equation governing E_y

$$\frac{\partial^2 E_y}{\partial x^2} - \frac{k_y^2 \frac{\partial}{\partial x}(\omega/V_A)^2}{[(\omega/V_A)^2 - k_z^2]\kappa^2}\left(\frac{\partial E_y}{\partial x}\right) + \kappa^2 E_y = 0 \tag{1.55}$$

$$\kappa^2 = \frac{\omega^2}{V_A^2} - k_z^2 - k_y^2$$

Equation (1.55) has two singular points which have important physical interpretations. The first corresponds to the condition

$$\kappa^2 = 0 \tag{1.56}$$

which is satisfied at the point $x=x_t$ defined as the turning point. It is the point where the solution changes from being purely oscillatory to purely decaying with distance. As shown by *Southwood* [1974], there are two independent solutions to equation (1.55) near the turning point which have the form

$$\begin{aligned} u_1 &= a_o + \sum_{n=1}^{\infty} a_n (x - x_t)^n \\ u_2 &= (x - x_t)^2 \{ b_o + \sum_{n=1}^{\infty} b_n (x - x_t)^{3n} \} \end{aligned} \tag{1.57}$$

and both solutions are finite at $x=x_t$.

The second singular point of equation (1.55) corresponds to the resonance position where

$$G(x) = \frac{\omega^2}{V_A^2} - k_z^2 = 0 \quad . \tag{1.58}$$

Near the resonance position, defined by $x=x_r$, $G(x)$ can be expressed as

$$G(x) \cong (x - x_r)\left.\frac{dG}{dx}\right|_{x=x_r} \quad . \tag{1.59}$$

Substituting this form for G into equation (1.55) gives

$$\frac{\partial^2 E_y}{\partial x^2} + \frac{1}{(x - x_r)} \frac{\partial E_y}{\partial x} - k_y^2 E_y = 0 \quad . \tag{1.60}$$

Equation (1.60) is a modified Bessel equation of order zero, whose solutions are infinite at $x=x_r$. However, the singularity at the resonance position is avoided if there is a small time dependent sink or source of energy in the system. Since the ionosphere does not perfectly reflect shear Alfvén waves, the system's energy is inevitably lost over time. Thus a small time dependent sink at the ionosphere is represented by k_z having a small positive imaginary part, i.e.

$$k_z = k_{z_r} + i k_{z_i} \quad . \tag{1.61}$$

The expansion of G(x) about $x=x_r$ is now given by

$$G(x) = G'(x_r)\,(x - x_r + i\varepsilon) \tag{1.62}$$

where $G'(x_r)$ represents the derivative of $G(x)$ at x_r and

$$\varepsilon \equiv \frac{-2 k_{z_r} k_{z_i}}{G'(x_r)\, V_A^2} \quad . \tag{1.63}$$

Now using equation (1.62), equation (1.55) becomes

$$\frac{\partial^2 E_y}{\partial x^2} + \frac{1}{(x - x_r + i\varepsilon)} \frac{\partial E_y}{\partial x} - k_y^2 E_y = 0 \tag{1.64}$$

which has solutions of the form [*Southwood*, 1974]

$$E_y = C I_o [k_y (x - x_r + i\varepsilon)] + D K_o [k_y (x - x_r + i\varepsilon)] \quad , \tag{1.65}$$

where I_o and K_o are modified Bessel functions of order zero and C and D are determined by boundary conditions.

To see the form of the solution at the resonance take k_y to be small. In the small k_y limit equation (1.65) becomes

$$E_y = -E_o ln [k_y (x - x_r + i\varepsilon)] \tag{1.66}$$

where E_o is now the constant determined by boundary conditions. Note that for small

k_y, the solution at the resonance is dominated by the radial component of the electric field, E_x, and is referred to as a toroidal resonance. Therefore, the form of the solution near $x=x_r$ is best illustrated by E_x, which from combining equations (1.54) and (1.66) is given by

$$E_x = \frac{-iE_o}{k_y(x-x_r+i\varepsilon)} = \frac{-E_o[\varepsilon+i(x-x_r)]}{k_y[(x-x_r)^2+\varepsilon^2]} \quad . \tag{1.67}$$

The general form of E_x at the resonance according to (1.67) is depicted in Figure 1.5.

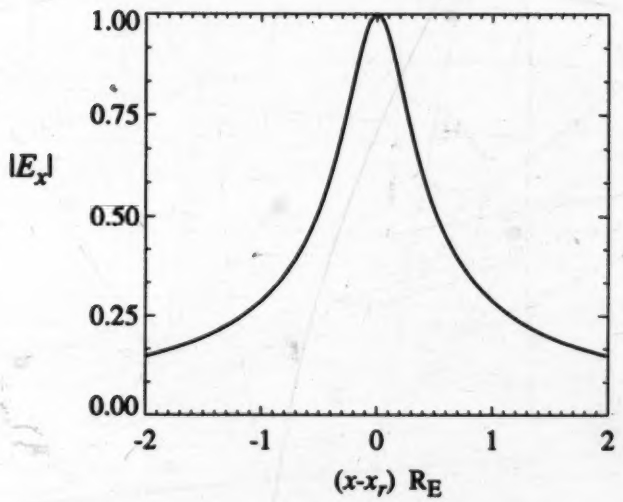

Figure 1.5. Small k_y solution for E_x near resonance. Note that $|E_x|$ has been normalized to 1.

The coupling of compressional and shear Alfvén wave modes in the box model of the magnetosphere resulting in the field line resonance can be summarized as follows. A monochromatic compressional mode propagating through the magnetosphere towards the earth encounters an increasing Alfvén velocity. The wave eventually reaches a turning point where it is partially reflected and partially transmitted. At the turning

point the wave changes from an oscillatory mode to a decaying mode. Thus beyond the turning point the wave is evanescent, i.e. it decays exponentially. At the resonance point the spatial phase and frequency of the fast wave matches that of a standing shear Alfvén wave along the field line. The result is a resonance of the field line whose characteristic shear Alfvén frequency matches the frequency of the fast compressional wave. A schematic of this scenario is shown in Figure 1.6.

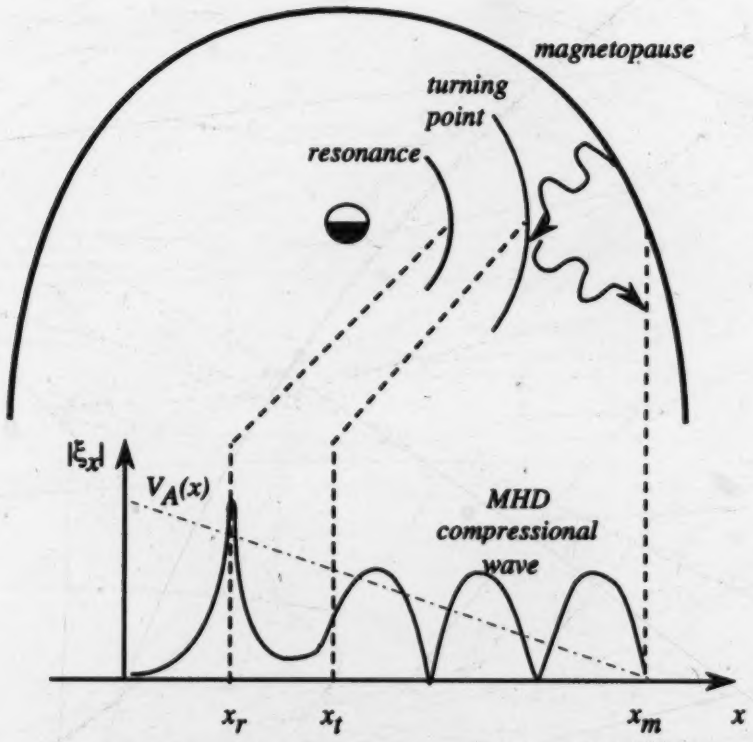

Figure 1.6. Schematic of field line resonance coupling. ξ_x represents the radial displacement of the plasma.

The strength of the coupling between the fast compressional and shear Alfvén wave modes depends upon the size of the azimuthal wave number, k_y. For k_y=0, the two modes are decoupled and no energy is transferred from the fast to the shear Alfvén wave

and thus no FLR results. As k_y becomes larger, the distance from the turning point, x_t, to the resonance point, x_r, increases. The evanescent compressional wave continues to decay over the increased distance and reaches the resonance location with a much smaller amplitude. Therefore, less wave energy reaches the resonance. In the limit $k_y \rightarrow \infty$, the modes are again completely decoupled. The most efficient coupling occurs for a small range of k_y values. The coupling efficiency is determined by the amount of energy absorbed by the shear Alfvén resonance. The energy absorption as a function of the dimensionless coupling parameter

$$Q = \frac{k_y^2}{\left[k_z^2 V_A^2 \frac{d}{dx}(V_A^{-2})\right]^{2/3}} \tag{1.68}$$

has been calculated numerically by Speziale and Catto [1977], and Forslund et al. [1975]. A plot of the absorption versus Q is shown in Figure 1.7(a). It is instructive to determine what the coupling parameter values correspond to in terms of an azimuthal wave number. The azimuthal wave number, m, represents the number of azimuthal wavelengths which would fit around the Earth. Thus k_y and m are related by

$$k_y = \frac{2\pi}{\lambda_y} = \frac{2\pi m}{2\pi x_r} = \frac{m}{x_r} \tag{1.69}$$

where λ_y is the azimuthal wavelength. Substituting (1.69) into (1.68) and using an Alfvén velocity profile proportional to x^{-1} yields

$$Q = \frac{m^2}{x_r^2\left[k_z^2\left(\frac{2}{x_r}\right)\right]^{2/3}} = \frac{m^2}{(2x_r^2 k_z^2)^{2/3}} \quad . \tag{1.70}$$

This relation is plotted in Figure 1.7(b) for a resonance location of 10 R_E and a reasonable field-aligned wave vector of k_z=0.1 R_E^{-1}. Comparing Figures 1.7(a) and 1.7(b) we can see that efficient coupling occurs for azimuthal wave numbers in the approximate range 0.5-2.0, with no coupling for m=0 and $m \rightarrow \infty$. This result suggests that FLRs generated by the compressional-shear coupling mechanism should exist only for azimuthal wave numbers in the above defined range. However, as will be shown in Chapter 2, FLRs with m values as large as 30 are often observed. A discussion of high-m mode coupling and its unique characteristics are presented in Chapter 3.

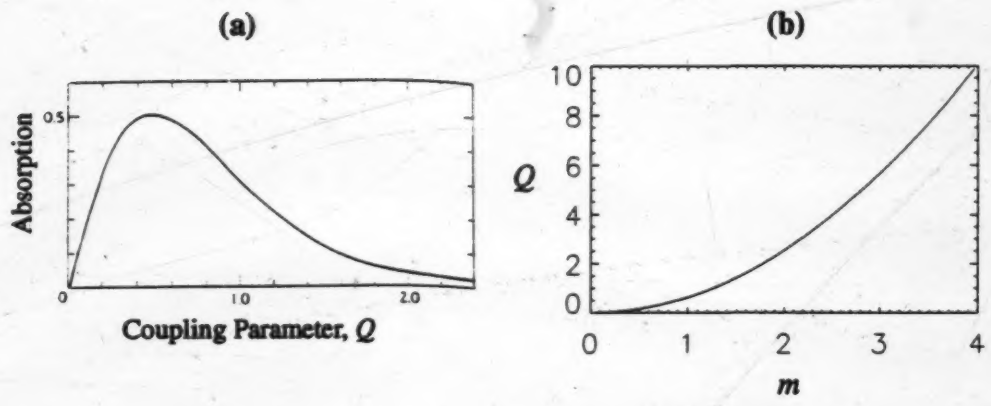

Figure 1.7. (a) Resonance absorption versus coupling parameter, Q, [from Kivelson and Southwood, 1986]. (b) Plot of Q versus azimuthal wave number, m.

1.2.4 Field Line Resonance Characteristics

FLRs have a number of distinguishing characteristics. They exhibit an inverse relationship between frequency and latitude, i.e. lower frequency FLRs occur at higher latitudes. In the region of the magnetosphere where the resonances discussed in this thesis are observed, between ~8-12 R_E in the equatorial plane, the gradients in magnetic field strength and plasma densities result in an Alfvén velocity profile which decreases monotonically with radial distance. The field aligned wave vector, k_z, which is inversely proportional to the field line length also decreases with increasing radial distances. Thus the standing shear Alfvén wave frequency, defined by

$$\omega = V_A k_z, \tag{1.71}$$

must also decrease with increasing distances from the Earth. Since larger radial distances map to higher latitudes, the inverse relationship between frequency and latitude results.

With a monochromatic compressional mode driving the resonance, the resonance will be localized in the radial direction and therefore latitudinally localized as well. This localization can be seen in Figure 1.5. From equation (1.67), one can derive an expression relating the width of the resonance to the magnitude of ε. This expression is

$$FWHM = 2\sqrt{3}|\varepsilon| \tag{1.72}$$

where *FWHM* represents the full width of the resonance at half its maximum. Observations have shown typical resonance *FWHM* values to be on the order of 1° latitude at the ionosphere which corresponds to a *FWHM* of ~1 R_E at an L value of 10 R_E based upon a dipole field model. According to (1.72) a FWHM value of 1 R_E gives $|\varepsilon| = 0.3\ R_E$. Therefore, this was the value used in calculating E_x for Figure 1.5 and one can see from Figure 1.5 that the *FWHM* is indeed ~ 1R_E.

The phase of the resonant wave fields as a function of latitude or radial position is an important feature used to identify FLRs. The phase corresponding to the radial component of the resonant electric field, E_x, is shown as a function of radial position in Figure 1.8. This figure shows the characteristic decrease in phase of ~180° as the resonance is crossed radially (latitudinally) from smaller x (lower latitude) to larger x (higher latitude). Note that this solution corresponds to the case where the azimuthal wave number is small and the resonance is being driven externally. However, the phase variation with latitude has been found to depend upon the size of k_y. FLRs with large ky values were found to exhibit an increasing rather than a decreasing latitudinal phase shift. Observations confirming this are presented in Chapter 2 and its cause is discussed in Chapter 3. In addition to the latitudinal phase changes being dependent upon the azimuthal wave vector, k_y, there are additional k_y dependent characteristics. When k_y is small the FLR is termed a toroidal resonance since it is dominated by toroidal wave fields, i.e. the wave electric fields are radial while the wave velocity and magnetic fields are azimuthal. When k_y is large the resonance is primarily poloidal, i.e. the wave electric fields are azimuthal while the velocity and magnetic fields are radial. For intermediate k_y values the resonance is a combination of toroidal and poloidal modes. In all cases the fields must satisfy boundary conditions at the ionosphere. The boundary conditions dictate that the electric and velocity fields have a node at the ionosphere while the magnetic field has an antinode there. The characteristics of the wave fields between the ionospheres will depend upon whether the shear Alfvén wave is a fundamental or higher harmonic along the field line. Figure 1.9 is a schematic of the wave fields of a toroidal FLR which is in a fundamental mode along the magnetic field line.

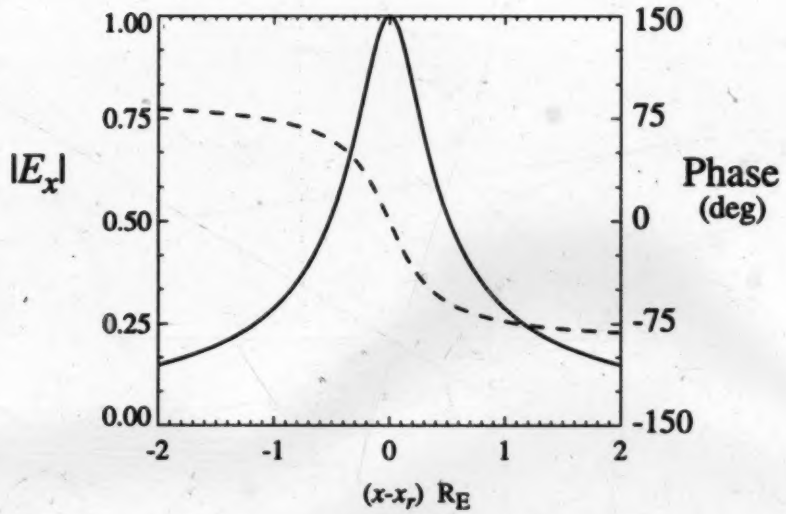

Figure 1.8. Phase (dashed) and amplitude (solid) of E_x across resonance.

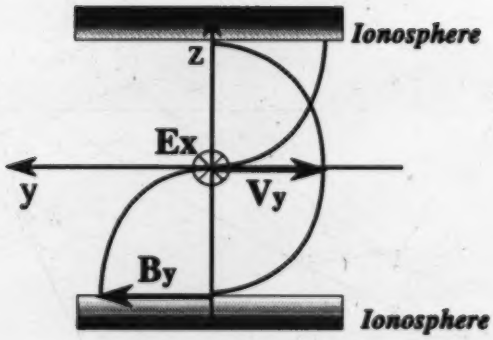

Figure 1.9. Fundamental wave fields of a toroidal FLR

1.2.5 Discussion of Previous Work on FLRs

In the theories developed to explain the occurrence of FLRs in the magnetosphere, there has been one issue that has remained unresolved: the source of the compressional modes responsible for driving the FLRs. It was initially suggested that surface waves on the magnetopause generated by solar wind driven Kelvin-Helmholtz instabilities were initiating the compressional modes [*Chen and Hasegawa*, 1974; *Southwood*, 1974]. However, such a source would be fairly broad-band thus exciting a continuum of FLRs. Although there is evidence of such a continuum at low powers [*Waters et al.*, 1994], observations have consistently shown the existence of discrete FLRs at powers well above the background. Recent observations of FLRs in HF coherent scatter radar data [*Ruohoniemi et al.*, 1991; *Walker et al.*, 1992; *Samson et al.*, 1992a], ground-based magnetometer data [*Ziesolleck and McDiarmid*, 1994; *Samson et al.*, 1991], and simultaneously in VHF coherent scatter radar and ground- and satellite-based magnetometer data [*McDiarmid et al.*, 1994], have shown not only the discrete nature of the FLRs but also that the same frequencies occur repeatedly on different days at different local times during various magnetic conditions. The most commonly observed reproducible frequencies were 1.3, 1.9, 2.6, and 3.3 mHz with uncertainties of less than 10%.

The first attempts to explain the quantization of the resonance frequencies were made by *Kivelson et al.* [1984] and *Kivelson and Southwood* [1985]. They proposed a cavity mode theory where the discrete FLRs correspond to eigenmodes of a magnetospheric cavity. However, a cavity implies boundaries in all three dimensions. With no potential boundaries in the azimuthal direction the cavity model was modified into a waveguide model by *Samson et al.* [1992b] and *Wright* [1994] to account for the azimuthal propagation of the compressional modes. A picture of the magnetospheric waveguide model is shown in Figure 1.10.

In the waveguide model a source disturbance in the magnetosphere generates the compressional modes with the inner turning point and possibly the magnetopause providing the waveguide boundaries. It is not certain what type of disturbance excites the waveguide, but potential sources include pressure pulses in the solar wind, Kelvin-Helmholtz instabilities in the low-latitude boundary layer, or plasma instabilities associated with substorms and reconnection. The monochromatic eigenmodes generated by the waveguide couple to the field line resonances, thus explaining the discrete nature of the observed resonance frequencies.

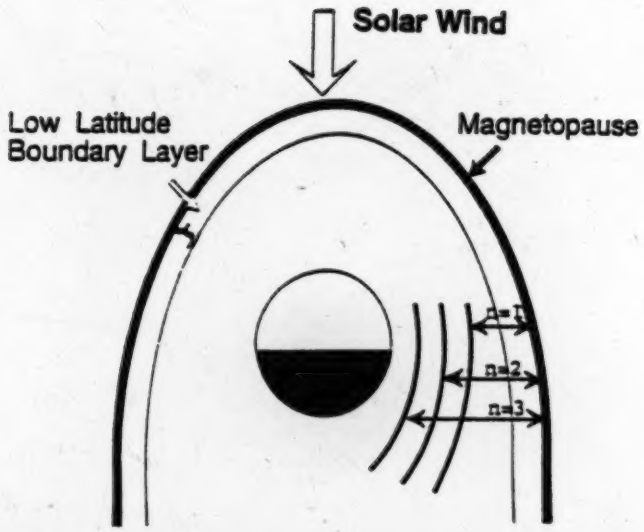

Figure 1.10. Magnetospheric waveguide model [from *Samson et al.*, 1992b]. The solid lines near the Earth represent the turning points for the first three eigenmodes (n=1,2,3) of the waveguide.

The eigenfrequencies of the magnetospheric waveguide can be estimated by using a WKB solution to the equation governing the resonance. The WKB solution to equation (1.55) is given by

$$E_y(x) = AK^{-1/2}e^{i\int Kdx} + BK^{-1/2}e^{-i\int Kdx} \tag{1.73}$$

where, as defined previously,

$$K^2 = \frac{\omega^2}{V_A^2} - k_z^2 - k_y^2 \tag{1.74}$$

and A and B are constants determined by boundary conditions. The compressional

eigenmode solution must match the solution at the turning point where the wave is reflected with a 90° phase shift [Samson et al., 1992b; Walker et al., 1992]. The boundary at the magnetopause is considered a fixed boundary because of the large changes in plasma density and magnetic field. In the WKB approximation the phase integral when integrated across the waveguide will correspond to the change in phase of the standing compressional eigenmode from the magnetopause to the turning point. Since the standing compressional eigenmode must have a node at the magnetopause and must match the turning point solution with a 90° phase shift, the change in phase from the magnetopause to the turning point is given by (n-1/4)π. Thus the phase integral must satisfy

$$\int_{x_t}^{x_m} K dx = (n - \frac{1}{4})\pi \quad . \tag{1.75}$$

Samson [1992b] used both the phase integral approach as well as numerical solutions to derive the first four harmonic frequencies of a model magnetospheric waveguide and found them to be compatible with the commonly observed frequencies listed above.

Although the concept of a magnetospheric waveguide or cavity is very successful in explaining the discreteness of the FLRs, there are many deficiencies in the model when it comes to explaining all observations. The extreme stability and reproducibility of the FLRs is inconsistent with a dynamic magnetosphere. The dimensions and conditions of the magnetosphere are continually changing. Thus it is inconceivable that a magnetospheric waveguide could produce the same stable resonance frequencies at different local times, day after day, year after year. Also, any magnetospheric waveguide system is going to be very dispersive, i.e. its eigenfrequencies are going to vary strongly with k_y. However, according to observations, which are presented in the next chapter, reproducible FLRs occur over a wide range of k_y values. An additional deficiency of the magnetospheric waveguide model is that the predicted frequencies for realistic magnetospheric conditions tend to be substantially larger than the observed FLR frequencies. A discussion of the full extent of the problems concerning the magnetospheric waveguide model as a source for the monochromatic compressional modes is deferred to Chapter 4 where other scenarios concerning the driving mechanism will be explored. However, before any new ideas about the source can be postulated it is first necessary to fully investigate the observable characteristics of the FLRs. Thus an observational study of numerous FLR events has been undertaken using the Super Dual Auroral Radar Network (SuperDARN) of HF radars. The methods and results of this study are the topic of the next chapter.

2

Observations of Discrete Field Line Resonances Using The Super Dual Auroral Radar Network[1]

In order to better understand the discrete FLR phenomenon, an observational study of field line resonance events has been completed using the Super Dual Auroral Radar Network (SuperDARN) of HF radars. In the following chapter the methods and results of this study will be presented. It will be shown that the FLRs fall into one of two categories: those with small azimuthal wave number and those with large azimuthal wave number. The high- and low-*m* events share many common features. They both have the same discrete and reproducible frequency spectrum, with the most common frequencies being 1.3, 1.9, and 2.5 mHz. Both types of event are localized in latitude with lower frequency FLRs occurring at higher latitudes. The high- and low-*m* FLRs also have some distinct differences the most notable being their latitudinal phase shifts which are decreasing for all low-*m* FLRs and increasing for all high-*m* FLRs. A complete description of the similarities and differences between these two types of resonances and their implications concerning a generation mechanism will be given.

2.1 Data Acquisition and Analysis Methods

The data used in this study were acquired by three of the operational HF radars of SuperDARN. These radars included the Johns Hopkins University/Applied Physics Laboratory (JHU/APL) radar at Goose Bay, which has been in operation since 1983, plus an overlapping pair of radars located at Saskatoon and Kapuskasing which began operation in mid 1993. The fields-of-view of these radars are shown in Figure 2.1. The Saskatoon, Kapuskasing, and Goose Bay radars are denoted by the prefixes T, K, and G, respectively. For a detailed description of the SuperDARN HF radars see Greenwald et al. [1995].

---

1. A version of this chapter has been published. F. R. Fenrich, J. C. Samson, G. Sofko, R. A. Greenwald, ULF high- and low-*m* field line resonances observed with the Super Dual Auroral Radar Network, *J. Geophys. Res.*, *100*, 21535-21547, 1995.

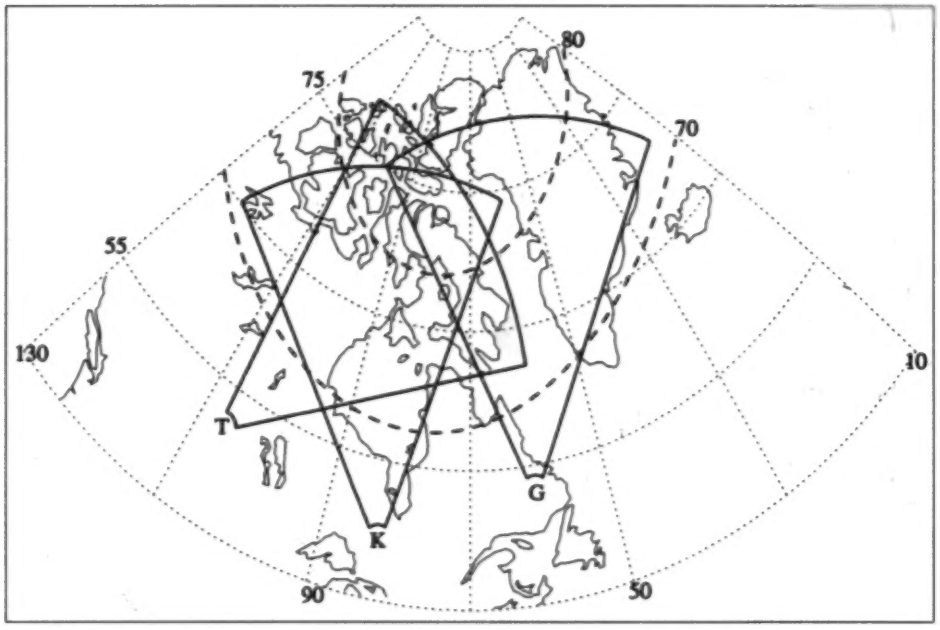

Figure 2.1. Fields-of-view of the Super Dual Auroral Radar Network (SuperDARN) radars at Goose Bay (G), Kapuskasing (K), and Saskatoon (T) plotted in geographic coordinates. The heavy dashed lines are Polar Anglo-American Conjugate Experiment (PACE) magnetic latitude contours [*Baker and Wing*, 1989].

Each radar consists of 16 log periodic antennas operating in the 8-20 MHz band. At any instant, a single beam is formed. By means of a phasing matrix, the beam is advanced through 16 successive azimuths with an angular separation of 3.24 degrees, giving a total azimuthal field of view of about 52 degrees. The beams of each radar are numbered 0 to 15, going from the westernmost to the easternmost beam. At each beam azimuth, the integration time is 6.25 s, yielding a sampling interval of about 100 s per complete 16-beam scan. For the pre-1990 Goose Bay data presented, the integration time was 6 s per beam for normal scans, with every fourth scan including a calculation of the elevation angle of arrival which doubled the integration time to 12 s per beam. At each beam azimuth the SuperDARN radars transmit a 5 to 7 pulse sequence over a 100 ms time period. The returned backscatter from the pulse sequence is sampled and processed to produce multi-lag autocorrelation functions as a function of range. The autocorrelation functions are then fitted to determine the backscattered power, the mean

Doppler velocity, and the width of the Doppler power spectrum for each range gate where there is significant backscatter. The radar beams have a maximum of 75 range gates spaced 45 km apart.

Figure 2.2 is an illustration of the manner in which VHF (30-300 MHz) and HF (3-30 MHz) signals are scattered by field aligned electron density irregularities in the ionosphere [*Fejer and Kelley*, 1980]. The HF frequencies refract towards the horizontal as they enter the ionospheric layers. If the HF signals are propagating perpendicular to the magnetic field when they encounter the electron density irregularities, the backscattered signals will return to the radar. In the F region the irregularities are at rest with respect to the background convection of the plasma [*Ruohoniemi et al.*, 1987]. Therefore, the measured Doppler velocities represent the bulk flow of the ionospheric plasma. Note that single beams can only measure the line-of-sight Doppler velocity, i.e. that component of the plasma flow along the beam direction. However, the overlap between SuperDARN radar pairs allows for the determination of total velocity vectors in the plane perpendicular to the magnetic field line. Since plasma convection is perpendicular to the Earth's magnetic field the overlapping SuperDARN radars measure the two-dimensional plasma convection pattern in the ionosphere.

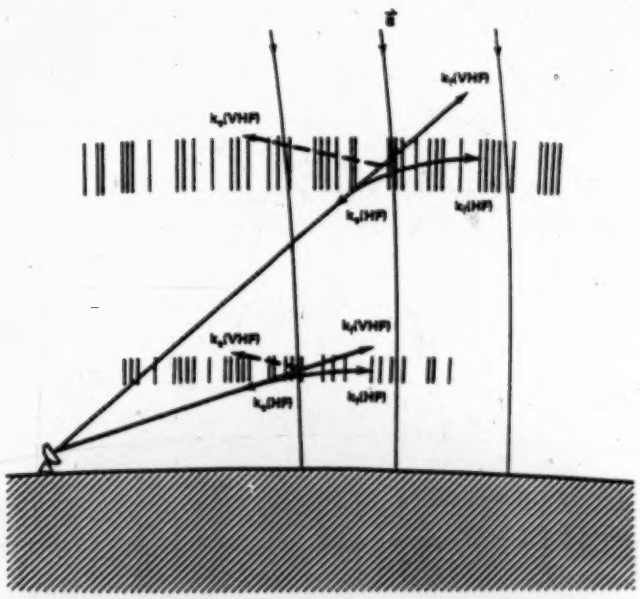

Figure 2.2. Illustration of the scattering of VHF and HF signals by the ionosphere (Taken from *Greenwald et al.* [1995]).

The SuperDARN system of coherent scatter HF radars provides an exceptional tool for analyzing field line resonances. The ULF oscillations in the *F* region plasma flows, which are associated with the field line resonances, are observable in the measured line-of-sight Doppler velocities. Data analysis began by scanning range-time plots of the line-of-sight Doppler velocity data in order to find periods of good scatter where ULF pulsations in the velocity were apparent. Figures 2.3 and 2.4 show two examples of range-time plots exhibiting ULF pulsations.

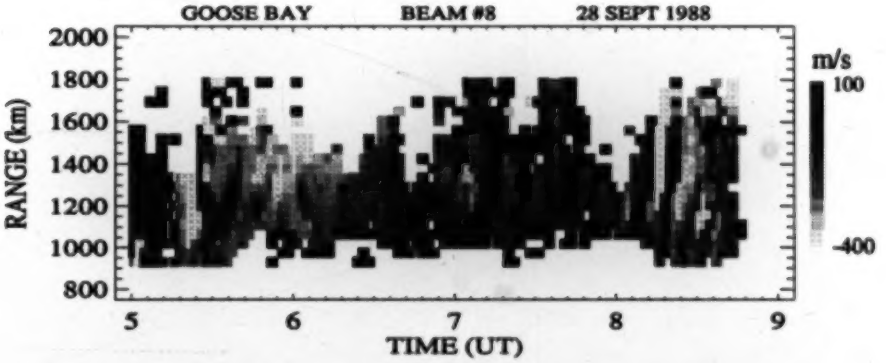

Figure 2.3. Range-time plot of the line-of-sight Doppler velocity along beam 8 of Goose Bay for the time interval 0500-0900 UT on September 28, 1988. Note the poleward moving bands of oscillation between 0740 and 0840 UT. Magnetic local times are approximately UT minus 3 hours for Goose Bay.

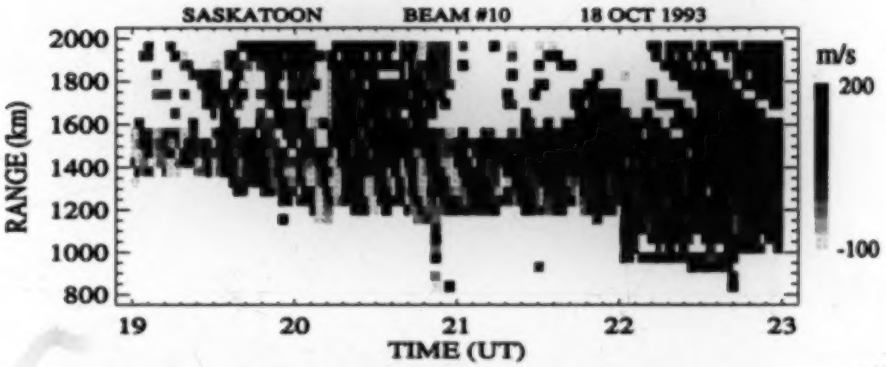

Figure 2.4. Range-time plot of the line-of-sight Doppler velocity along beam 10 of Saskatoon for the time interval 1900-2300 UT on October 18, 1993. Note the equatorward moving bands of oscillation between 1930 and 2200 UT. Magnetic local times are approximately UT minus 7 hours for Saskatoon.}

Once a period of interest was identified, the data for each beam was selected over the range and time interval exhibiting good scatter. A two-dimensional interpolation of the raw range-time data set was then performed to fill in small data gaps which were typically no larger than a few points. Data sets with large gaps were not used. In order to determine the spectral components present in the data, 32 or 64 point time series were detrended, high-pass filtered ($f > 0.5$ mHz), and then fast Fourier transformed. The 32 point time series were used most often since the resonance events generally had a time duration of ~1 hour which corresponds to ~32 data points given the 100 second resolution of the data. Contour plots of power spectra for various FLR events are shown in Figures 2.5 and 2.6. Note the reproducibility of the FLR frequencies (shown by the dashed lines).

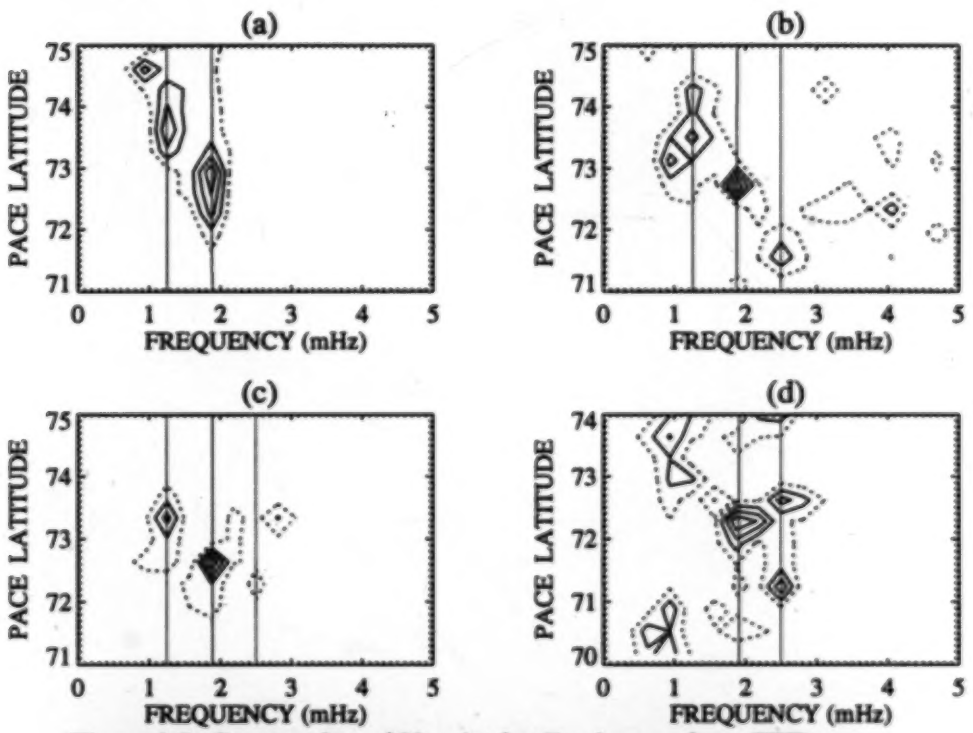

Figure 2.5. Contour plots of 32-point fast Fourier transform (FFT) power spectra taken at numerous gates for (a) beam 8 of Goose Bay during the time interval 0735-0835 UT on September 28, 1988, (b) beam 5 of Saskatoon during the time interval 2220-2320 UT on October 6, 1993, (c) beam 9 of Saskatoon during the time interval 1948-2048 UT on October 18, 1993, and (d) beam 8 of Kapuskasing during the time interval 0000-0100 UT on February 2, 1994. The range values are given in PACE magnetic latitude coordinates, and the spectra are normalized to ten with the contour lines drawn at 2 (dashed), 4, 6, 8, and 10. The dotted lines indicate the spectral frequencies which were identified as FLRs. Figures 2.5a and 2.5d represent low-m events, while Figures 2.5b and 2.5c represent high-m events.

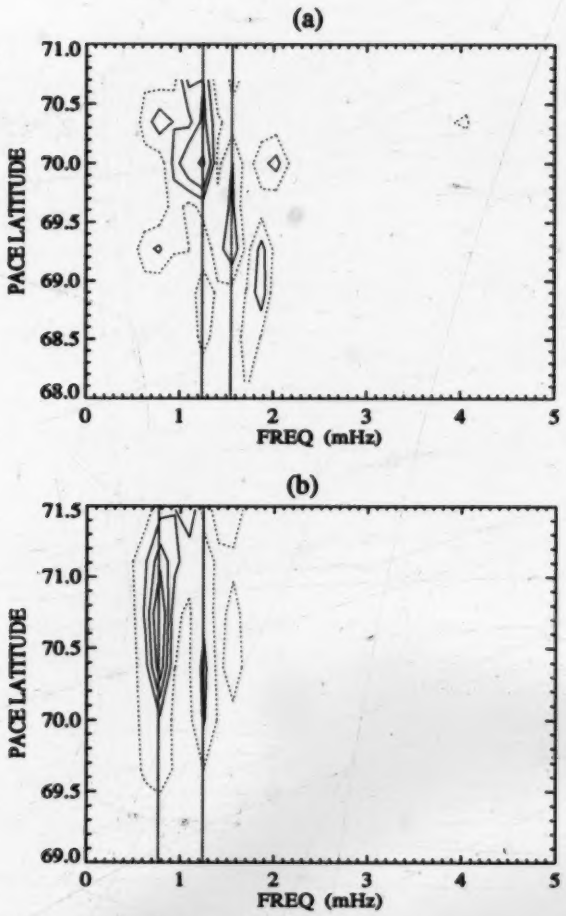

Figure 2.6. Contour plots of 64-point fast Fourier transform (FFT) power spectra taken at numerous gates for (a) beam 11 of Saskatoon during the time interval 0210-0400 UT on October 23, 1994, (b) beam 8 of Goose Bay during the time interval 0315-0505 UT on October 14, 1989. The spectra are normalized to ten with the contour lines drawn at (a) 2, 4, 6, 8, and (b) 1, 3, 5, 7. The dotted lines indicate the spectral frequencies which were identified as FLRs. Figure 2.6a is a low-*m* event, while figure 2.6b is a high-*m* event.

Measurements of the power and phase of the observed spectral peaks as a function of latitude were made to identify potential FLRs. Examples of such measurements are shown in Figure 2.7. The power spectra are normalized to an arbitrary amplitude. The error bars represent statistical estimates of uncertainties in spectral power and phase calculated in the same manner as *Walker et al.* [1979]. The mean spectral power is calculated for each time series according to

$$P = \frac{1}{n}\sum_{i=1}^{n} P_i \tag{2.1}$$

where P_i is the spectral power at each of the n frequency points. The calculation is then repeated, dropping the points for which $P_i > 2P$. The resulting power, P', is an estimate of the noise and is used as the uncertainty in the spectral power. The uncertainty in the spectral phase, $\delta\phi$, is approximated by

$$\delta\phi = \text{atan}\left[(P'/P_i)^{1/2} \right] \tag{2.2}$$

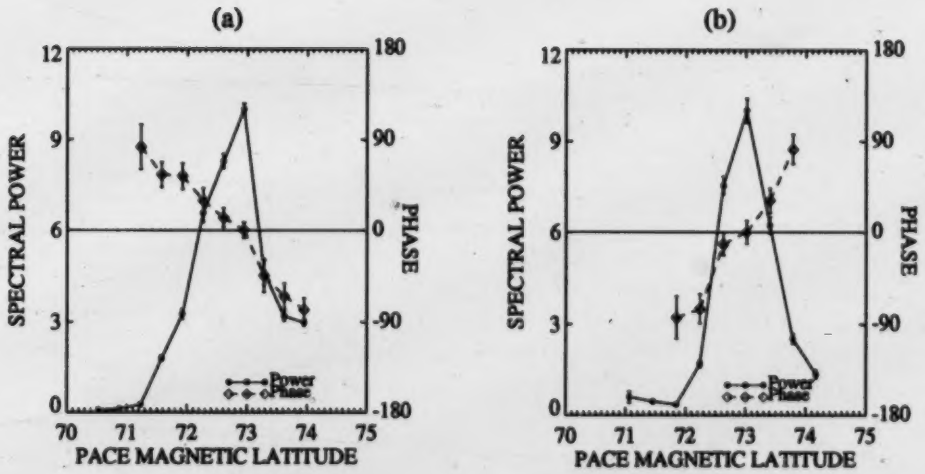

Figure 2.7. (a) Latitude profile of the spectral power and phase at 1.9 mHz along beam 8 of Goose Bay for the time interval 0735-0835 UT on September 28, 1988 (a low-m event). (b) Latitude profile of the spectral power and phase at 1.3 mHz along beam 3 of Saskatoon for the time interval 2120-2220 UT on October 18, 1993 (a high-m event). Note the difference in phase variation between Figures 2.7(a) and 2.7(b).

It should be noted that care was taken in using the data from a single beam of the radar to determine the phase variation with latitude since azimuthal phase variations can contaminate the measurement if the beam is not directed perpendicular to the latitudinal contour of the resonance. However, in some cases the perpendicular direction was also the direction of minimum amplitude in the measured Doppler oscillations. Therefore phase variations with latitude were determined using beams which differed as little as possible from the perpendicular direction to the resonance contour in order to minimize the influence of azimuthal phase variations while maintaining sufficient amplitude.

If an observed spectral component corresponds to a field line resonance, it should exhibit a narrow maximum in power and a phase decrease of ~180 degrees across this maximum. Note the reverse phase shift in Figure 2.7(b). This was a very interesting feature characteristic of all high-m resonances and will be discussed in detail in the following sections. Also, since a FLR is extended azimuthally along a single L shell, it should be visible on a number of the radar beams at approximately the same geomagnetic latitude. Therefore, if a similar analysis of numerous beams in the radar array yielded the same frequency component with the same FLR characteristics, then the pulsation was identified as a FLR and analyzed in more detail using analytic signal techniques.

The analytic signal $A(t)$ corresponding to a given time series $f(t)$ is defined by

$$A(t) = f(t) - iH(t) \quad , \tag{2.3}$$

where $H(t)$ is the Hilbert transform of $f(t)$. The characteristics of the analytic signal are described in detail by *Walker et al.* [1992]. Essentially, the analytic signal separates the amplitude information from the phase information, allowing one to instantaneously measure the amplitude, phase, and frequency of a given spectral component. For this method to be useful the data must be quasi-monochromatic and therefore the data were first band-pass filtered in the time domain. To accomplish this the band-pass filter was centered on the frequency of interest with a bandwidth of 0.6 mHz. This width was chosen to be as narrow as possible in order to isolate the resonance frequency, yet wide enough to allow any shifts in the frequency to be observable. In the analysis of a particular resonance, the analytic signal amplitude was calculated for each beam at the range gate where a given field line resonance was a maximum, as shown in Figure 2.8. The instantaneous phase of the resonance was then measured along each of the beams yielding a phase versus longitude relation. The phase errors were calculated using equation (2.2). An example of phase versus longitude measurement is shown in Figure

2.9. The slope of this relation gives the azimuthal wave number, m. The 95% confidence interval in the slope was calculated to determine the accuracy of the m value. Note that small slope values and therefore small m values generally have a larger percentage error associated with them, given that the errors in phase are independent of the m value. The m value and the resonance frequency were then used to calculate the azimuthal phase velocity. Calculation of cross-correlations between the analytic signal amplitude envelopes yielded lag times of the resonance wave packet as a function of longitude (see Figure 2.10) from which azimuthal group velocities were estimated. Errors in the lag times were estimated from the width of the cross-correlation functions.

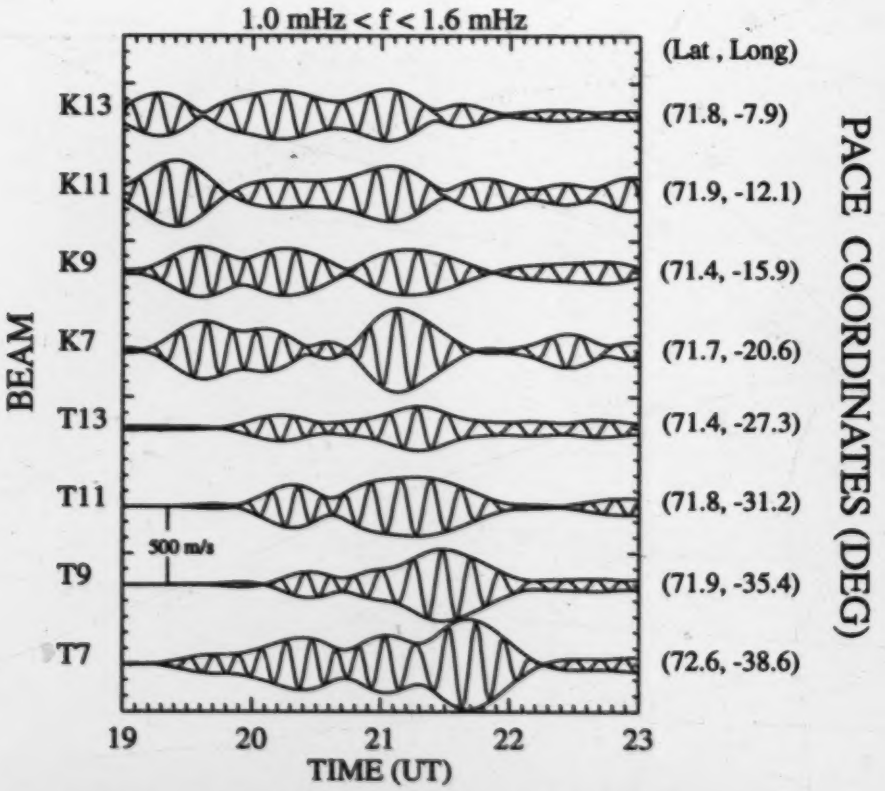

Figure 2.8. Stack plot of the analytic signal amplitude envelopes for various beams of Kapuskasing (K) and Saskatoon (T) at the range gates where the 1.3-mHz resonance was at its maximum on October 18, 1993, during the time interval 1900-2300 UT. The coordinates corresponding to the gate values used are listed on the right side of the figure in PACE magnetic coordinates. Note that this resonance was seen on both Kapuskasing and Saskatoon at ~71.8 degrees magnetic latitude with the maximum in the wave packet structure appearing earlier on the larger beams of Kapuskasing indicating westward propagation.

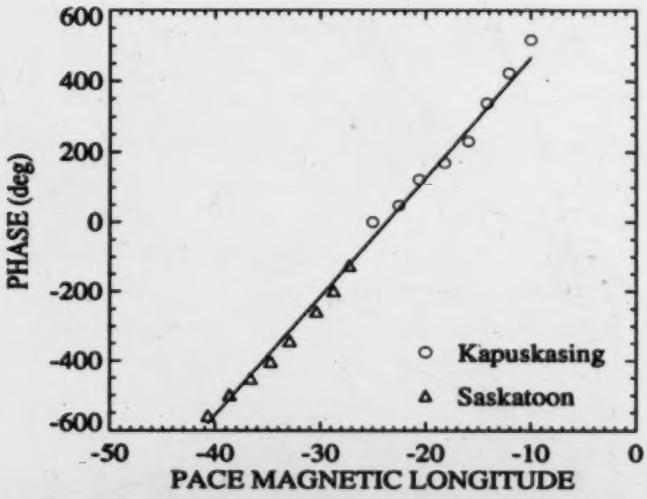

Figure 2.9. Plot of phase versus longitude measured at 2120 UT for the 1.3-mHz resonance of October 18, 1993. The errors in the instantaneous phase measurements fall within the size of the symbols and therefore are not shown. The slope of this relation yields the azimuthal wave number, m, which in this case is ~34 and corresponds to a westward phase velocity of ~0.5 km/s at the ionosphere.

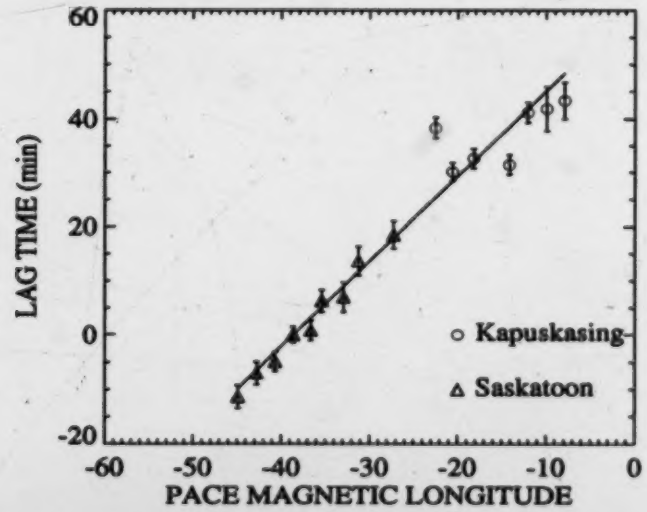

Figure 2.10. Plot of lag times of the resonance wave packet versus longitude for the 1.3-mHz resonance of October 18, 1993. The lag times were determined from calculation of the cross correlations between analytic signal amplitude envelopes, as shown in Figure 2.8, for the time interval 2000-2320. The positive slope indicates a westward group propagation of ~0.3 km/s at the ionosphere.

Although the SuperDARN system of radars was designed to provide the total velocity vectors for the plasma flow using intersecting beams from overlapping radars, we were unable to analyze the majority of resonance events using data from intersecting beams for the following reasons. Of course, for the events before 1993, only the Goose Bay radar was in operation. During the first 8 months of operation of the Saskatoon-Kapuskasing radar pair, when the majority of the events were observed, the amount of good scatter from the *F* region was very limited. This was believed to be due to changes in the ionospheric electron densities during the sunspot minimum of the solar cycle. In addition, the beams of Saskatoon and Kapuskasing have substantial overlap only at latitudes greater than approximately 70 degrees PACE magnetic latitude. Therefore total velocity vectors for resonances at latitudes lower than this cannot be determined. Thus the resonance events in this paper have been analyzed for the most part with line of sight velocities provided by single radars.

In the few instances where good ionospheric scatter was observed on both the Saskatoon and Kapuskasing radars during an FLR event, a merge of the line-of-sight velocity data from each of the two radars was possible. The overlapping field of view of the radar pair is separated into a 16x16 grid defined by the intersection of the radar beams. Figure 2.11 is a geographic plot of the Saskatoon-Kapuskasing merge grid. Within each grid box the velocities measured by each radar are averaged. Since the radar beam directions are known, the average velocities from each radar can be combined to yield total velocity vectors at the center of each grid box.

2.2 Observations

The results of the analysis of 15 FLR events are summarized in Table 2.1. Corresponding composite pictures of the azimuthal phase velocities mapped to the equatorial plane using both a dipole model and the Tsyganenko 87 [*Tsyganenko*, 1987] model are shown in Figures 2.12(a) and 2.12(b), respectively. The events were found to occur on both the dayside and nightside of the magnetosphere during predominantly quiet days with most events occurring when $Kp \leq 3$. ULF pulsations were observed on more active days, but the structures were not stable enough to be observed across a large portion of the radar and therefore could not be identified as FLRs.

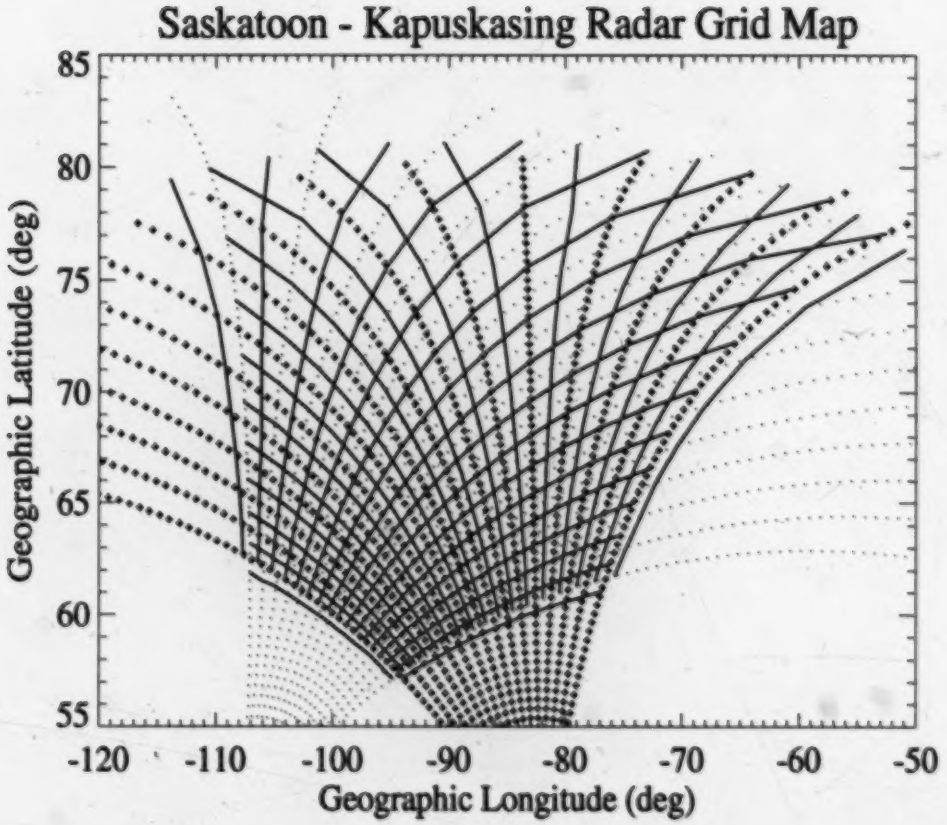

Figure 2.11. Plot of the Saskatoon-Kapuskasing merge grid. The cross symbols correspond to the range gates of the Kapuskasing radar, while the dots correspond to the range gates of the Saskatoon radar.

Table 2.1. FLR Study Analysis Results

Event No.	Day	Time Interval UT	Radar[a]	*Kp*	Freq mHz	*m*[b]	PACE Latitude	Azimuthal Phase Velocity[c] km/s	Azimuthal Group Velocity[c] km/s	Phase Variation With Latitude[d]
1a	Sept. 28, 1988	0740-0840	G	1	1.3	3 ± 1	73.5	5.2	2.2 ± 0.8	standard
1b	Sept. 28, 1988	0730-0850	G	1	1.9	6 ± 2	72.4	4.0	-	standard
2a	Sept. 30, 1988	0630-0730	G	2+	1.0	4 ± 1	74.0	2.9	-	standard
2b	Sept. 30, 1988	0700-0810	G	2+	1.6	6 ± 2	73.8	3.1	1.4 ± 1.0	standard
2c	Sept. 30, 1988	0650-0810	G	2+	1.9	13 ± 2	73.5	1.7	-	standard
3a	Jan. 11, 1989	0550-0700	G	1+	0.8	-	72.5	-	-0.4 ± 0.2	standard
3b	Jan. 11, 1989	0550-0700	G	1+	1.3	5 ± 2	72.0	3.4	0.7 ± 0.4	standard
3c	Jan. 11, 1989	0550-0700	G	1+	1.9	10 ± 2	71.0	2.7	0.5 ± 0.2	standard
3d	Jan. 11, 1989	0550-0700	G	1+	2.6	-5 ± 2	69.8	-7.5	-3.0 ± 1.0	standard
3e	Jan. 11, 1989	0550-0700	G	1+	3.3	-	69.4	-	-	standard
4a	Oct. 14, 1989	0300-0420	G	0+	0.8	12 ± 3	70.4	0.9	-	standard
4b	Oct. 14, 1989	0310-0430	G	0+	1.3	30 ± 2	69.9	0.6	-	reverse
4c	Oct. 14, 1989	0310-0430	G	0+	1.9	20 ± 3	69.4	1.4	-	reverse
5a	Oct. 6, 1993	2200-2330	T	3-	1.3	17±2→9±3	73.2	0.9→1.7	0.4 ± 0.1	reverse→standard
5b	Oct.6, 1993	2230-2340	T	3-	1.6	14 ± 2	72.0	1.5	0.6 ± 0.3	-
5c	Oct. 6, 1993	2200-2330	T	3-	1.9	21±2→3±5	72.8	1.1→7.8	0.3 ± 0.1	reverse→standard
5d	Oct. 6, 1993	2230-2340	T	3-	2.5	25 ± 1	71.7	1.3	1.2 ± 0.2	reverse
5e	Oct. 6, 1993	2230-2340	T	3-	3.6	40 ± 9	71.7	1.2	0.7 ± 0.5	reverse
6a	Oct. 18, 1993	1840-2040	K	1	1.3	19 ± 1	72.6	0.9	0.3 ± 0.1	reverse
6b	Oct. 18, 1993	1950-2210	T&K	1	1.3	34 ± 2	72.5	0.5	0.3 ± 0.1	reverse
6c	Oct. 18, 1993	1900-2140	T&K	1	1.5	26 ± 2	72.8	0.7	0.8 ± 0.3	reverse
6d	Oct. 18, 1993	1910-2140	T&K	1	1.9	31 ± 2	72.8	0.8	0.4 ± 0.1	reverse
6e	Oct. 18, 1993	1920-2150	T&K	1	2.5	36 ± 2	72.5	0.9	-0.3 ± 0.1	reverse

Dashes indicate values could not be determined. PACE is the Polar Anglo-American Conjugate Experiment.

[a] G, GooseBay; K, Kapuskasing; T, Saskatoon.

[b] Azimuthal wave number. The errors correspond to the 95% confidence interval.

[c] Velocities are calculated at the ionosphere with negative values indicating eastward propagation. Errors in phase velocity can be determined from the corresponding errors in m given that $V_{ph} = \omega/k$. The errors in group velocity are estimated from the 95% confidence interval in the slope measurements of lag time versus longitude.

[d] Standard refers to a phase decrease with increasing latitude; reverse refers to a phase increase with increasing latitude.

Table 2.1. FLR Study Analysis Results Continued

Event No.	Day	Time Interval UT	Radar[a]	*Kp*	Freq mHz	*m*[b]	PACE Latitude	Azimuthal Phase Velocity[c] km/s	Azimuthal Group Velocity[c] km/s	Phase Variation With Latitude[d]
7	Nov. 18, 1993	1550-1730	T	6	1.9	-27 ± 15	68.2	-1.1	-	reverse
8	Dec. 16, 1993	0320-0450	K	4-	1.9	28 ± 6	70.2	1.0	-	reverse
9	Dec. 29, 1993	0000-0140	K	1	1.3	23 ± 2	73.3	0.7	-	reverse
10	Jan. 11, 1994	1320-1500	T	3	2.8	7 ± 2	69.8	5.8	-	standard
11a	Feb. 2, 1994	0000-0110	K	1-	1.9	-7 ± 2	72.3	-3.5	-	standard
11b	Feb. 2, 1994	0000-0110	K	1-	2.5	-3 ± 1	71.2	-11.7	0.7 ± 0.3	standard
11c	Feb. 2, 1994	0050-0150	K	1-	2.6	-5 ± 3	70.2	-7.4	1.1 ± 0.5	standard
12	Feb. 5, 1994	1500-1650	G	4	2.2	16 ± 5	70.2	2.0	0.2 ± 0.1	standard
13a	Oct. 23, 1994	0030-0200	T	6	1.3	-5 ± 1	70.1	−3.7	−0.7 ± 0.6	standard
13b	Oct. 23, 1994	0030-0200	T	6	1.5	-7 ± 5	69.8	−3.1	−0.7 ± 0.4	standard
13c	Oct. 23, 1994	0030-0200	T	6	2.2	-6 ± 2	67.3	−5.9	-	standard
13d	Oct. 23, 1994	0120-0240	T	6	2.5	-4 ± 1	67.6	−10.0	-	standard
13e	Oct. 23, 1994	0230-0350	T	5+	1.3	-12 ± 1	70.0	−1.5	-	standard
13f	Oct. 23, 1994	0230-0350	T	5+	1.5	-12 ± 1	69.7	−1.8	−1.0 ± 0.3	standard
14	Feb 09, 1995	0000-0130	T	3+	1.9	-2 ± 1	71.2	-12.8	-	standard
15a	Apr 06, 1995	2230-2350	T	3-	1.3	33 ±2	67.8	0.6	0.6 ± 0.2	reverse
15b	Apr 06, 1995	2230-2350	T	3-	1.9	42 ±4	67.4	0.7	-	reverse

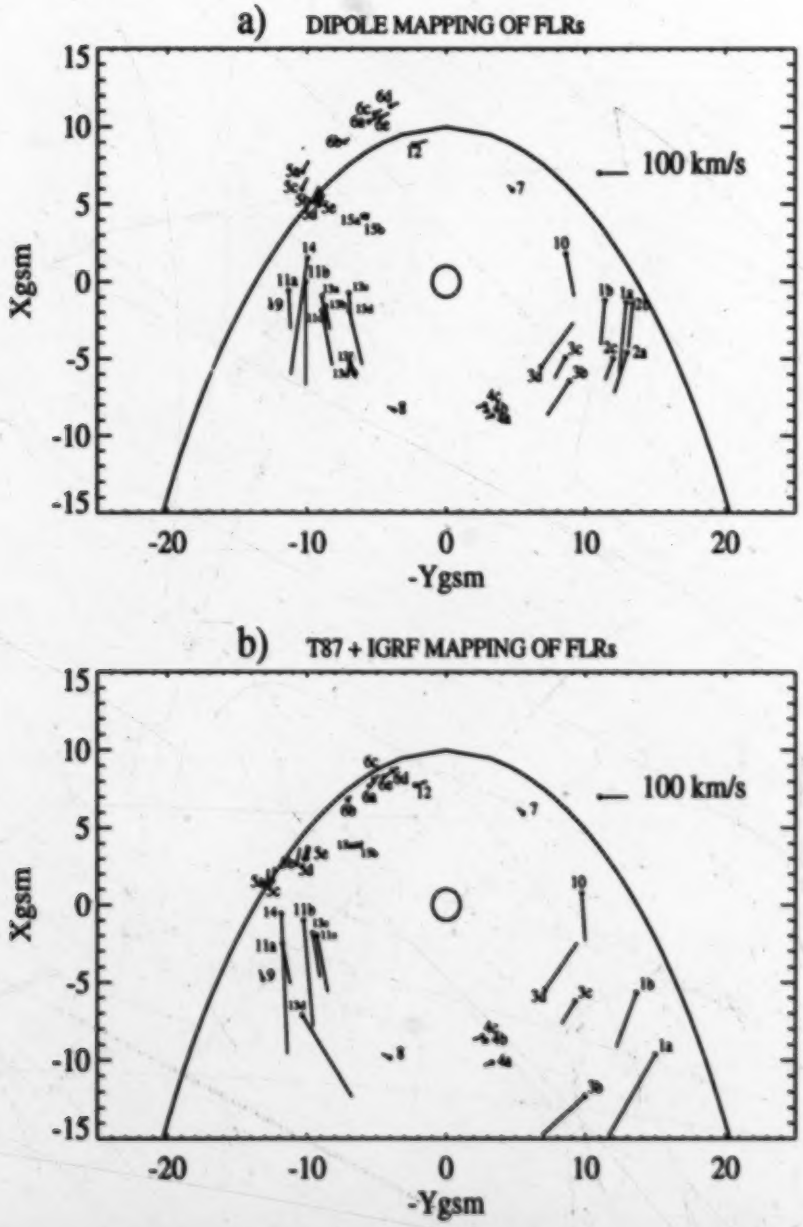

Figure 2.12. Mappings of the azimuthal phase velocities to the equatorial plane for each of the resonances listed in Table 2.1 for (a) a dipole model and (b) the Tsyganenko 87 [*Tsyganenko*, 1987] model with an International Geomagnetic Reference Field (IGRF). Note that event 2 and some of event 13 do not appear in Figure 2.12(b) because the T87 model mapped it to greater than 15 R_E down tail. The position of the magnetopause is taken from *Sibeck et al.*, [1991].

One of the most striking results was the reoccurrence of FLRs with the same discrete frequencies at various locations in the magnetosphere. The discrete and reproducible nature of the FLRs can be seen in the power spectra of Figure 2.5 and 2.6 and is reemphasized in Figure 2.13, which shows the number of occurrences for each frequency. In agreement with previous studies [*Ziesolleck and McDiarmid*, 1994; *Samson et al.*, 1992a, 1992b; *Walker et al.*, 1992; *Ruohoniemi et al.*, 1991], the most common FLR frequencies were 1.3, 1.9, and 2.5-2.6 mHz. There were also resonances observed at less common frequencies such as 0.8, 1.0, 1.5-1.6, 2.2, 2.8, 3.3, and 3.6 mHz. Given the spectral resolution the errors in the observed frequencies are ~±0.1 mHz. For resonances occurring at the same time during a given event, the lower-frequency resonances were localized at higher latitudes than the higher-frequency resonances as predicted by theory.

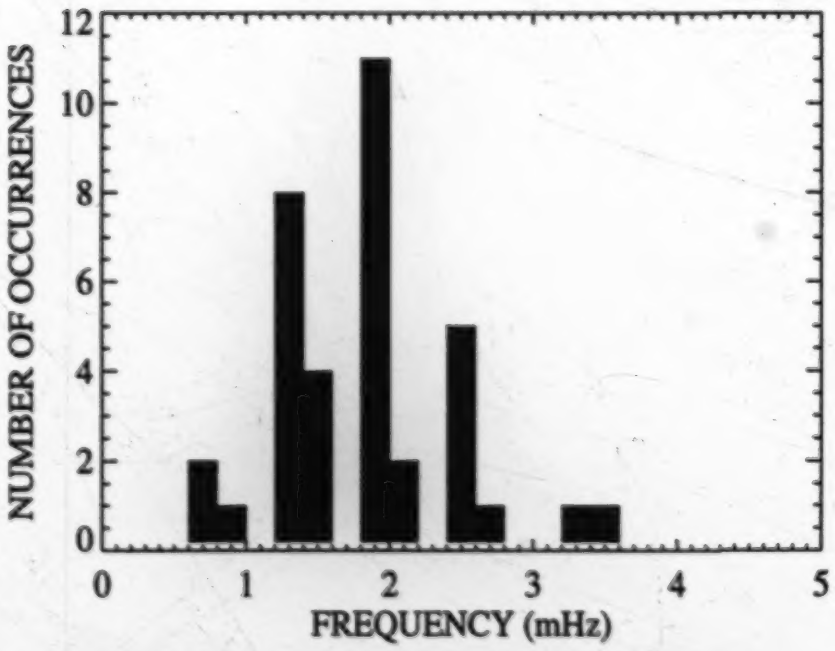

Figure 2.13. Number of occurrences observed to date for the various FLR frequencies. The frequency bins are 0.2 mHz in width centered at 0.1, 0.3, 0.5 mHz, etc. For example, the bin centered at 1.3 mHz covers the range $1.2 < f \leq 1.4$ mHz.

Two common features shared by all of the resonances were their stable frequencies and wave packet structure which were found to last for a duration of ~1 hour. These features are seen in Figure 2.14, which shows examples of the analytic signal representation and corresponding instantaneous frequency for two FLR events. The instantaneous frequency was calculated by taking the time derivative of the instantaneous phase of the analytic signal. Figure 2.14 also emphasizes the similar temporal variation of the resonance amplitudes for different frequency components in a given event, which is expected if the frequencies are harmonics of the fast compressional component in the cavity or waveguide.

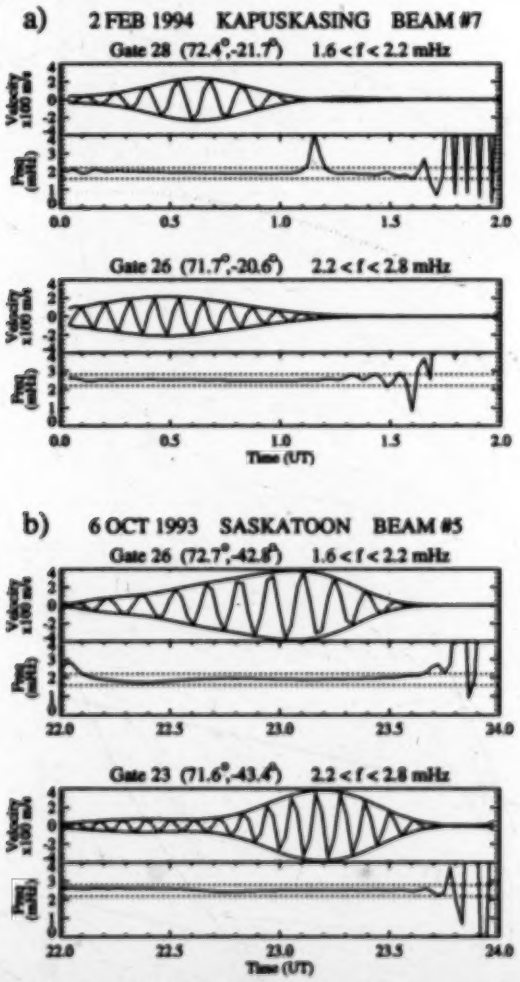
a) 2 FEB 1994 KAPUSKASING BEAM #7
Gate 28 (72.4°,-21.7°) 1.6 < f < 2.2 mHz
Gate 26 (71.7°,-20.6°) 2.2 < f < 2.8 mHz
Time (UT)
b) 6 OCT 1993 SASKATOON BEAM #5
Gate 26 (72.7°,-42.8°) 1.6 < f < 2.2 mHz
Gate 23 (71.6°,-43.4°) 2.2 < f < 2.8 mHz
Time (UT)

Figure 2.14. Analytic signal amplitude and frequency for the 1.9-mHz and 2.5-mHz resonances of two different events: (a) February 2, 1994 (low-*m*), and (b) October 6, 1993 (high-*m*). The dotted lines represent the bandwidth of the filter. Note the wave packet structure and the stable frequencies.

The m values ranged from 2-42 with distinct differences between resonances with low-m values (i.e., $m < 17$) and those with high-m values (i.e., $m > 17$). All of the observed high-m resonances exhibited a reverse phase change with increasing latitude, i.e., an increase in phase as the resonance was crossed, rather than the standard phase decrease of ~180 degrees which is predicted by FLR theory and characteristic of all the low-m resonances. The range-time plots of Figures 2.3 and 2.4, which correspond to a low- and high-m event, respectively, illustrate this difference in phase variation. The poleward moving bands in Figure 2.3 represent bands of constant phase. The motion of the bands poleward indicates that the lower latitudes lead the higher latitudes in phase, i.e. the standard decrease in phase with increasing latitude. Likewise, the equatorward moving bands in Figure 2.4 indicate the reverse or an increase in phase with increasing latitude. These phase variations are shown explicitly in Figure 2.7.

Another of the observable differences between the high- and low-m resonances was the polarization direction of the oscillating drift velocities. The high-m resonances were characterized by predominantly magnetic north-south velocity oscillations, while the low-m resonances displayed magnetic east-west velocities. The polarization directions of the velocity oscillations were first estimated by measuring the maximum amplitude of the line-of-sight velocities as a function of beam direction as done by *Ruohoniemi et al.* [1991]. This method assumed that the resonant pulsations were linearly polarized. Examples of such measurements for low- and high-m resonances are shown in Figures 2.15(a) and 2.15(b), respectively.

There were two events, the 18 October 1993 event and the 2 February 1994 event, where there was sufficient data on both the Kapuskasing and Saskatoon radars to allow determination of total velocity vectors rather than just the line-of-sight velocities. In order to confirm the velocity polarization characteristics, total velocity vectors corresponding to a given FLR during each of these events were determined. The resulting velocity polarizations at the location of the resonance maximum are shown in Figures 2.16(a) and 2.16(b) for a low-m and high-m FLR, respectively. It can be seen in these figures that the resonant pulsations are indeed linearly polarized at the resonance maximum. In the case of the high-m resonance the polarization direction is close to perpendicular to the line of the resonance contour. Since the resonance contour lies on a magnetic L shell the polarization direction for the high-m resonance is approximately magnetic north-south. In the low-m case the polarization direction is approximately along the resonance contour and therefore is approximately along magnetic east-west.

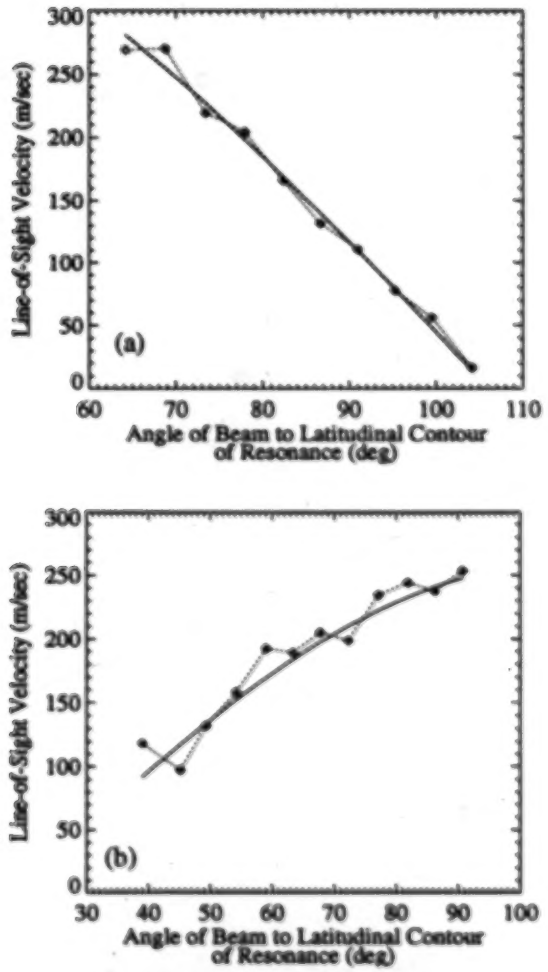

Figure 2.15. Plot of the line of sight velocity amplitude versus radar beam direction for (a) the 1.9-mHz component in the interval 0730-0900 UT on September 28, 1988, for beams 0-9 of the Goose Bay radar and (b) the 1.9-mHz component in the interval 1900-2100 UT on October 18, 1993, for beams 2-13 of the Saskatoon radar. The radar beam direction is given in terms of the angle of the beam to the latitudinal contour of the resonance peak power, taking counterclockwise (ccw) from geomagnetic east as positive. The solid lines represent in Figure 2.15(a) the theoretical curve for a velocity amplitude of 420 m/s directed along -16° ccw of the resonance contour and in Figure 2.15(b) the theoretical curve for a velocity of 260 m/s directed along -108° ccw of the resonance contour. Note that Figure 2.15(a) corresponds to a low-*m* resonance characterized by flows directed almost parallel to the resonance contour, while Figure 2.15(b) corresponds to a high-*m* resonance characterized by flows directed close to perpendicular to the resonance contour.

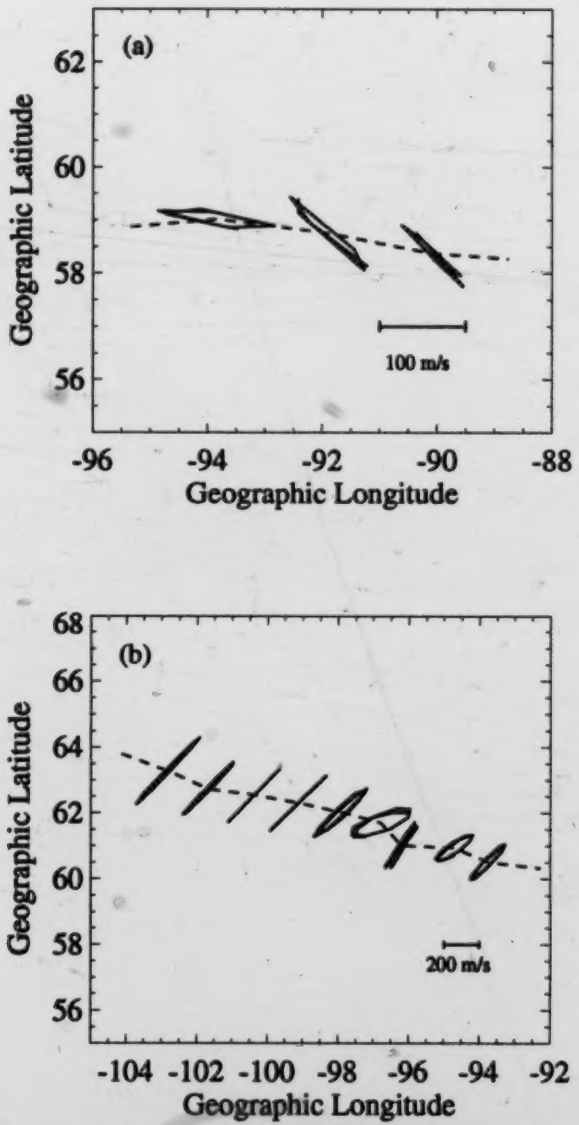

Figure 2.16. Plot of total velocity polarization ellipses at the resonance maximum for (a) the 2.6 mHz low-*m* FLR on 2 February, 1994; and (b) the 1.3 mHz high-*m* FLR on 18 October, 1993. The dashed line represents the resonance contour determined from the geographic coordinates of the range gate along each beam where the resonance was observed to be a maximum. The polarization ellipses were determined by tracing the tip of the total velocity vectors for one and a half periods during the time interval when the resonance was at its maximum amplitude.

A merge of the pulsation flow velocities in the vicinity of a low- and a high-*m* FLR are shown in Figures 2.17(a) and 2.17(b), respectively. Figure 2.17(a) corresponds to the 2.6 mHz low-*m* FLR of 2 February, 1994; while Figure 2.17(b) corresponds to the 1.3 mHz high-*m* FLR of 18 October, 1993. In these figures it is apparent that both the high- and low-*m* FLRs exhibit a vortex flow pattern, however, there is a significant difference in their respective flow patterns. The high-*m* FLR is characterized by a succession of small vortices along the east-west direction, while the low-*m* FLR is characterized by two larger vortices aligned along the north-south direction and which are elongated azimuthally. These observations confirm that the FLR plasma flows have the potential to wrap up into vortices as predicted by linear MHD simulations [*Ding et al.*, 1995].

Further differences between the high- and low-*m* resonances can be seen in the composite pictures of azimuthal phase velocities shown in Figures 2.12(a) and 2.12(b). The high-*m* resonances, those with small azimuthal phase velocities, were clustered on the dayside and around local midnight with all but one propagating westward. The low-*m* resonances, those with large phase velocities, were clustered near the dawn and dusk flanks and propagated predominantly anti-Sunward, i.e., eastward at dusk and westward at dawn. The group velocities were generally of the same order of magnitude for both the low- and high-*m* resonances ranging from 0.2 to 3.1 km/s in the ionosphere for the low-*m* resonances and 0.3 to 1.2 km/s for the high-*m* resonances. The resonance group velocity was always found to be smaller than the phase velocity and in most cases was in the same direction as the phase velocity. The group velocities are significant because they indicate the direction of azimuthal energy propagation, an important factor when considering where the source might be.

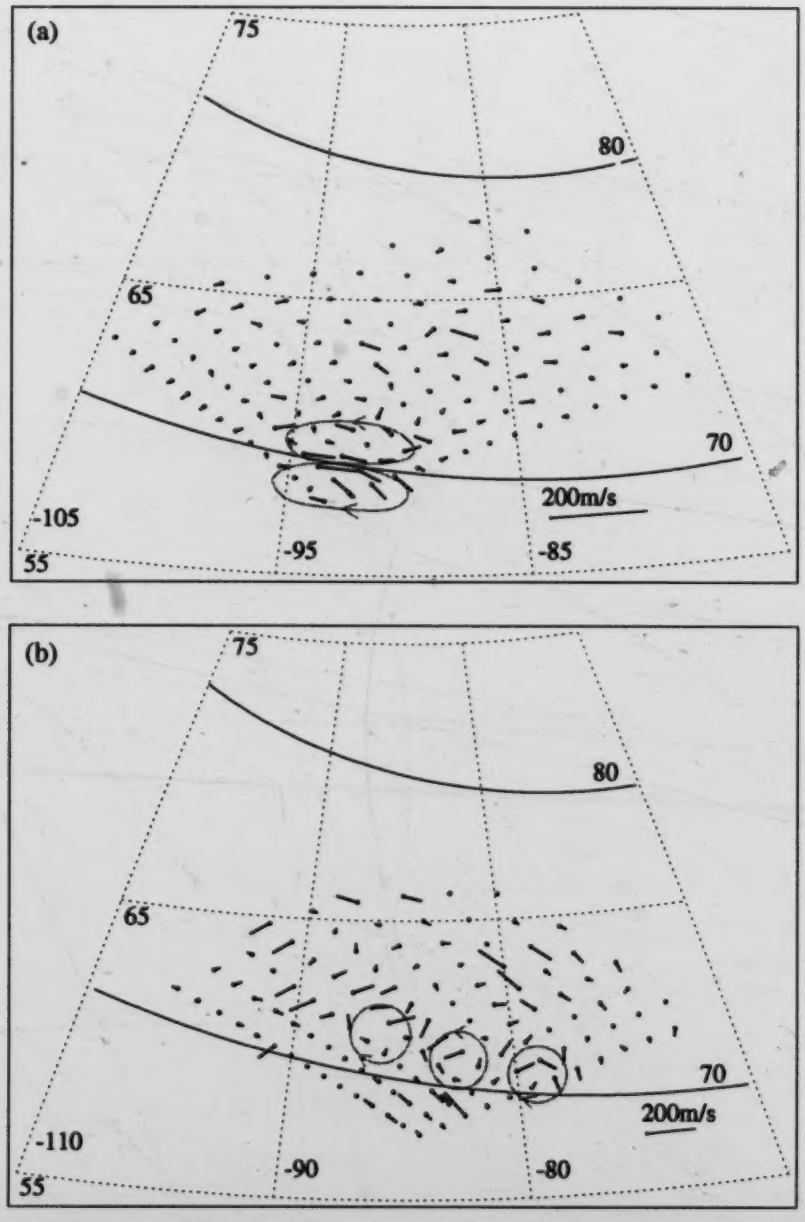

Figure 2.17. Merge of band-passed line-of-sight Doppler velocity data from the Saskatoon and Kapuskasing radars for (a) the time interval 1:23:20-1:25:0 on 2 Feb 1994 (2.4 mHz< f < 2.8 mHz) and (b) the time interval 21:08:20-21:10:01 on 18 Oct 1993 (1.1 mHz< f < 1.5 mHz). In each case the vortex flow pattern is sketched with a short dashed line. Note that (a) corresponds to a low-*m* FLR while (b) corresponds to a high-*m* FLR. The dashed lines are geographic coordinates and the solid lines are PACE geomagnetic coordinates.

2.3 Discussion

The first point that needs to be addressed is the occurrence of the high-*m* pulsations which exhibit some very interesting characteristics not typical of classic field line resonances. This brings up the following question: Are the high-*m* pulsations initiated by the same source as the low-*m* pulsations, or are they due to some other mechanism such as a wave-particle source? To help in answering this question, the observations of high-*m* pulsations presented in previous studies plus those of this paper will be discussed in terms of which source mechanisms they support.

ULF pulsations with large azimuthal wavenumbers have been detected in previous VHF radar studies *Allan et al.*, 1982; *Grant et al.*, 1992; *Walker et al.*, 1982; *Yeoman et al.* 1992]. A summary of the common observations presented in these studies only is as follows:

1. The majority of the high-*m* pulsations occurred in the noon-dusk quadrant.

2. The pulsations occurred at discrete frequencies with different frequencies dominant at different times. The most common frequencies found in these studies were 2.6 and 3.2-3.4 mHz.

3. Each pulsation had a latitudinal extent of approximately 3 degrees covering a large portion of the radar field of view. The pulsations did not appear to be localized within the field of view but would certainly be considered localized if they did not extend outside the field of view.

4. All pulsations exhibited westward phase propagation. In some cases the azimuthal phase velocity was mapped to the equatorial plane and was found to be consistent with gradient-curvature drifts of 35-70 keV protons in the ring current.

5. In most cases, an equatorward phase propagation consistent with an increase in phase with geomagnetic latitude was seen. *Yeoman et al.* [1992] provided evidence that such latitudinal phase increases could occur in regions like the plasmapause where the Alfvén velocity gradient is radially outward, not radially inward as it is in the region outside of the plasmapause. In the other studies the pulsations occurred at latitudes too high to involve the plasmapause, and in these cases the reverse phase variation remained unexplained.

6. All pulsations showed near-linear polarizations in the drift velocities with the polarization aligned close to the geomagnetic north-south direction. When mapped to the equatorial plane, they were radial in direction.

In the above studies a wave-particle source mechanism involving a drift-mirror instability was believed to be responsible for the observed pulsations. Cheng et al.

[1994] have examined drift mirror and drift Alfvén ballooning modes as possible explanations of Pc 5 waves.

The characteristics of the high-*m* resonances observed in this study agree in many ways with the characteristics of the previously observed high-*m* pulsations listed above. This suggests that they are all the same type of event. However, the high-*m* pulsations of this study were found to exhibit additional characteristics which may shed new light on the possible source mechanism. To begin with, the high-*m* resonances were found not only in the noon to dusk range of local times but also in the post-midnight and morning sectors. The high-*m* resonances of our study also showed numerous similarities to the resonances with small azimuthal wave numbers. They showed the same strong localization in latitude (see Figure 2.7) with an inverse relation between frequency and latitude (see Figure 2.5 and 2.6), as well as a very similar wave packet structure (see Figure 2.14). But most remarkably, they were found to exhibit the same discrete common frequencies as found for the low-*m* FLRs, i.e., 1.3, 1.5-1.6, 1.9, and 2.5-2.6 mHz. In fact, referring back to the previous studies of high-*m* pulsations, they too were found to occur at discrete frequencies with 2.6 and 3.2-3.4 mHz being the most common [*Allan et al.*, 1982; *Grant et al.*, 1992; *Walker et al.*, 1982]. These new observations provide strong evidence that the high- and low-*m* FLRs may be initiated by the same mechanism. In further support of this, one resonance event, that of October 6, 1993, included pulsations which showed a decrease in their azimuthal wave number from the high-*m* regime to the low-*m* regime. For example, the 1.3-mHz resonance of this event initially showed a large *m* value of ~17 and a reverse phase change with latitude. Then approximately 25 min later the azimuthal wave number had reduced to ~9, and the phase variation with latitude became the standard decrease of ~180 degrees.

If in fact the low- and high-*m* resonances do originate from the same source, then a source involving solely a wave-particle interaction must be ruled out since such a source could not produce pulsations with small azimuthal wave numbers propagating both eastward and westward. Currently, low-*m* field line resonances are believed to be coupled to fast wave eigenmodes generated by a waveguide or cavity in the magnetosphere; but can a magnetospheric waveguide or cavity model explain the high-*m* resonances as well? A detailed discussion of the magnetospheric waveguide modes as a potential source for both the high and low-m FLRs is presented in Chapter 4. There it is shown that the magnetospheric waveguide is an unlikely candidate for the source of the FLRs. It is also shown that the source is most likely external to the magnetosphere and a new theory involving the magnetosheath as a waveguide is developed.

Figure 2.18 is a schematic diagram illustrating the general locations and propagation directions of the high- and low-*m* resonances together with a proposed source location. The placement of the source on the flanks is supported by the location and propagation directions of the resonances. Propagating away from the source is a set of fast wave modes which have a continuum of azimuthal wave numbers. The fast waves with small k_y will couple to FLRs near the source, while the fast waves with larger values of k_y will propagate away, both up and down the waveguide, and will couple to FLRs further from the source. This scenario predicts the occurrence of eastward propagating high-m resonances in the pre-noon and pre-midnight sectors for which few examples have been observed. If the high-*m* resonances require amplification by a wave-particle interaction with the westward drifting ring current protons then this would explain the lack of high-*m* resonances propagating eastward.

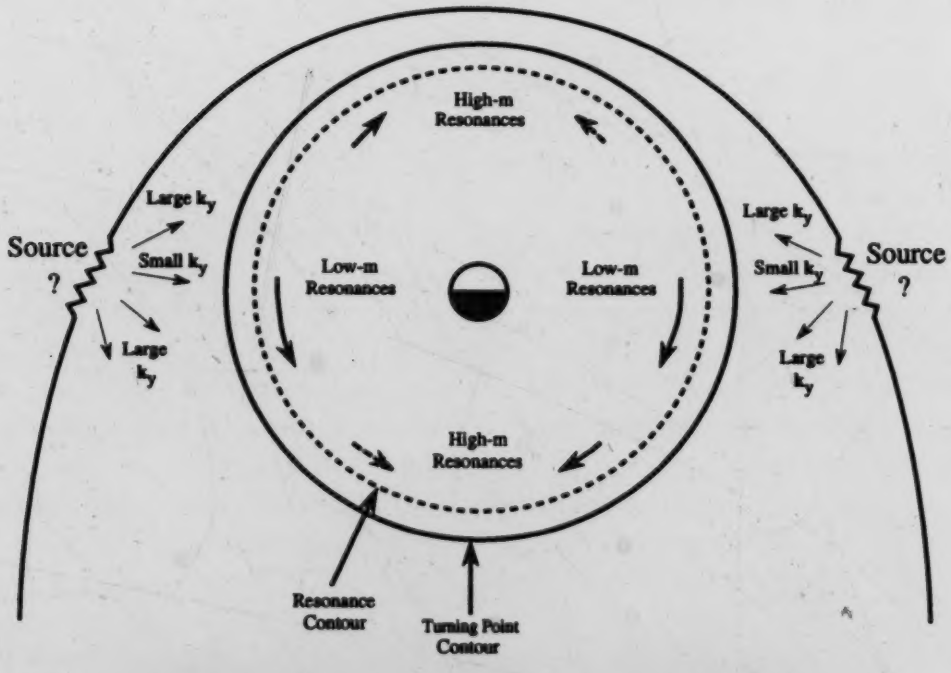

Figure 2.18. Schematic diagram of the equatorial magnetosphere illustrating the general locations and propagation directions of the observed high- and low-*m* resonances. The bold arrows represent observed propagation directions with the length of the arrows an indication of the relative magnitudes of the azimuthal phase velocities. The dashed arrows are only speculation due to limited data in the prenoon and premidnight sectors. Also shown are the proposed source locations.

Regardless of what the source of the high-*m* resonances is, the reverse phase associated with them is a very puzzling result. Statistical studies of both poleward (standard phase) and equatorward (reverse phase) moving events observed on VHF radars have been reported by *Waldock et al.* [1983] and *Tian et al.* [1991]. These studies have linked the equatorward moving events to events occurring in the region of the plasmapause and poleward events to events occurring outside of the plasmapause. However, they made no measurements of azimuthal wave number, and we are left to assume that their results include both low- and high-*m* pulsations. *Yeoman et al.* [1992], on the other hand, did measure the azimuthal wave number for 26 equatorward propagating events and found the *m* values to range from 10 to 30. Therefore these events were predominantly high-*m* events. As discussed earlier, Yeoman et al. explained the equatorward propagation of these events as being due to the occurrence of the pulsations in the plasmapause region, in accordance with the results of Waldock et al. and Tian et al. In addition, *Nielsen and Allan* [1983] reported a double low-*m* resonance observed simultaneously at plasmapause and plasma trough latitudes. The phase variation for this double resonance was of the reverse sense at the plasmapause latitude and of the standard sense at the plasma trough latitude.

Thus it can be concluded, from the aforementioned studies, that pulsations at plasmapause latitudes exhibit equatorward motion. This equatorward motion corresponds to an increase in phase with increasing latitude which is consistent with the outward gradient in the local shear Alfvén resonance frequency found at the plasmapause. In our study, however, all of the resonances are being observed at latitudes between 69° and 74° geomagnetic latitude where no radially outward gradient in the local shear Alfvén resonance frequency is expected. In fact, an inward gradient in the local shear Alfvén frequency is confirmed by the fact that all resonance events, both low- and high-*m*, exhibit an inverse relation between frequency and latitude (see Figure 2.5 and 2.6). Thus our observation of a reverse phase variation with latitude for the high-*m* resonances is not expected. Further discussion of the high-*m* reverse phase problem and a possible explanation can be found in Chapter 3.

A final point that warrants discussion is the observation of the less common field line resonance frequencies that do not fit into a simple magnetospheric waveguide model which predicts only a few frequencies like 1.3, 1.9, 2.6, and 3.3 mHz. The intermediate frequencies, such as 1.5-1.6 mHz, also seen by *Samson et al.* [1992a], were rarely found to exist independently of the more common frequencies indicating that there may be some link between them. *Ziesolleck and McDiarmid* [1994] suggest that they may be sidebands adjacent to the fundamental frequency peaks produced by the large-amplitude

modulation of the wave trains. The observation of resonances at lower frequencies, i.e., 0.8 and 1.0 mHz, also has important implications regarding the magnetospheric waveguide model since they indicate a waveguide of dimensions larger than that which can be generated by an outer boundary at the magnetopause and an inner boundary at the turning point.

2.4 Summary

The numerous field line resonances observed with the HF radars of the new SuperDARN system can be clearly classified into two distinct groups based upon the size of their azimuthal wave number, m. The high-m resonances (i.e., $m > 17$) exhibited the following characteristics.

1. They were localized in latitude with an increasing latitudinal phase shift.
2. They exhibited an inverse relation between frequency and latitude which is indicative of a radially inward gradient in the local shear Alfvén resonance frequency.
3. They showed a wave packet structure with a duration of ~1 hour.
4. All except one propagated westward.
5. They were clustered in the local afternoon and midnight sectors.
6. The pulsation velocities were linearly polarized predominantly in the magnetic north-south direction.
7. In one instance a vortex flow pattern aligned azimuthally was observed.

The low-m resonances (i.e., $m < 17$) were characterized by the following.

1. They were localized in latitude with a decreasing latitudinal phase shift.
2. They exhibited an inverse relation between frequency and latitude.
3. They showed a wave packet structure with a duration of ~1 hour.
4. Most propagated anti-Sunward (i.e., westward at dawn, eastward at dusk).
5. They were clustered near the dawn and dusk flanks.
6. The pulsation velocities were linearly polarized predominantly in the magnetic east-west direction.
7. In one instance an elongated vortex flow pattern aligned north-south was observed.

Although these two classes were distinguishable, resonances from both classes were found to occur at the same discrete frequencies, 1.3, 1.9 and 2.5-2.6 mHz, that have previously been associated with a magnetospheric waveguide. As well, some less common frequencies were found to reoccur such as 1.5-1.6 mHz.

The high-m resonances presented in this paper shared many common features with previous reports of high-m pulsations. These reports supported a wave-particle interaction as a source mechanism based upon the consistent westward propagation and the noon to midnight location of the high-m pulsations. However, our observations, which strongly link the low- and high-m resonances to the same source, make an exclusive wave-particle source unlikely and suggest that the wave-particle interactions may only play a role in amplifying the high-m waves already present. The role of wave-particle interactions is discussed further in Chapter 3. The locations and propagation directions of the high- and low-m resonances are consistent with a source of fast waves located at the flanks of the magnetosphere.

This observational study of FLRs has introduced some new and interesting questions. What is the nature of the source generating the discrete fast wave spectrum which couples to the FLRs. Why do the high-m resonances have a reverse phase change with latitude? How do the high-m modes couple as strongly as they do to the field line resonances? And finally, why do the same stable resonance frequencies occur repeatedly independent of local time and k_y? Finding answers to these questions is the purpose of the next two chapters.

3

Growth and Decay of Field Line Resonances[1]

Chapter 2 outlined a number of problems concerning the observed features of the FLRs. The most important of these problems is the lack of a consistent theory describing the complete mechanism responsible for generating the discrete FLR spectrum at both large and small m values. However, it is known that fast wave modes in the outer magnetosphere are driving the FLRs, so the main problem then is to determine the generation mechanism for the discrete spectrum of fast wave modes. There is another problem, though, in the fact that the high-m FLRs exist at amplitudes comparable to those of the low-m FLRs. As shown in Figure 1.7, the high-m coupling efficiency between the fast and shear Alfvén waves should be orders of magnitude smaller than that of low-m coupling [*Speziale and Catto*, 1977; *Kivelson and Southwood*, 1986]. Also, the high-m FLRs are characterized by an increase in phase with latitude rather than the expected decrease in phase which is characteristic of the low-m FLRs. Possible resolutions to the latter two problems are presented in this chapter. The stability of the FLR frequencies and the generating mechanism will be addressed in Chapter 4.

The basic premise of this chapter is that FLR growth rate, latitudinal phase shift, and azimuthal wave number are all interrelated. The goal is to sort out what that relationship is. The growth rates for the set of FLRs presented in Chapter 2 have been measured. The methods of growth rate measurement are detailed in Section 3.1. In Section 3.2 the results and a discussion of the factors relating the resonance m values, growth rates, and phase characteristics are presented. It is shown that an additional internal energy source is involved in the high-m mode coupling and is responsible for the distinguishing features associated with the high-m modes. It is suggested that a wave-particle interaction provides the internal energy source.

---

1. A version of this chapter has been submitted for publication. F. R. Fenrich, J. C. Samson, Growth and Decay of Field Line Resonances, J. Geophys. Res., submitted June, 1996.

3.1. Methods of Growth Rate Measurement

The data consists of the extensive set of FLR events presented in Chapter 2. In this chapter only the methods used to determine the growth rates will be discussed. For a detailed description of the general methods used to identify and characterize the FLRs see Chapter 2.

A field line resonance event evolves both temporally and spatially. A single beam of a radar observes both the temporal growth of the complete coupled system plus the spatial variation of the azimuthally localized resonance as it propagates through the field of view. The result is that each beam measures a time varying resonance amplitude with a characteristic wave packet structure which is determined by both the temporal and spatial variations of the resonance. In this paper it is only the temporal growth or decay of the complete FLR-fast wave system which is of interest. This type of growth or decay should be observable as a change in the maximum amplitude of the FLR wave packet as it propagates through the field of view of the radar. An example of the resonance wave packet structure and its propagation through the field of view of the radar is shown in Figure 3.1. Note that the azimuthal wave number, m, is determined by measuring the instantaneous phase of the wave as a function of longitude.

The HF radars provide line-of-sight Doppler velocity measurements corresponding to the convective plasma flows in the F-region of the ionosphere. The observed resonances are identified by oscillations in the measured background convective plasma flows. To measure the growth or decay of a particular resonance the Doppler velocity measurements were selected for all radar beams along which the resonance was observed. For each of these beams the velocity time series corresponding to the range gate where the power of the resonance was a maximum was selected for analysis. Recall that single radars provide only the line-of-sight Doppler velocities, i.e. only the component of velocity along the given radar beam. In order to get total velocities two radar measurements are required. However, since most of the identified resonances were observed only by single radars, due to the latitudinal location of the resonance and poor ionospheric scatter, the true pulsation velocity vectors were not directly measurable. Therefore a correction to the data had to be made to compensate for the angle of the beam to the pulsation flow direction.

In order to correct the line-of-sight velocities to get the total pulsation velocity a number of assumptions had to be made. First, it was assumed that the velocity fields at the resonance maximum were linearly polarized. Linear polarization at the resonance maximum has been shown in the coupling theory of *Southwood* [1974] and *Chen and*

Hasegawa [1974]. Second, the pulsation flow direction for the low-*m* resonances was assumed to be aligned along the resonance contour, i.e. approximately east-west, while the high-*m* resonances were assumed to have a pulsation flow direction aligned perpendicular to the resonance contour, i.e. approximately north-south. These assumptions concerning the pulsation flow directions are supported by the observations shown in Figure 2.16 as well as the theoretical result that the low-*m* resonances correspond to the toroidally dominated mode with azimuthal or east-west velocity fields, while the high-*m* resonances correspond to the poloidally dominated mode with radial or north-south velocity fields. Numerous VHF radar studies [*Walker et al.*, 1979; *Poulter*, 1982; *Grant et al.*, 1992; *Yeoman et al.*, 1992] have observed these pulsation flow directions. *Ruohoniemi et al.* [1991] used the variation in the line-of-sight velocity amplitudes with beam direction to estimate the pulsation flow directions and found the directions to be consistent with those mentioned above.

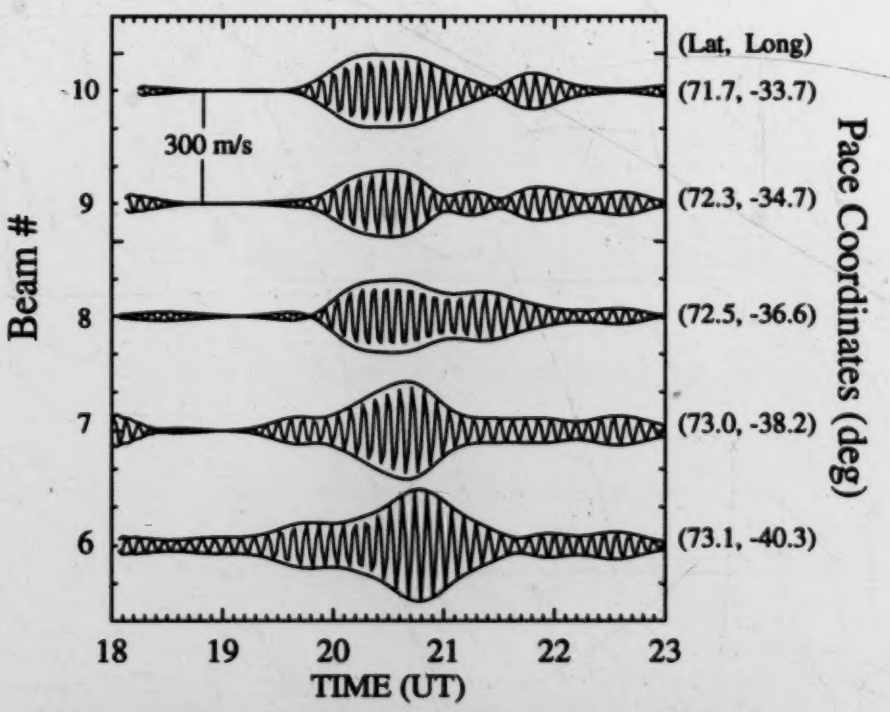

Figure 3.1. Stackplot of the band-passed (2.3 mHz < f < 2.7 mHz) uncorrected velocity time series data for beams 6 to 10 of the Saskatoon radar at the range gates where the 2.5 mHz resonance was at its maximum power on October 18, 1993. The envelopes of velocity were determined using an analytic signal analysis. The coordinates are PACE magnetic coordinates [Baker and Wing, 1989].

A plot of the location of the resonance as a function of latitude and longitude across the radar yielded the position of the resonance contour and therefore the pulsation flow direction, either parallel to the contour for a low-m resonance or perpendicular to the contour for a high-m resonance, from which the angle of the beam to the pulsation flow direction was determined. Specifying this angle by ϕ, the correction made to the line-of-sight Doppler velocities for that particular beam is given by

$$V_c = \frac{V_m}{\cos(\phi)} \tag{3.1}$$

where V_c is the corrected velocity and V_m is the measured line-of-sight Doppler velocity. An example of a measured resonance contour, estimated flow direction and beam direction is shown in Figure 3.2.

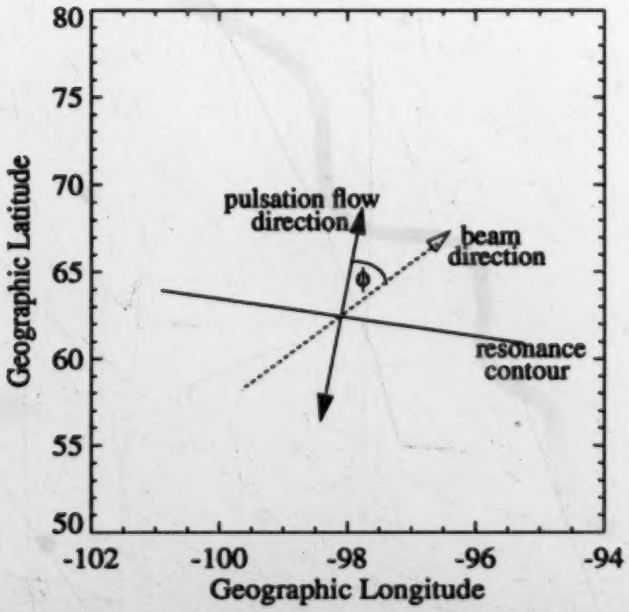

Figure 3.2. Plot of the resonance contour for a 2.5 mHz resonance observed on October 18, 1993. Because this was a high-m resonance the flow direction is estimated as being perpendicular to the resonance contour. The angle ϕ represents the angle between the pulsation flow direction and any given radar beam direction.

In order to isolate the resonance frequency of interest, the corrected velocity data for each beam was band-pass filtered with a bandwidth of 0.4 mHz centered on the resonance frequency. Note that the time resolution of the data is 100 seconds. For each beam, at the range gate where the resonance was a maximum, the power of the resonance wave packet was determined using the following method. A set of 32 point FFTs were taken at successive time points in the time series from well before the resonance to well after the resonance. Since a resonance wave packet typically lasted for approximately one hour, the set of FFTs covered a total time interval of approximately 2 hours. For each FFT the power spectrum was summed to give a total power value for that particular FFT time interval. The total power values for all FFTs were compared and the maximum found. The central time of the FFT window for which the total power was a maximum was chosen to represent the time corresponding to the resonance maximum along that particular beam. The Fourier analysis method was repeated for each selected beam yielding the total power of the resonance as a function of time. Note that the times chosen to correspond to the resonance maxima along the various beams were for the most part consistent with the propagation direction of the resonance. The plot of total power versus time was fit with an exponential curve whose time constant was used to determine the growth or decay rate of the resonance. Figure 3.3 shows examples of power versus time plots and their exponential fits for both a low-m and a high-m resonance. Figure 3.4 is a plot of the measured growth rates versus m value for all identified resonances. The plot also indicates the latitudinal phase shift of each resonance. Errors represent the standard deviation in the exponential fit. Points with greater than 50% error have been excluded as well as those points with m values between 10 and 25 since the assumptions concerning flow direction do not hold for intermediate m values.

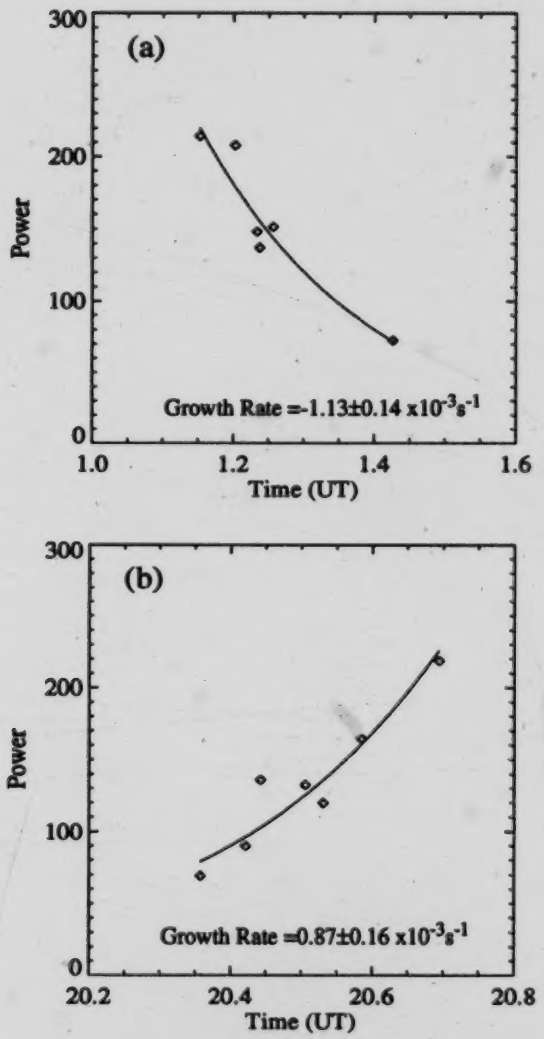

Figure 3.3. Plot of power vs. time and the exponential fits for **(a)** a 2.2 mHz low-*m* resonance observed on October 23, 1994 between 1 and 2 UT, and **(b)** a 2.5 mHz high-*m* resonance observed on October 18, 1993 between 20 and 21 UT.

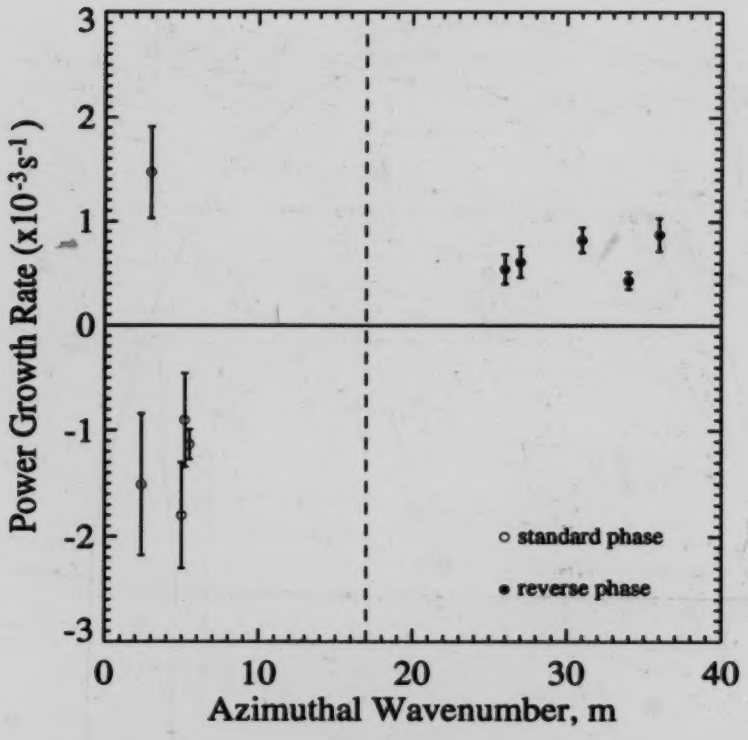

Figure 3.4. Plot of power growth rate versus azimuthal wave number. Standard phase refers to an observed decrease in phase with increasing latitude across the resonance while reverse phase refers to an increase in phase with latitude across the resonance. The dashed line represents the delineating value of *m* below which only low-*m* resonances with standard phase have been observed and above which only high-*m* resonances with reverse phase have been observed.

3.2. Results and Discussion

The plot of growth rate versus azimuthal wave number in Figure 3.4, shows that all of the high-*m* resonances exhibit growth while all, but one, of the low-*m* resonances exhibit decay. Also, all of the high-m resonances are characterized by a phase increase with latitude while all of the low-m resonances show a decrease in phase with latitude. These results indicate that there is indeed a relationship between the growth rate, latitudinal phase variation and azimuthal wave number. The consistent growth of the

high-m resonances is a very interesting observation. It suggests that in the case of the high-m resonances there is possibly some additional input of energy to the coupled system. The presence of an internal energy source, or lack thereof, may be the key to explaining the observed relationship between growth rate, latitudinal phase structure and m value. To investigate this possibility the ideal MHD theory governing the low-m resonance will be discussed. Then an internal driver will be added to simulate the high-m case

3.2.1. Low-m Case

In the general low-m case, the shear Alfvén field line resonance is driven by a monochromatic fast wave in the outer magnetosphere. The equations governing the coupling of the fast wave mode to the shear mode are well known and have been derived in the Chapter 1. Some of the derivations and equations will be repeated here for convenience. According to linear MHD coupling theory [*Southwood*, 1974; *Chen and Hasegawa*, 1974] the azimuthal component of the electric field, E_y, is given by

$$\frac{\partial^2 E_y}{\partial x^2} - \frac{k_y^2 \frac{\partial}{\partial x}\left[\frac{\omega^2}{V_A^2} - k_z^2\right]}{\left[\frac{\omega^2}{V_A^2} - k_z^2\right]\left[\frac{\omega^2}{V_A^2} - k_z^2 - k_y^2\right]} \frac{\partial E_y}{\partial x} + \left[\frac{\omega^2}{V_A^2} - k_z^2 - k_y^2\right] E_y = 0 \qquad (3.2)$$

where the z-direction is field aligned, the x-direction is radial, and the y-direction is azimuthal. The wave frequency is represented by ω, the Alfvén velocity by V_A, the field aligned wave vector by k_z, and the azimuthal wave vector by k_y. This equation has a singularity at the resonance position defined by

$$\frac{\omega^2}{V_A^2} - k_z^2 = 0 \qquad (3.3)$$

If there is no process by which energy can be dissipated at the resonance location, the standing shear Alfvén wave amplitude will grow to infinity. However, the ionosphere is not a perfect reflector to the shear Alfvén wave. Because the ionosphere has finite conductivity, the magnetic field perturbations above the ionosphere drive ionospheric

currents which dissipate energy through Joule heating. The dissipation of energy results in a finite field line resonance amplitude. Thus the Poynting flux at the ionosphere, which is given by

$$S = \mu_o \sigma_p E_1^2 \hat{z} \ , \tag{3.4}$$

is downward along the field lines. In equation (3.4) σ_p is the height integrated Pedersen conductivity and E_1 is an induced wave electric field in the ionosphere resulting from the oscillating wave magnetic field above the ionosphere. Note that the primary wave electric field has a node at the ionosphere.

Taking the wave perturbations to vary as $\exp[i(\omega t - k_y y - k_z z)]$, the ionospheric dissipation of energy may be represented in the coupling equations by letting the field aligned wave vector, k_z, have a positive imaginary part, i.e.

$$k_z = k_{zr} + i k_{zi} \tag{3.5}$$

where k_{zi} is proportional to the ionospheric conductivity. By defining

$$G(x) = \left[\frac{\omega^2}{V_A^2} - k_z^2 \right] \tag{3.6}$$

and using complex k_z with $|k_{zi}| << |k_{zr}|$, $G(x)$ may be expressed as

$$G(x) \cong \frac{\omega_r^2}{V_A^2} - k_z^2 - 2 i k_{zr} k_{zi} . \tag{3.7}$$

If $x=x_r$ is the value of x at the resonance where $\omega^2/V_A{}^2 = k_z{}^2$, then $G(x)$ may be expanded about $x=x_r$ to give

$$G(x) = G'(x_r)\,(x - x_r + i\varepsilon) \tag{3.8}$$

where $G'(x_r)$ represents the first derivative of $G(x)$ at x_r, and ε is defined by

$$\varepsilon = \frac{-2 k_{zr} k_{zi}}{G'(x_r)} \ . \tag{3.9}$$

Note that in the region of the magnetosphere where the FLRs have been observed, i.e. at latitudes of ~68°-74° at the ionosphere, there is generally a decrease in both V_A and k_z with increasing x which results in a corresponding decrease in the field line resonant frequency. This frequency gradient has been confirmed observationally by the fact that the lower frequency resonances are observed at higher latitudes. Thus $G'(x_r)$ is expected to be positive unless there is a reversal of the shear Alfvén frequency gradient. With both $G'(x_r)$ and k_{zi} being positive, ε will be negative. By substituting equation (3.8), equation (3.2) near the resonance, $x=x_r$, becomes

$$\frac{d^2E_y}{dx^2} + \frac{1}{(x-x_r+i\varepsilon)}\frac{dE_y}{dx} - k_y^2 E_y = 0 \tag{3.10}$$

which, for small k_y, has solutions of the form

$$E_y = -E_o ln\,[\pm k_y (x-x_r+i\varepsilon)]\ . \tag{3.11}$$

Note that there are two possible solutions. However, the correct solution is the one which will match the fast wave solution outside the resonance region. For the case of k_y positive the correct solution corresponds to the negative sign in equation (3.11).

For the case of small k_y the resonance is a toroidal wave with the wave electric field being primarily radial in direction. Therefore the sense of phase variation across the resonance is best illustrated by the phase changes in the radial component of the electric field, E_x. From the linear coupling theory E_x is related to E_y by the following equation.

$$E_x = \frac{-ik_y\dfrac{dE_y}{dx}}{\dfrac{\omega^2}{V_A^2} - k_z^2 - k_y^2} \tag{3.12}$$

Combining (3.11) and (3.12) yields the following expression for E_x near $x=x_r$.

$$E_x = \frac{-E_o\,[\varepsilon + i\,(x-x_r)\,]}{k_y\,[\,(x-x_r)^2+\varepsilon^2]} \tag{3.13}$$

The amplitude and phase of E_x according to equation (3.13) are shown in Figure 3.5. To

generate this figure ε=-0.3 Re and k_y=0.1 Re^{-1} have been used. The value of ε was chosen to yield a resonance width consistent with observations while the k_y value corresponds to m~1. The decrease in phase by ~180° as the resonance is crossed going from smaller x (lower latitudes) to larger x (higher latitudes) is consistent with all low-m observations.

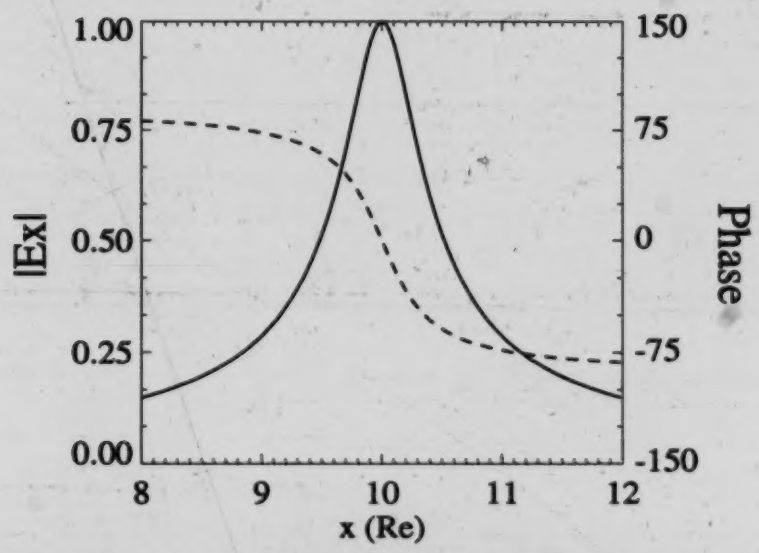

Figure 3.5. Plot of the amplitude (solid line) and phase (dashed line) of E_x near the resonance at $x=x_r=10\ R_E$ for the low-m case.

Thus the low-m scenario may be summarized as follows. A monochromatic fast wave mode in the outer magnetosphere couples to the shear Alfvén field line resonance. Because of the finite ionospheric conductivity, energy in the coupled system is dissipated into the ionosphere. During the initial time development of the coupling process the FLR will grow. At some point a marginal steady state will be reached where the Poynting flux into the FLR from the fast wave balances the Poynting flux into the ionosphere. This directionality of the Poynting flux results in the standard latitudinal phase decrease. If the energy of the fast wave mode is finite, the amplitude of the fast wave and the FLR will decrease together at a rate proportional to the rate of energy loss

into the ionosphere.

The scenario described above is in good agreement with the low-m observations. Although all of the low-m resonances exhibit the standard decrease in the latitudinal phase shift, which is consistent with the direction of the Poynting flux, not all low-m FLRs exhibit decay. The one instance where the low-m FLR grows most likely corresponds to the case where the coupled system is in its initial time development stage, whereas the remaining low-m FLRs correspond to the period of marginal stability.

For the purpose of illustration, consider the situation where the energy for the coupled shear-fast Alfvén wave system originates internally at the resonance location rather than an externally. In this case the Poynting flux would be in the opposite direction to that described above, i.e. it would point out into the fast wave from the FLR. This situation can be represented mathematically by taking ε as positive rather than negative. The relationship between the Poynting flux and ε can be seen in Figure 3.6(a) which illustrates the radial Poynting vector, S_x, for ε taken as negative, and Figure 3.6(b) which illustrates the radial Poynting vector for ε taken as positive. In Figure 3.6(a) the slope of Poynting flux versus radial position is negative in the resonance region indicating that energy is being absorbed there. The plot also shows that the Poynting flux direction is into the FLR from the fast wave, i.e. S_x is negative for $x>x_0$. In Figure 3.6(b) the slope of Poynting flux versus radial position is positive in the resonance region indicating that there is now an injection of energy at the resonance region. In this case, the Poynting flux direction is from the resonance out into the fast wave, i.e. S_x is positive for $x>x_0$. Thus a negative ε simulates an absorption of energy at the resonance with the Poynting flux directed from the fast wave into the FLR, while a positive ε simulates an injection of energy with Poynting flux directed from the FLR into the fast wave. Note also that the magnitude of ε determines the width of the resonance region and thus the region over which the energy is either being absorbed or injected.

It is the direction of the Poynting flux, represented by the sign of ε, which determines the sense of the latitudinal phase variation across the resonance. Recall that a decreasing latitudinal phase shift results when the Poynting flux direction is from the fast wave into the FLR and down into the ionosphere as was shown above in Figure 5 for the low-m case. Now consider the new case where the Poynting flux is in the opposite direction, i.e. from the FLR into the fast wave. Figure 3.7 depicts the low-m solution for this scenario showing the amplitude and phase of E_x with ε taken as positive. Here the latitudinal phase shift is increasing rather than decreasing which confirms the effect of the Poynting flux direction upon the latitudinal phase shift.

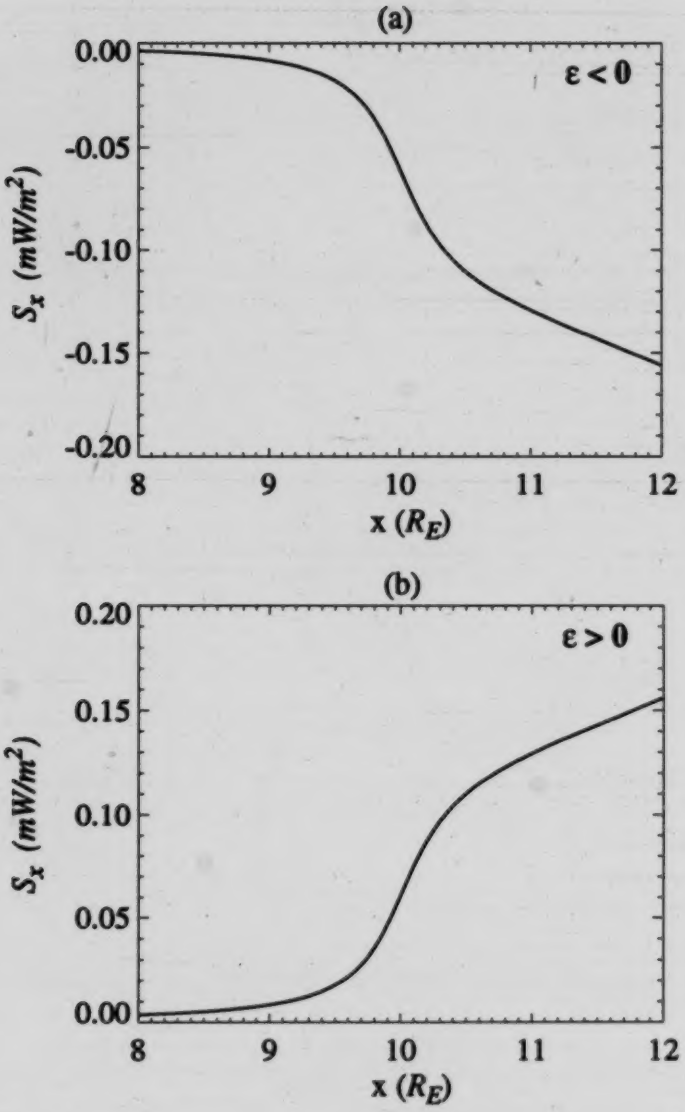

Figure 3.6. Plot of the time averaged radial component of the Poynting vector, S_x=Re{Ex$B^*/(2\mu_o)$}$_x$, versus radial position for (a) $\varepsilon < 0$ and (b)$\varepsilon > 0$. Note that the resonance position is at x=10 R_E.

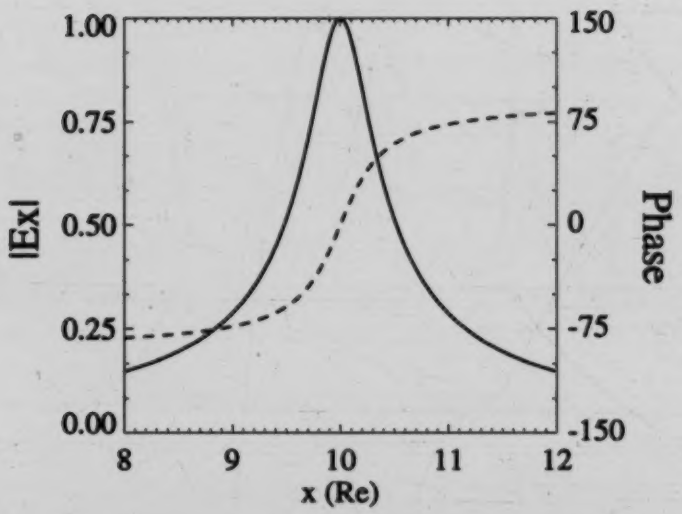

Figure 3.7. Plot of the amplitude (solid line) and phase (dashed line) of E_x near the resonance at $x=x_r=10\ R_E$ for the low-m case with ε taken as positive.

3.2.2. High-m case

Since the discrete frequency spectrum of the high-m FLRs is almost identical to that of the low-m FLRs, the fast wave driver must be responsible for initiating the high-m FLRs as well. However, there also must be an additional internal driver to the system which causes the temporal growth of the high-m modes and makes them observable. The presence of an internal driver causes the energy to flow from the internal driver into the FLR and out into the fast wave. When the system reaches a marginal steady state, the net Poynting flux into the FLR from the internal driver will approximately equal the Poynting flux from the FLR into the fast wave. If there is no energy dissipation mechanism in the fast wave region, the fast wave will grow in amplitude and thus so will the FLR. Since the internal driver is present only for the high-m modes, it most likely acts by pumping energy in through E_y which is the dominant electric field component for the high-m modes. To simulate the internal driver a real polarization current proportional to E_y is added, i.e.

$$J \rightarrow J + \frac{1}{V_A^2 \mu_o} \gamma E_y \hat{y} \ , \tag{3.14}$$

where γE_y is the positive real time derivative of E_y due to the influx of energy from the internal driver. Using a current density as defined by equation (3.14) and defining

$$\beta = \frac{\omega\gamma}{V_A^2 \frac{d}{dx}\left(\frac{\omega^2}{V_A^2}\right)} \tag{3.15}$$

results in an extra driving term added to the right hand side of equation (3.10), i.e.

$$\frac{d^2E_y}{dx^2} + \frac{1}{(x-x_r+i\varepsilon)}\frac{dE_y}{dx} - k_y^2 E_y = \frac{-i\beta E_y k_y^2}{(x-x_r+i\varepsilon)} \; . \tag{3.16}$$

Note that this driving term is not intended to represent the exact form of the internal driver, but is only intended to simulate the effect an internal energy source might have upon the solution. In equation (3.16) ε is positive to be consistent with an injection of energy from the internal driver into the resonance and the subsequent flow of energy from the FLR out into the fast wave.

Since the large k_y resonance is primarily poloidal, the phase variation across the resonance is best illustrated by the phase and amplitude of E_y. Using a fourth order Runge-Kutta algorithm numerical solutions to equation (3.16) have been determined. The resulting phase and amplitude of E_y are plotted in Figure 3.8. In generating this solution the following values were used: k_y=3.0 R_E, ε=0.3 Re, β=2.0 Re. The magnitude of ε was taken to be the same as that used in the low-*m* case in order to represent the fact that the magnitude of the Poynting vector, at marginal stability, is approximately the same in both the low- and high-*m* cases. The value for k_y was chosen to correspond to *m*~30, while the constant β, which determines the strength of the internal driver, was chosen to yield a strong resonance amplitude for E_y.

The solution shown in Figure 3.8 is very interesting because not only does the phase increase across the resonance, but it increases by several hundreds of degrees more than the 180° phase change typical of the low-*m* resonances. The strong phase change is in fact consistent with some of the high-*m* observations and is an indication that the solution is oscillatory in *x*. Figure 3.9 is a plot of the resonance power and phase for one observed high-*m* resonance showing a latitudinal phase increase of ~500° across the resonance. From the numerical solutions it was found that the magnitude of the phase change depended upon the size of β, i.e. the strength of the driver, as well as the size of k_y. Therefore in the case of the observed high-*m* resonances, differences in the

magnitude of the phase variation can be explained by differences in the strength of the internal driver as well as the size of the azimuthal wave number, k_y.

According to the above results, the growth and latitudinal phase increase of the high-m FLRs are consistent with the reversal of the Poynting flux which results from the presence of an internal driver. Since the FLR cannot grow indefinitely, it is expected that at some point the internal driver will turn off. In this case the Poynting flux direction will revert back to that of the low-m case and the fast wave and FLR should decay with the standard phase decrease. However, no decaying high-m FLRs have been observed. This may be due to the limited number of events studied or may indicate that once the internal driver turns off, the high-m resonance is no longer observable.

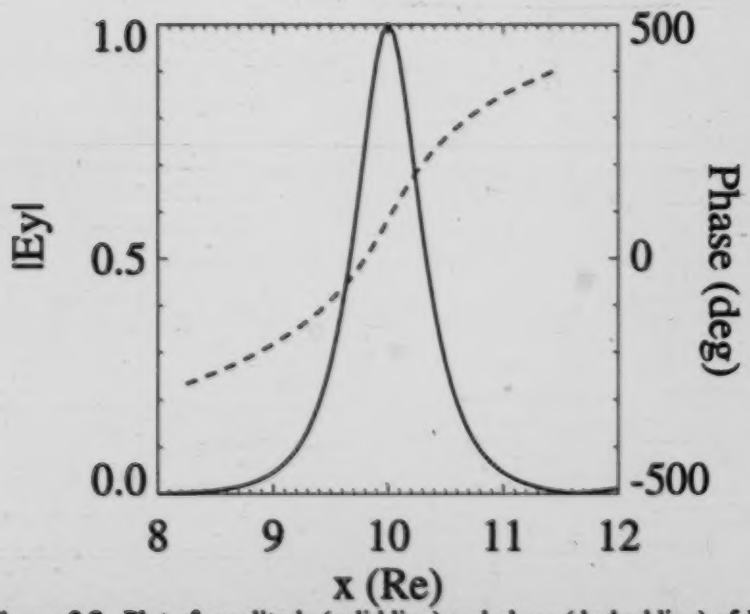

Figure 3.8. Plot of amplitude (solid line) and phase (dashed line) of E_y near the resonance at $x=x_r=10$ Re determined by the numerical solution to the driven system for large k_y.

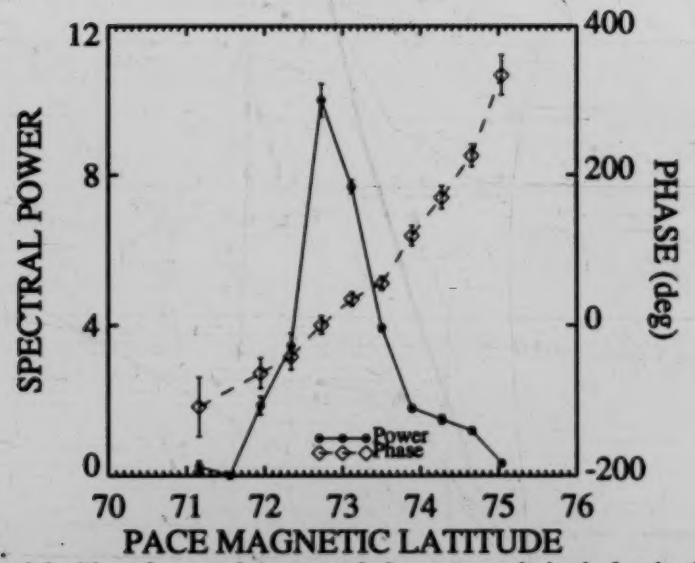

Figure 3.9. Plot of spectral power and phase versus latitude for the 1.3 mHz high-*m* resonance on 18 October, 1993. The data plotted is from beam 5 of Saskatoon for the interval 21:10-22:10 UT.

3.2.3. Wave-Particle Coupling

In this section the form of the internal driver which interacts with the high-*m* FLRs will be discussed. Many of the high-*m* characteristics suggest that a wave-particle coupling mechanism is acting as an internal driver to the system. *Walker et al.* [1982], *Allan et al.* [1982], *Yeoman et al.* [1992], and *Grant et al.* [1992] have all made observations of a class of high-*m* ULF pulsations termed "storm-time" Pc5 events which they have attributed to a wave particle interaction and in particular a drift-mirror instability in the ring current. These storm-time Pc5 pulsations were shown in Chapter 2 to share many characteristics with the discrete high-*m* FLRs of this study. The similar characteristics include local time of occurrence (noon-dusk), a large radial or north-south component in the pulsation, and westward phase propagation. In some of the storm-time Pc5 studies the westward phase velocities when mapped to the equatorial plane were found to be consistent with gradient-curvature drifts of ring-current protons. In the case of the high-*m* FLRs used in this study, the westward phase velocities when mapped to the equatorial plane ranged from 15-40 km/s. Subtracting a background convective ExB drift of ~10 km/s [*Allan et al.*, 1982] this range corresponds to gradient-curvature drifts of 10 to 30 KeV protons with 90° pitch angle at L~10 R_E. If the FLRs are fundamental

harmonic oscillations of the field lines then it is the 90° pitch angle protons near the equatorial plane which will couple most strongly to the FLRs since the protons interact through the pulsation electric field which has a maximum in the equatorial plane for the fundamental mode. However, if the FLRs are a second order harmonic then the energetic protons which can couple to the FLR must have a bounce motion as well as a drift motion and they must bounce and drift such that they always see the same phase of the wave. The energetic protons which can satisfy the drift-bounce resonance condition require larger energies on the order of 100 KeV. This energy value is consistent with the peak flux of the ring current. However, the ring current peaks at ~5-6 R_E during storm time periods, whereas the high-*m* FLRs are occurring at ~10 R_E during predominantly quiet times. Also, in geostationary satellite observations of ULF pulsations, 30 KeV particles were found to dominate the ion flux measurements [*Woch et al.*, 1990] while the strongest wave-particle resonance was found to involve 90° pitch angle protons [*Kremser et al.*, 1981]. These observation suggest that the ULF pulsations are fundamentals along the field line, and the more energetic drifting-bouncing protons are not required. Regardless of the proton energies involved, the high-*m* FLRs are definitely associated with some form of wave-particle interaction.

Various theories on wave-particle coupling and instabilities have been developed and used to try and explain such observations as the storm-time Pc5 events. *Hasegawa* [1969] initially developed the theory of the drift-mirror instability which involves the generation of waves due to the drift-bounce motion of particles. Later, other authors showed that the unstable drift-mirror wave could couple to shear Alfvén wave modes [*Lin and Parks*, 1978; *Walker et al.*, 1982]. Kinetic theories on the excitation of Alfvén waves purely through resonant particle instabilities have been looked at in general by *Southwood* [1976] and including finite Larmour radius effects by *Chen and Hasegawa* [1988]. More recently, *Walker* [1994] evaluated the effects of an energetic particle population on a pre-existing standing hydromagnetic wave and showed the existence of a drift resonance while maintaining marginal stability.

All of the theoretical treatments listed above, except for *Walker* [1994], attribute the excitation of the high-*m* pulsations solely to a particle driven instability in the ring current. However, this excitation mechanism cannot explain the recent observations of *Fenrich et al.* [1995] which show the existence of the high-*m* FLRs at the same discrete frequencies as the low-*m* FLRs. These observations suggest that the same initial excitation mechanism is responsible for both the low- and high-*m* FLRs. The low-*m* FLRs cannot be associated with an energetic particle instability due to their large azimuthal wavelengths and propagation directions. This leads us to conclude that a

wave-particle interaction is not the sole mechanism responsible for initiating the high-*m* FLRs. Instead, both the high- and low-*m* resonances are initiated by the same mechanism which determines the normal mode structure. Generally, this mechanism is believed to involve the resonant coupling between MHD fast compressional modes and standing shear Alfvén waves on field lines whose natural frequency corresponds to the frequency of the fast wave [*Tamao*, 1966; *Southwood*, 1974; *Chen and Hasegawa*, 1974]. The fast wave modes are possibly eigenmodes of a magnetospheric waveguide [*Samson* et al.,1992b; *Wright*, 1994], to be discussed in Chapter 4, thus explaining the discrete nature of the FLRs.

The coupling efficiency between the fast wave mode and the FLR is dependent upon the azimuthal wave number [*Speziale and Catto*, 1977; *Kivelson and Southwood*, 1986]. Coupling is non-existent for m=0, maximum for small m values and then decreases as m increases. Thus the high-*m* FLRs are not expected to be observable and yet they are seen at amplitudes comparable to the low-*m* FLRs. This is where the wave-particle interaction comes into play. Those modes with large azimuthal wave numbers propagating westward in the same direction as the ring current, and with phase speeds equal to the gradient-curvature drift speeds of energetic ring current protons, begin to grow. The growth arises from a transfer of energy from the energetic particle population to the wave as the particles drift along always seeing the same phase of the wave. Of course for energy to be transferred into the wave the velocity distribution of the energetic particles must be such that there are more particles moving slightly faster than there are particles moving slightly slower than the phase speed of the wave. This type of interaction is described as a drift resonance by *Walker* [1994]. However, rather than there being a perfectly stable balance, as Walker describes, between energy influx from the resonant particles and energy losses in the ionosphere, the particle resonance dominates yielding a net flux of energy into the FLR and fast wave which causes growth of both the fast wave and FLR. This scenario is supported by the observation of high-*m* growth shown in Figure 3.4.

An extensive set of geostationary satellite observations of ULF waves in the ring current by *Woch et al.* [1990] provides evidence that some ULF pulsations are coupled to energetic ring-current particles. *Woch et al.* observed numerous events characterized by simultaneous modulations of the particle fluxes and oscillations of the magnetic field. The events were classified as diamagnetic if their onset was immediately preceded by an enhancement of the ion intensity and as non-diamagnetic events if not. In the 1-4 mHz range the events were primarily non-diamagnetic. The non-diamagnetic events were found to exist during periods of low, decreasing geomagnetic disturbance levels but with

enhanced ring current. Values of the D_{st} index during the time periods when the high-*m* FLRs of this study were observed ranged from -15 to +4 indicating that the resonances occurred during quiet magnetospheric conditions with little or no enhancement of the ring current. Note the D_{st} index provides information on the world-wide magnetic storm with larger negative values indicating a more intense storm. Thus it is highly unlikely that there is a particle driven instability involved independent of the FLRs.

3.3. Summary

The measurements of FLR growth rates versus azimuthal wave number has yielded a very interesting result. The low-*m* FLRs, characterized by the standard decrease in phase with latitude, were found in almost all cases to exhibit temporal decay. The high-*m* FLRs, characterized by a phase increase with latitude, were found in all cases to exhibit temporal growth. The temporal growth indicates the presence of an internal energy source in the high-*m* case.

The FLR growth rates and latitudinal phase shifts were found to be consistent with the direction of the Poynting flux through the system. In the low-m case, energy flows from the fast wave driver into the FLR and then into the resistive ionosphere. An analytic solution to the linearized ideal MHD equations showed that this Poynting flux direction always results in a latitudinal phase decrease of ~180^{o}. In marginal steady state this Poynting flux direction will also cause a temporal decay of the FLR and fast wave amplitudes. However, in the initial time development before a steady state is reached the FLR will grow in amplitude as the fast wave driver begins to couple to the FLR.

In the high-*m* case an internal driver couples to the FLR and reverses the direction of the Poynting flux such that the energy now flows from the internal driver into the FLR and out into the fast wave. The result is always an increasing latitudinal phase shift and a temporal growth of both the FLR and fast wave amplitudes. In order to simulate an internal driver for the high-*m* resonances a driving term was added to the ideal MHD equation governing the azimuthal component of the electric field, Ey, near the resonance. The resulting numerical solutions to this high-*m* equation showed a latitudinal phase increase of many hundreds of degrees. Such a large increase in phase with latitude is consistent with observations of high-*m* latitudinal phase variations. This result further supports the idea that the high-*m* FLRs are being driven by an internal energy source.

A wave-particle interaction, in the form of a drift resonance between energetic ring-current protons and the shear Alfvén FLR, is the most likely candidate for the internal driver. Note, however, that the wave-particle coupling mechanism is not the primary mechanism responsible for exciting the initial high-*m* FLRs, but is a secondary mechanism responsible only for the growth of the pre-existing high-*m* modes.

4

Discussion of Theoretical Models

This chapter is an investigation of various models which may have the potential to explain the observations of the discrete reproducible field line resonances discussed in Chapter 2. The currently accepted model, the magnetospheric waveguide/cavity model, has many deficiencies which are outlined in the following section. Given these deficiencies it is clear that a new model is required. After examining a few alternate possibilities a model involving the magnetosheath as a waveguide is developed, and will be shown to have the ability to explain many aspects of the FLR phenomenon.

4.1 Problems with the Magnetospheric Waveguide/Cavity Model

4.1.1 Plasma Density Problem

The success of the magnetospheric waveguide/cavity model lies in its ability to explain the discrete frequencies of the observed FLRs. As discussed in Section 1.2.5 these frequencies are predicted by solving the phase integral equation

$$\int_{x_i}^{x_m} \left(\frac{\omega^2}{V_A^2} - k_z^2 - k_y^2 \right) dx = \left(n - \frac{1}{4} \right) \pi, \tag{4.1}$$

In order to solve equation (4.1) the magnetopause position, x_{mp}, and the Alfvén velocity profile, $V_A(x)$, must be estimated. Based upon a minimization technique Samson et al. [1992b] found

$$V_A(x) = V_{pp} \left(\frac{x_{pp}}{x} \right)^3$$
$$x_{mp} = 14.8 R_E \tag{4.2}$$

where V_{pp}=1000 km/s is the Alfvén velocity at the plasmapause location defined by x_{pp}=5 R_E, and found the waveguide eigenfrequencies to be 1.24, 1.91, 2.75, and 3.62 mHz. In determining these frequencies Samson et al. assumed $k_y^2 << k_z^2$ and used the resonance relation of equation (1.58) to determine k_z. However, assuming a dipole

magnetic field which is of the form

$$B_{dipole} = B_{pp}\left(\frac{x_{pp}}{x}\right)^3 \qquad B_{pp} = 250nT \qquad x_{pp} = 5R_E \ , \tag{4.3}$$

the Alfvén velocity profile in (4.2) corresponds to a constant plasma density of ~30 m_p cm^{-3}, where m_p represents the proton mass. Such a large plasma density is very unrealistic according to observations [Parks, 1991; Kivelson et al., 1984]. A reasonable plasma density profile consistent with observations is given by

$$\rho(x) = \rho_{pp}\left(\frac{x_{pp}}{x}\right)^4 \qquad \rho_{pp} = 15m_p(cm)^{-3} \tag{4.4}$$

which yields plasma mass densities on the order of 1 m_p cm^{-3} in the regions of the magnetosphere where the FLRs are generated.

Solving equation (4.1) for the waveguide eigenfrequencies using the plasma density profile defined in (4.4), the dipole field of (4.3), x_{mp}=15 R_E, k_y=0.1 R_E^{-1}, and k_z=0.1R_E^{-1} yields a fundamental frequency of ~5 mHz which is substantially larger than the lowest observed resonant frequency of 0.8 mHz. Note that the k_y value used corresponds to that of maximum coupling to the FLR and the k_z value is typical of dipole-like field lines at ~10 R_E. Thus unless there is an enhanced plasma density in the outer magnetosphere which has not yet been detected, the magnetospheric waveguide is not able to generate the observed resonance frequencies. Even if such large densities did exist, according to the resonance condition $\omega = V_A k_z$, the k_z values would have to be much larger than that which corresponds to dipole field line lengths in order to get the observed frequencies at the observed locations.

4.1.2 The Problem Concerning Large Azimuthal Wave Numbers

The observations of the large k_y field line resonances presents a major problem for the waveguide/cavity model. FLRs have been observed with m values as large as 40 which corresponds to k_y values as large as ~4. However, the variation of frequency with k_y in the magnetospheric waveguide is quite significant. It has been calculated using equations (4.1) and (4.2) and can be seen in Figure 4.1. This figure shows that a change in k_y from 0 to 1.0 corresponds to a 200% change in the eigenfrequency of the waveguide. Thus a waveguide inside the magnetosphere likely does not generate the observed high- and low-m FLRs which occur at the same set of reproducible frequencies.

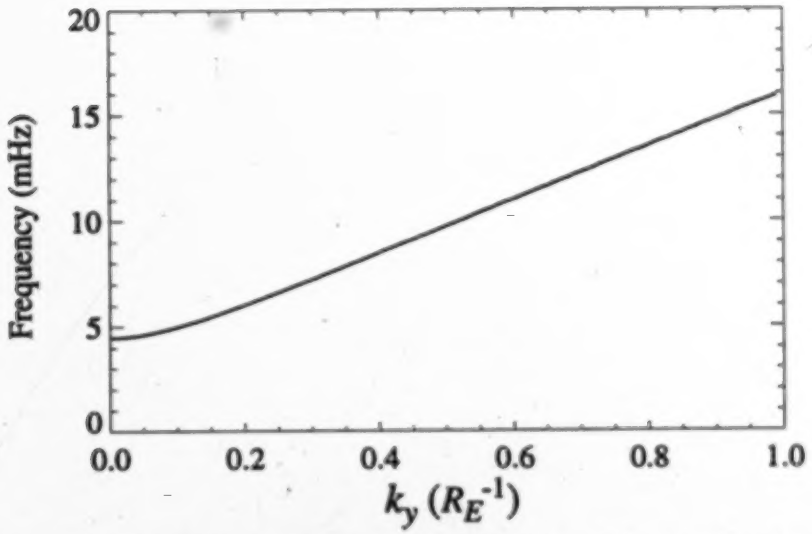

Figure 4.1. Magnetospheric waveguide frequency variation as a function of k_y for x_m=15 R_E and k_z=0.1 R_E^{-1}.

Another way of looking at the large k_y problem is to consider the locations of the turning points. Using the turning point condition

$$\frac{\omega^2}{V_A^2} - k_z^2 - k_y^2 = 0 \tag{4.5}$$

together with the observed FLR frequencies and locations, the turning points as a function of k_y can be determined. Table 4.1 lists the frequency, L value, k_z, and k_y for three of the low-m resonances observed during the January 11, 1989 event. Note that the k_z values were determined from the resonance condition, $\omega = V_A k_z$, where the Alfvén velocity profile used corresponds to the dipole field and the plasma density profile defined in (4.4). Using the parameters of Table 4.1, the turning points as a function of k_y have been determined and plotted in Figure 4.2. In this plot the FLR turning points corresponding to the observed k_y values listed in Table 4.1 are indicated with a cross, and are well beyond the location of the magnetopause. Given that the range of k_y values for all observed FLRs is 0.3 to 4.0, the observed FLRs most likely have their turning points outside of the magnetosphere and therefore cannot be associated with a magnetospheric waveguide.

Table 4.1: Parameters For Three Low-m FLRs

f (mHz)	L (R_E)	k_z (R_E^{-1})	k_y (R_E^{-1})
1.3	11	0.08	0.45
1.9	9.9	0.11	1.0
2.6	8.7	0.13	0.57

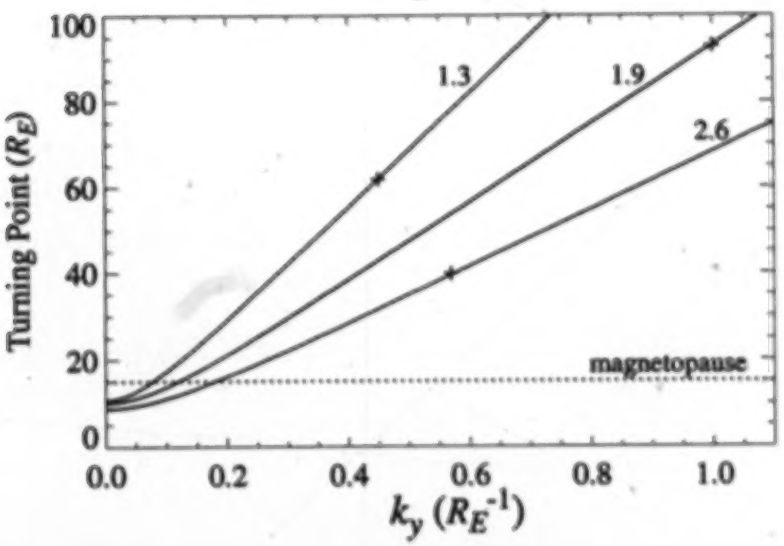

Figure 4.2. Plot of turning point as a function of k_y for 1.3, 1.9, and 2.6 mHz FLRs. The crosses represent the turning point locations corresponding to the measured k_y values.

An additional problem concerning the large k_y FLRs is that according to Wright [1994], only small k_y eigenmodes can grow strong enough in the waveguide to couple to the FLRs. This can be understood in the following way. The small k_y modes remain in approximately the same azimuthal location and therefore are able to constructively add to themselves while the large k_y modes propagate away with no constructive growth.

4.1.3 Stability Problem

In Chapter 2 the observed FLR frequencies were shown to be very stable and reproducible. However, the magnetosphere is a very dynamic system and thus a magnetospheric waveguide may not be able to generate a stable and reproducible set of eigenfrequencies during different magnetospheric conditions. To investigate the stability of the magnetospheric waveguide, the frequency of the guide as a function of magnetopause position and different Alfvén velocity profiles has been determined. The Alfvén velocity profiles used are of the form

$$V_A(x) = V_p\left(\frac{x_p}{x}\right) \tag{4.6}$$

which corresponds to a dipole magnetic field and a density profile as given in equation (4.4). Taking x_p=5 R_E as the location of the plasmapause, V_p is determined by the magnetic field strength and plasma density at the plasmapause. Taking these values to be 250 nT and 15 $m_p\ cm^{-3}$, respectively, gives V_p=1400 km/s. To represent changes in magnetospheric conditions this value of V_p is varied. A value of V_p=1200 km/s is used to represent a 15% decrease and a value of V_p=1600 km/s is used to represent a 15% increase in the Alfvén velocity throughout the guide giving an overall variation of 30%. The results are plotted in Figure 4.3 which shows the waveguide eigenfrequency as a function of magnetopause position for the three different Alfvén velocity profiles. From this figure it is apparent that changes in magnetopause position of ~1 RE corresponds to changes in the waveguide eigenfrequency of ~15%. A Similar change in eigenfrequency results from a 15% change in the Alfvén velocity. Given that the measured FLR frequencies can vary by approximately 10%, small variations in magnetospheric conditions may not have a significant effect. However, the observed FLRs are generally spatially localized within the field of view of the radar and therefore the fast wave eigenmode driving the FLR must also be localized to a specific region of the magnetosphere with its eigenfrequency determined by the dimensions of that region. Considering the difference in magnetopause position as a function of local time from dawn to dusk, i.e. ~15 R_E at dawn and dusk and ~10 R_E at noon, the variations in eigenfrequency can be as large as ~100%. The observation of the same discrete frequencies at different local times is then inconsistent with the waveguide scenario.

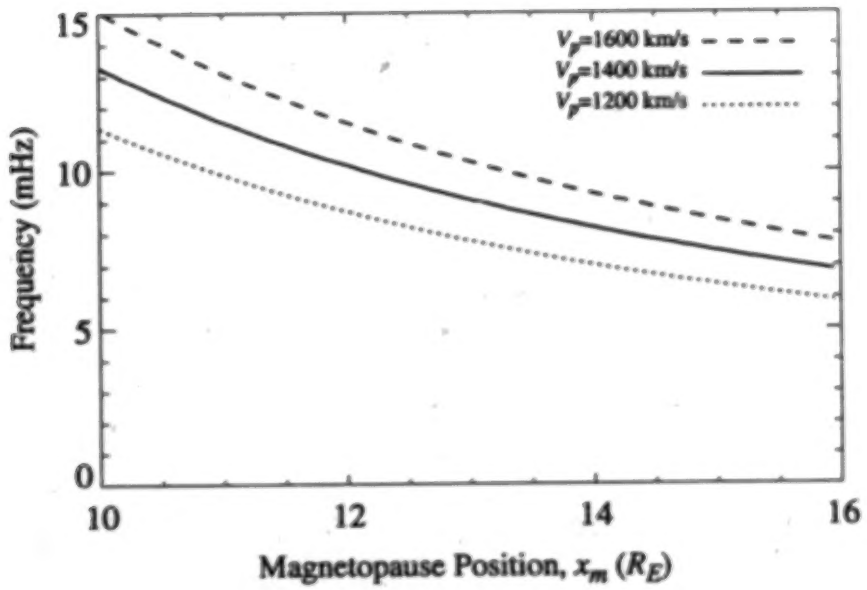

Figure 4.3. Magnetospheric waveguide eigenfrequency as a function of magnetopause position for three different Alfvén velocity profiles. Note that for this plot k_y=0.3 R_E^{-1} was used to keep the turning point beyond the plasmapause, while the k_z value used was 0.1 R_E^{-1}.

4.2 Other Possible Models

Given the problems concerning the magnetospheric waveguide model defined above, it can be concluded that this model is probably not the solution to the field line resonance problem. Therefore we need to look at other possible models which can better explain the FLR observations. One model which has been considered is the existence of an MHD cavity in the magnetotail [Siscoe, 1969; Sebolt, 1990; Liu et al., 1995]. This model is attractive because under typical magnetospheric conditions frequencies in the 1-5 mHz range can be achieved. However to get a discrete set of frequencies, boundaries in all three dimensions are required. In a GSM coordinate system, boundaries in the y-direction would be provided by the magnetopause; in the z-direction either turning points within the plasma sheet boundary layers or the magnetopause can provide the reflecting boundaries; while in the radial direction it is not clear what boundaries might exist. In any case the magnetotail dimensions are

highly variable depending on magnetic conditions and thus a tail mode model has serious stability problems. An additional point which rules out the magnetotail as a possible source for the discrete FLRs is the fact that a source in the tail cannot produce any of the anti-sunward propagating FLRs since compressional wave energy coming from the tail could only generate sunward propagating FLRs.

Another mechanism which may play a role in the generation of FLRs involves the reconnection of field lines on the dayside of the magnetosphere. There have been some observations that dayside magnetic reconnection can be modulated at frequencies similar to FLR frequencies [Prikryl et al., 1996] However, there is no known mechanism by which the reconnection process could generate the set of discrete frequencies observed for the FLRs. The fact that the observed FLRs occurred primarily during quiet magnetic conditions with probably little dayside reconnection provides conclusive evidence that a mechanism associated with dayside reconnection cannot be responsible for generating the FLRs. Thus pulsed reconnection may be a result rather than a cause of the FLR phenomenon.

The most promising model concerning the source of the FLRs involves the magnetosheath. The involvement of the magnetosheath was first suggested by Harrold and Samson [1992], who proposed the existence of a waveguide between the bow shock and a turning point deep within the magnetosphere. The larger dimensions of this waveguide compared to that of the magnetospheric waveguide allowed for eigenfrequencies in the 1-5 mHz range without requiring unreasonably large magnetospheric plasma densities. However, like the magnetospheric waveguide model, this model is subject to the same dispersion and stability problems. It is also highly unlikely that waveguide modes would be generated between the bow shock and a turning point within the magnetosphere for the following reasons. The magnetopause is a good reflector of fast waves, as will be shown in the next section, and therefore waves impinging on the magnetopause from either the magnetosheath or the magnetosphere will be strongly reflected. Also the bulk plasma flows in the magnetosheath and magnetosphere are in opposite directions. With plasma flow in opposite directions it would be difficult for an eigenmode spanning both regions to exist. In addition, recall from section 4.1.2 that the observed FLRs most likely have their effective turning points well beyond the magnetopause position making reflection from a turning point within the magnetosphere unlikely.

The possibility that reflections at both the bowshock and magnetopause might result in a waveguide within the magnetosheath itself is a new idea which should be

considered. The following section is a detailed discussion of the magnetosheath waveguide model and its potential as a driving mechanism for the FLR phenomenon. The major differences between this model and that of Harrold and Samson [1992] are: reflection occurs at the magnetopause rather than a turning point in the magnetosphere; more realistic magnetosheath parameters are used; the magnetosheath eigenmodes are shown to be localized to the dusk and dawn flank regions; and the eigenmode frequencies are shown to be reasonably stable.

4.3 The Magnetosheath Waveguide Model

The basic premise of the magnetosheath model, which is sketched in Figure 4.4, is the following. A continuum of fast compressional wave energy in the solar wind is refracted at the bow shock as it enters the magnetosheath. Once in the magnetosheath, the fast waves are reflected off both the magnetopause and bow shock as they propagate downstream. Thus the magnetosheath acts like a waveguide. Now, like all waveguides, the magnetosheath will allow propagation of a continuum of fast wave modes. For a discrete set of eigenmodes to grow above the background continuum certain conditions must be met.

Consider the analogy of waves on a string. A string will resonate at certain discrete frequencies because the incident and reflected waves constructively add in such a way as to set up a standing wave pattern. In the case of the magnetosheath waveguide, the incident and reflected waves can only constructively add to become standing waves if they remain within the same region of plasma. This means that in the rest frame of the plasma the wave vector along the length of the waveguide must be small, i.e. $k_y \rightarrow 0$. Waves with large k_y values will propagate away in the plasma and will not grow above the background continuum. In the direction perpendicular to the equatorial plane, which in the model is defined as the z-direction, the situation is similar. There are no fixed reflecting boundaries so once again the eigenmodes which grow will have small k_z as well.

Although the magnetosheath eigenmodes will not propagate relative to the plasma in either the y- or z-directions, the magnetosheath plasma itself is flowing downstream at speeds ranging from ~50 km/s near local noon to ~300 km/s at the dusk and dawn flanks [Kivelson and Russell, 1995]. Given the speed of the fast mode waves in the magnetosheath plasma and the time required for the bulk plasma to flow from the

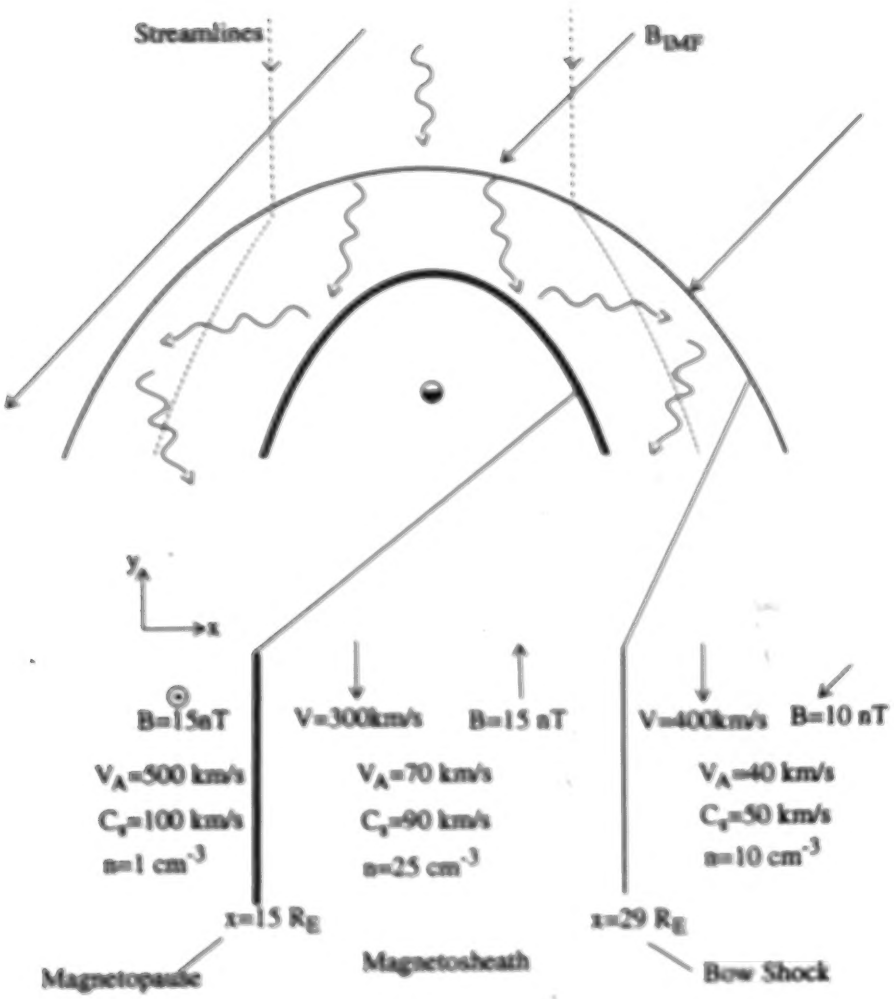

Figure 4.4. Schematic of magnetosheath waveguide model in the equatorial plane.

local noon region to the dusk or dawn flank region, the $k_y \to 0$ fast mode waves will have undergone only ~1 or 2 complete traversals of the magnetosheath from bow shock to magnetopause and back to bow shock again. Since at least one complete traversal is required before the $k_y \to 0$ waves begin to add constructively, the eigenmode standing waves are not set up until the bulk plasma reaches the flank region of the magnetosheath. Therefore, it is the plasma parameters in the flank region which determine the characteristic frequencies of the magnetosheath waveguide eigenmodes.

Typical magnetosheath plasma parameters together with those characteristic of the regions of the magnetosphere and solar wind adjacent to the flank magnetosheath are given in Figure 4.4. These plasma parameters were estimated from various sources [McKenzie, 1970; Kivelson and Russell, 1995, Gleaves and Southwood, 1991]. The bow shock position at the dusk and dawn flanks is estimated from the comprehensive study of Peredo et al. [1995] which made use of a large set of bow shock crossings observed by 17 spacecraft to explore the three-dimensional shape and location of the Earth's bow shock.

4.3.1 Fast Wave Reflection at Magnetopause and Bow Shock

The existence of magnetosheath eigenmodes requires reflection of fast magnetosonic modes at both the magnetopause and bow shock. McKenzie [1970] has derived the reflection coefficient for hydromagnetic waves at the magnetopause boundary. For the radial component of the flow perturbation and in the case of normal incidence it is given by

$$R = \frac{1 - Z}{1 + Z} \tag{4.7}$$

where

$$Z = \frac{k_{x1}^{(i)} \rho_2}{k_{x2}^{(t)} \rho_1} \tag{4.8}$$

Here $k_{x1}^{(i)}$ and $k_{x2}^{(t)}$ represent the incident and transmitted normal wave vectors which can be determined from the magnetoacoustic dispersion relation

$$k_x^2 = \frac{\omega^2}{(C_s^2 + V_A^2)} \qquad (k_y = k_z = 0) \ ; \tag{4.9}$$

ρ_1 and ρ_2 are the mass densities in the magnetosheath and magnetosphere respectively.

Using equation (4.9) together with the plasma parameter estimates given in Figure 4.4, the magnetopause reflection coefficient near the flanks is –0.75. This value increases slightly towards local noon. Thus the magnetopause does provide good reflection for fast magnetoacoustic modes in the magnetosheath.

Now consider the bow shock. The bow shock is a fast mode shock which forms in front of the Earth's magnetopause because the solar wind speed exceeds the fast mode wave speed. Whereas the magnetopause is a tangential discontinuity which allows no normal $\boldsymbol{B}$ or mass flux across it, the bow shock does allow both normal $\boldsymbol{B}$ and mass flux across it as long as they are continuous. To investigate the bow shock as a reflecting boundary the equations of reflection and refraction for hydromagnetic waves at a perpendicular shock have been derived in Appendix A. A perpendicular shock is defined as a shock in which the normal to the shock boundary is also perpendicular to the interplanetary magnetic field (i.e. $\boldsymbol{B}\cdot\boldsymbol{n}=0$). Although the angle between the bow shock and the interplanetary magnetic field varies from dawn to dusk it will be assumed that if reflection occurs at the bow shock in the perpendicular shock case then reflection will most likely occur for other bow shock angles as well. This may be justified by the fact that the derived reflection coefficients are independent of the angle between the bow shock and the interplanetary magnetic field and depend only on the magnetosonic and radial flow velocities at the bow shock.

From the derivation in Appendix A the reflection coefficient for the fast wave normal flow perturbation was found to be

$$R_{(V_x)} = \frac{\delta V_{x1}^{(r)}}{\delta V_{x1}^{(i)}} = \frac{\omega + k_{x1}^{(i)} V_{x1}}{\omega - k_{x1}^{(i)} V_{x1}} \left(\frac{2}{1 + k_{x1}^{(i)} / k_{x2}^{(i)}} - 1 \right) \tag{4.10}$$

where $k_{x1}^{(i)}$ and $k_{x2}^{(i)}$ are as defined previously and V_{x1} is the normal flow to the shock boundary on the magnetosheath side. Using the magnetosonic dispersion relation, equation (4.9), the above equation can be rewritten as

$$R_{(V_x)} = \frac{1 + V_{x1}/V_{M1}}{1 - V_{x1}/V_{M1}} \left(\frac{2}{1 + V_{M2}/V_{M1}} - 1 \right) \tag{4.11}$$

where

$$V_{M1} = \sqrt{V_{A1}^2 + C_{s1}^2}$$
$$V_{M2} = \sqrt{V_{A2}^2 + C_{s2}^2} \tag{4.12}$$

Note that V_{x1}/V_{M1} is negative since the normal flow across the bow shock is in the opposite direction to the incident normal wave vector. According to equation (4.11) the reflection coefficient at the bow shock is non-zero if V_{M1}, the fast wave speed in the magnetosheath, is different from both the fast wave speed in the solar wind, V_{M2}, and the normal flow speed to the shock boundary on the magnetosheath side, V_{x1}. Taking an average $V_{M1}$of ~180 km/s and V_{x1}~50 km/s in the magnetosheath between local noon and the flanks, and taking V_{M2}~60 km/s in the solar wind, the reflection coefficient for the normal flow perturbation of a fast wave incident on the bow shock is ~0.3. Thus it appears that fast wave modes can reflect from both the magnetopause and the bow shock allowing magnetosheath waveguide eigenmodes to grow.

4.3.2 Boundary Conditions

As discussed above the reflection coefficient at the bow shock for the normal flow perturbation is approximately 0.3. The fact that this value is positive implies that the incident and reflected perturbations are in phase and will therefore constructively add. Although the reflection at the bow shock is not perfect the in-phase reflection is a good indication that the boundary condition at the bow shock is such that the radial flow perturbation and thus the radial plasma displacement will have a maximum or antinode there. The boundary condition to be applied at the bow shock is then the open boundary condition, $\partial\xi_x/\partial x=0$, where ξ_x is the radial displacement.

At the magnetopause the situation is similar with the reflection coefficient for the radial flow perturbations having a value of ~0.75. Given this value the reflection at the magnetopause is quite strong and the reflected wave is in phase with the incident wave. Thus the magnetopause has an open boundary condition as well. An illustration of the boundary conditions at both the magnetopause and bow shock are given in Figure 4.5.

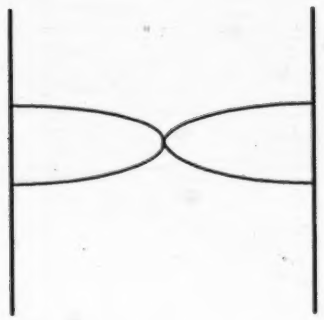

Figure 4.5. Illustration of boundary conditions at bow shock and magnetopause for the radial displacement, ξ_x.

4.3.3 Magnetosheath Eigenmode Solutions

In the magnetosheath the warm plasma equations are required to solve for the eigenmode solutions. The warm, ideal MHD equations governing the radial displacement vector, ξ_x, is given by

$$\rho_o k_{\parallel}^2 (V_p^2 - V_A^2)\,\xi_x = \frac{d}{dx}\left[\frac{\rho_o k_{\parallel}^2 (V_p^2 - V_A^2)\,(C_s^2 + V_A^2)\,(V_p^2 - C_T^2)}{k_{\perp}^2 (C_s^2 + V_A^2)\,(V_p^2 - C_T^2) - k_{\parallel}^2 (V_p^2 - V_A^2)\,(V_p^2 - C_s^2)}\right]\frac{d\xi_x}{dx}$$

$$V_p = \left(\frac{\omega - \boldsymbol{k} \bullet \boldsymbol{V}_o}{k_{\parallel}}\right) \qquad C_T^2 = \frac{C_s^2 V_A^2}{(C_s^2 + V_A^2)}\,. \tag{4.13}$$

where C_s is the sound speed, V_A is the Alfvén speed, V_o is the plasma bulk flow velocity, $\boldsymbol{k}=k_{\parallel}\boldsymbol{e}_{\parallel}+k_{\perp}\,\boldsymbol{e}_{\perp}$ ($\boldsymbol{e}_{\parallel}=\boldsymbol{Bo}/\mathrm{Bo}$, $\boldsymbol{e}_{\perp}=\boldsymbol{e}_x x \boldsymbol{e}_{\parallel}$). Note that in this magnetosheath model $\boldsymbol{e}_{\parallel}=\boldsymbol{e}_y$

and $e_\perp = e_z$. The derivation of equation (4.13) can be found in Harrold et al.[1990].

As discussed previously, the magnetosheath waveguide eigenmodes will be determined by the conditions in the flank region of the magnetosheath. Therefore it is the set of plasma parameters characteristic of the magnetosheath flank region which will be used in the determination of the eigenmode solutions. Although the plasma parameters do fluctuate somewhat across the magnetosheath flank region it is a reasonable approximation to assume average values which are constant across the sheath. With this approximation the term in brackets in equation (4.13) is constant and the equation can be simplified as

$$\frac{d^2\xi_x}{dx^2} - \kappa\xi_x = 0 \tag{4.14}$$

where

$$\kappa = k_\perp^2 - \frac{k_{||}^2 (V_p^2 - V_A^2)(V_p^2 - C_s^2)}{(C_s^2 + V_A^2)(V_p^2 - C_T^2)} . \tag{4.15}$$

This equation can be solved analytically with solutions of the form

$$\xi_x = A exp(x\sqrt{\kappa}) + B exp(-x\sqrt{\kappa}) \tag{4.16}$$

where A and B are constants determined by the boundary conditions defined in section 4.3.2. Using the magnetosheath plasma parameters defined in Figure 4.4 with $k_y = k_z = 0.001\ R_E^{-1}$, ξ_x as a function of frequency has been calculated and is shown in Figure 4.6. This figure illustrate the displacement amplitude of the eigenmode solutions in the flank region of the magnetosheath. The eigenfrequencies are apparent in the figure but can also be calculated using a phase integral approach, i.e.

$$\int_{x_{mp}}^{x_{bs}} \sqrt{\kappa} dx = n\pi , \tag{4.17}$$

where x_{bs} and x_{mp} are the radial locations of the bow shock and magnetopause, respectively. A plot of the resulting eigenfrequencies together with the plot of occurrence of observed FLR frequencies is shown in Figure 4.7. Note that the agreement between the most commonly observed FLR frequencies and the magnetosheath eigenfrequencies is very good.

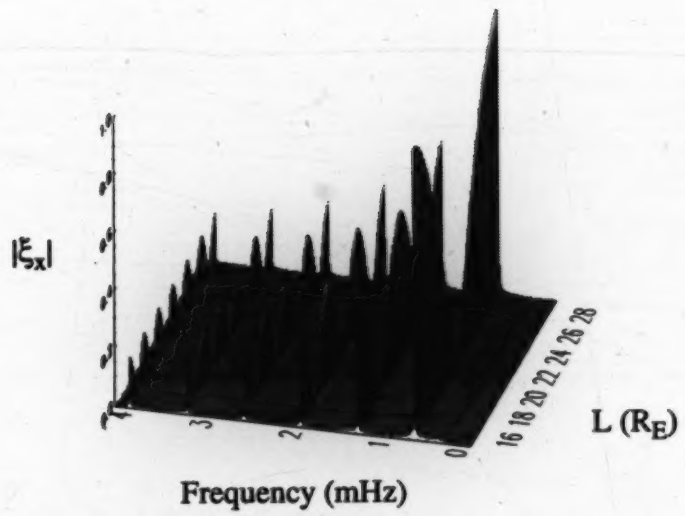

Figure 4.6. Displacement amplitude versus frequency and L value for the magnetosheath waveguide eigenmodes.

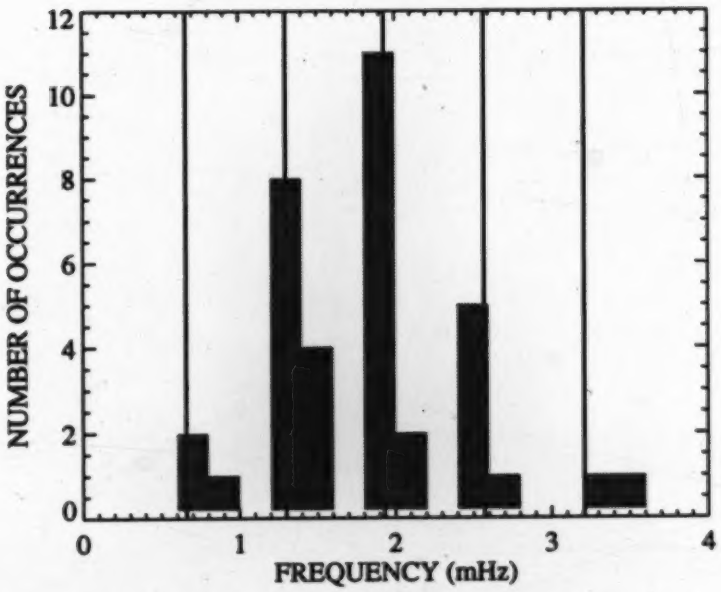

Figure 4.7. Comparison of magnetosheath eigenmode frequencies (solid lines) and observed occurrences of FLR frequencies.

4.3.4. Stability of Eigenmode Frequencies

Although the frequencies predicted by the magnetosheath model are in good agreement with observations, there is still the question of whether or not these frequencies will remain stable under various magnetosheath conditions. To test the stability of the eigenfrequencies, each of the parameters k_y, k_z, V_A, C_s, x_{bs}, and x_{mp} was varied independently of the others and the frequency variation determined. Plots of the eigenfrequency of the first 4 eigenmodes as a function of each parameter are shown in Figures 4.8-4.13. Note that for the case of small k_y, the eigenfrequencies are independent of the flow speed V_o as V_o enters the equation only through $\mathbf{k}\cdot\mathbf{V}_o=k_yV_o$.

A summary of the stability of the first eigenmode is presented in Figure 4.14 From this figure it is obvious that the magnetosheath is very dispersive, i.e. the frequencies are very sensitive to the size of k_y. However, this dispersion is irrelevant since, as discussed previously, only the small ky modes are able to add constructively and grow above the background continuum. For $k_y<0.005$ R_E^{-1} the variation in frequency is virtually non-distinguishable. Although only the small k_z solutions are relevant for the same reasons as for k_y, the frequencies are insensitive to changes in k_z.

Variations in C_s and V_A appear to render the magnetosheath unstable. However, one must also consider the possibility of a compensating effect between these speeds and the magnetopause position due to the requirement of pressure balance at the magnetopause. As an example, consider the following. The total plasma pressure which includes particle and magnetic pressures must be balanced across the magnetopause. Suppose the magnetopause is at ~15 R_E and the particle pressures on either side are equivalent with a value of ~0.35 nPa. The magnetic field strengths on either side are equivalent as well at a value of ~15 nT. Thus the total pressure is balanced across the magnetopause with a value of ~0.4 nPa. Assuming that the plasma behaves as an ideal gas, i.e. $p=nkT$, the particle pressure will vary with x in the same manner as the plasma density, temperature being approximately constant. Then taking a magnetospheric plasma density profile which varies as x^{-4} and a dipole B field, the total pressure, p^*, in the magnetosphere near the magnetopause will vary as

$$p^* = p_{mp}\left(\frac{x_{mp}}{x}\right)^4 + \frac{B_{mp}^2}{2\mu_o}\left(\frac{x_{mp}}{x}\right)^6 \qquad (4.18)$$

where the subscript mp refers to the value of that parameter at the initial magnetopause position, i.e. p_{mp}=0.35 nPa, x_{mp}=15 R_E, B_{mp}=15 nT. Now suppose that due to changes in the solar wind the plasma density and magnetic field strength in the magnetosheath

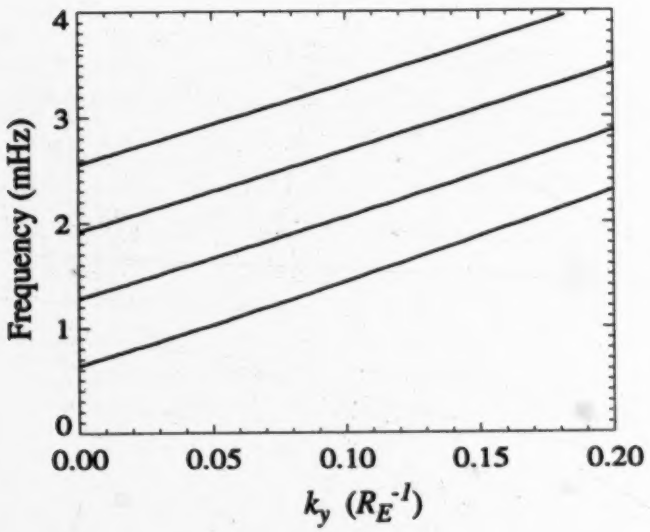

Figure 4.8. Variation of magnetosheath eigenmode frequencies as a function of k_y for the first four harmonics.

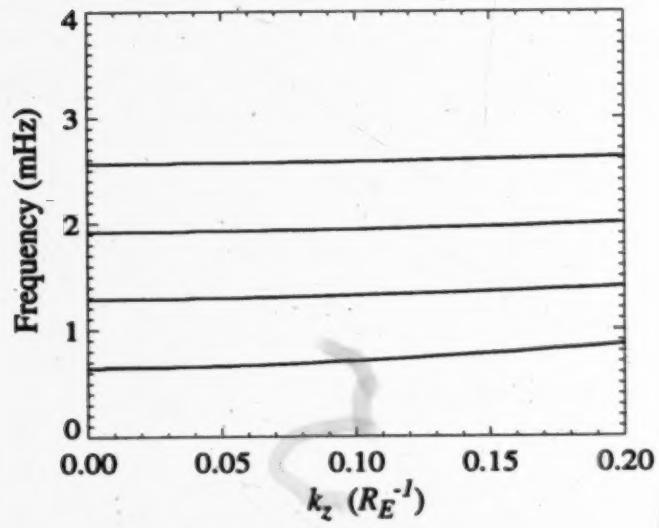

Figure 4.9. Variation of magnetosheath eigenmode frequencies as a function of k_z for the first four harmonics.

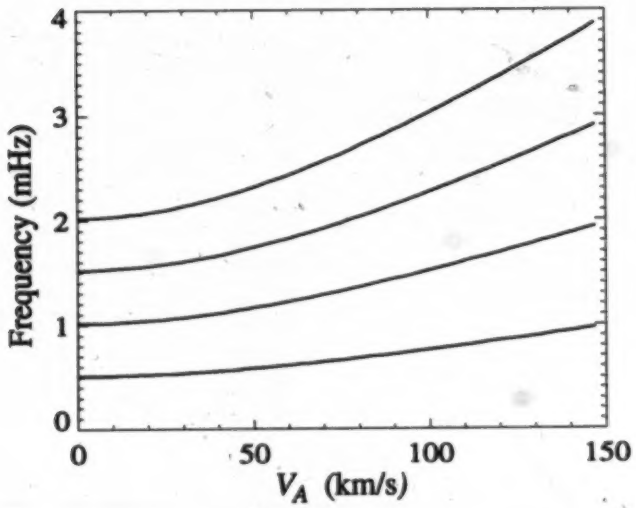

Figure 4.10. Variation of magnetosheath eigenmode frequencies as a function of V_A for the first four harmonics.

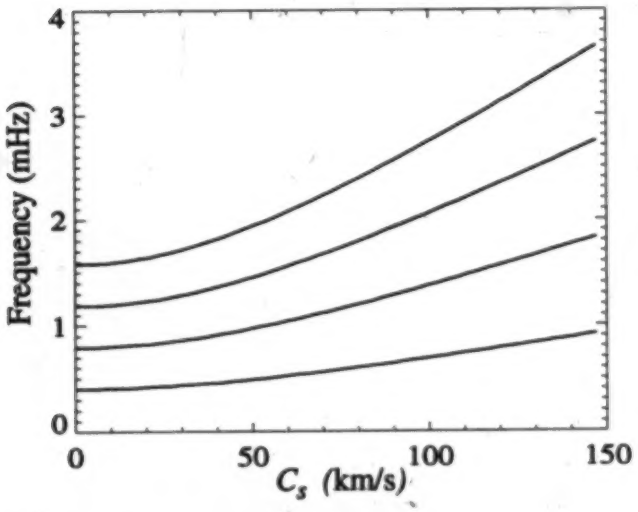

Figure 4.11. Variation of magnetosheath eigenmode frequencies as a function of C_s for the first four harmonics.

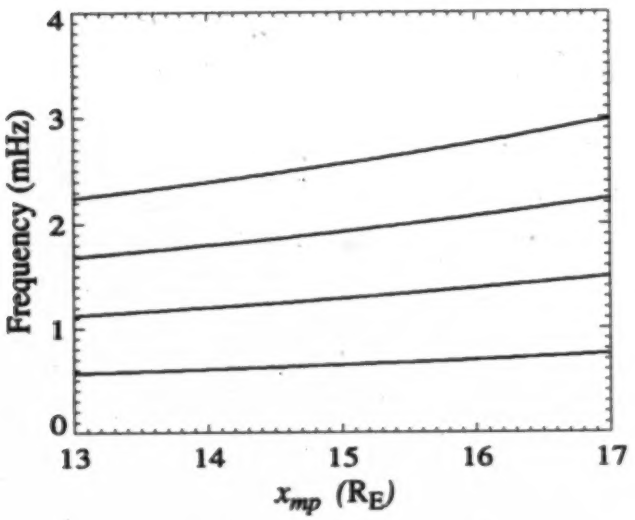

Figure 4.12. Variation of magnetosheath eigenmode frequencies as a function of x_{mp} for the first four harmonics.

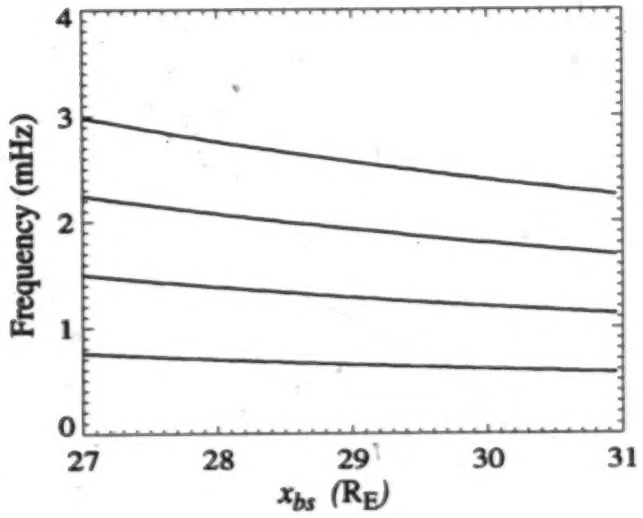

Figure 4.13. Variation of magnetosheath eigenmode frequencies as a function of x_{bs} for the first four harmonics.

both increase by 50%. This results in an increase in the total magnetosheath pressure to ~0.65 nPa. To restore pressure balance across the magnetopause the magnetopause will adjust its position until the pressure on either side is balanced. Using equation (4.18) the new magnetopause position required to satisfy pressure balance is ~13.5 R_E, a change of ~1.5 R_E from the initial position of 15 R_E. Referring to Figure 4.14, such a decrease in the magnetopause position will decrease the eigenfrequency by ~10%. However, the increase in density and magnetic field in the magnetosheath also increases V_A in the magnetosheath by ~22% which itself causes a ~10% increase in the eigenfrequency. Thus the frequency variation due to magnetopause motion is offset by the increase in V_A. A similar compensating effect would also occur for changes in C_s arising from magnetosheath temperature variations. Note that the work of Sibeck et al. [1991], which is based upon 1821 satellite crossings of the magnetopause, has shown that the magnetopause location varies by no more than ±2 R_E at the flanks.

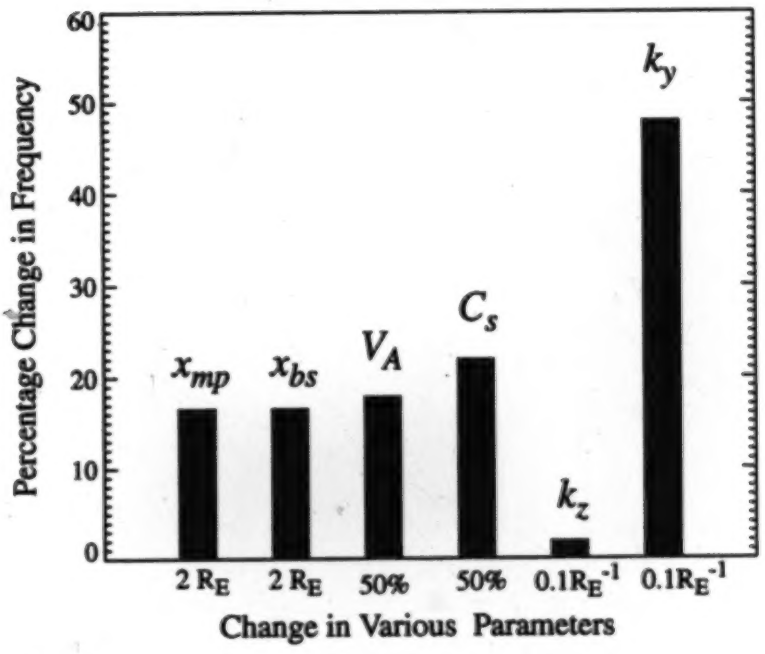

Figure 4.14. Percentage change in the frequency of the 1st eigenmode as a function of the specified changes in the various parameters.

The bow shock position unlike the magnetopause is not controlled by pressure balance but by the flow speed of the solar wind. Figure 4.15 is a plot of best fitting curves to observed bow shock locations for different ranges of Alfvénic Mach numbers, M_A, taken from Peredo et al. [1995]. This figure shows that for intermediate ranges in M_A, the bow shock position on the flanks varies by ~1 R_E at most, and in the region half-way between local noon and either flank, the bow shock position shows no variation at all. Thus, realistic variations in bow shock position should not alter the eigenfrequencies significantly.

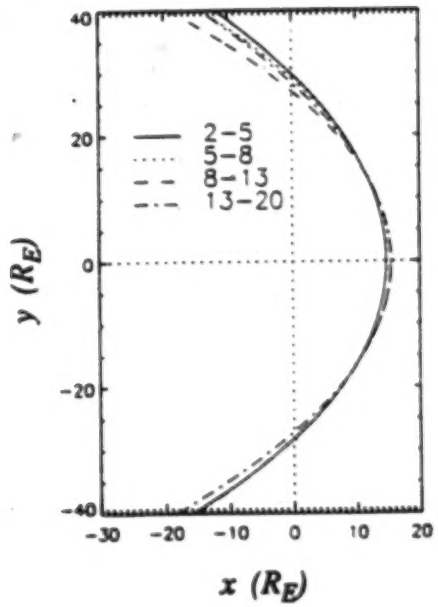

Figure 4.15. Equatorial projection of the best fitting curves for observed bow shock location for different ranges of M_A. Taken from Peredo et al. [1995].

4.3.5 Coupling of Magnetosheath Eigenmodes to FLRs

As discussed in Section 4.3.2 the magnetosheath eigenmodes have an antinode in both the radial displacement and radial flow perturbation at the magnetopause. However, there can be no normal flows across the magnetopause boundary since it is a tangential discontinuity. Thus the magnetopause will oscillate radially at the same frequencies as the magnetosheath eigenmodes to prevent any normal flow. The resulting perturbations of the magnetopause will generate fast wave modes inside the magnetosphere.

As discussed at the beginning of Section 4.3, the fast waves which generate the magnetosheath eigenmodes are those with $k_y \rightarrow 0$. Thus there is the problem as to how the magnetosheath waveguide eigenmodes can generate FLRs which have a large range of k_y values. This problem may be solved in the following way. The magnetosheath eigenmodes are localized in the flank region because of the need for successive reflections of the small k_y fast waves across the magnetosheath before the eigenmodes are generated. The result is a localized source of monochromatic waves on the flanks of the magnetosphere. The uncertainty principle tells us that the spatial localization of a wave corresponds to a broadening of the k spectrum, i.e. $\Delta x \Delta k \sim 2\pi$. Thus the eigenmode waves which are transmitted into the magnetosphere via magnetopause perturbations will have a range of k_y values while maintaining the magnetosheath eigenfrequencies.

To illustrate the coupling of the magnetosheath eigenmodes to the FLRs, Figure 4.16 is a numerical solution to the warm ideal MHD plasma equations in the box model of the magnetosphere calculated to match the eigenmode amplitudes at the magnetopause boundary. The boundary condition at the plasmapause (x=5 R_E) was taken to be $\partial \xi_x / \partial x = 0$ (or $E_x = 0$). The numerical solution was achieved using a 4^{th} order Runge-Kutta algorithm. The radial variations in magnetic field and plasma density were of the form given in equations (4.3) and (4.4), respectively. A constant sound speed value of C_s=100 km/s was used. The k_z and k_y values were varied with frequency to keep the field line resonances between ~7-12 R_E and to keep an azimuthal wave number of ~1. Thus k_z was varied from 0.015-0.15 R_E^{-1} and k_y from 0.15-0.3 R_E^{-1}. With this range of k_y, which corresponds to m values of ~1-3, the effective turning point locations all fall beyond 15 R_E and thus the solution for ξ_x shown in Figure 4.16(a) decays evanescently right from the magnetopause, till the resonances position is reached. Note that the resonance amplitudes for ξ_x are not as pronounced as those for E_x.

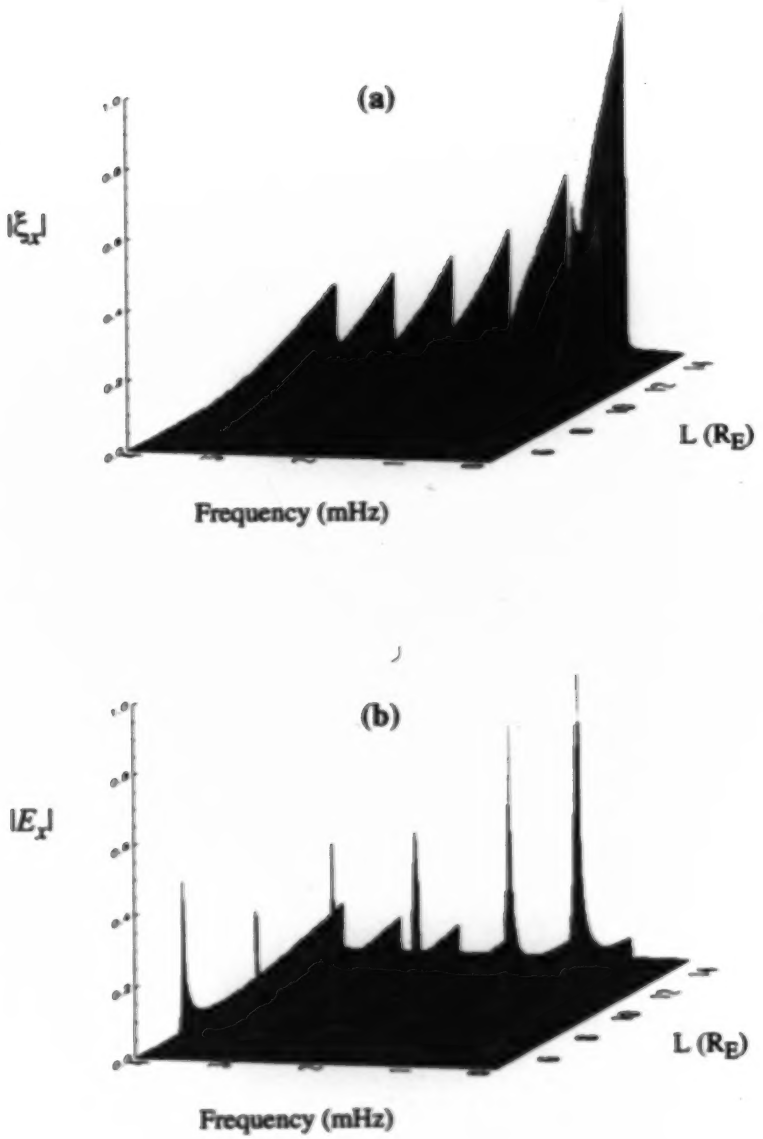

Figure 4.16. Plots of (a) $|\xi_x|$ and (b) $|E_x|$ as a function of frequency and L value calculated from numerical solutions to the warm ideal MHD equations and matching the magnetosheath eigenmode amplitudes at the magnetopause.

As shown in Figure 4.16 the eigenmodes with m values of -1 and greater will all be evanescent from the magnetopause. This result may help to explain the coupling of modes with m values greater than 2 which, according to the coupling parameter shown in Figure 1.7, should not couple very strongly. The resonant absorption as a function of the coupling parameter is based upon the fact that the fast wave is evanescent from the turning point to the resonance point. In the magnetosheath model there is no turning point and the waves are all evanescent from the magnetopause. The distance from the magnetopause to the resonance point is independent of the eigenmode m value and therefore all m value modes will evanescently decay for approximately the same distance. Thus the coupling efficiency will not decrease as quickly with m value as has been determined by the coupling parameter. Therefore eigenmodes with m values greater than 2 will be able to couple efficiently as well. Of course, for the high-m modes the coupling is not as efficient as for the low-m modes and may require an additional input of energy from an internal energy source.

4.3.6 Success of Magnetosheath Waveguide Model

As shown in Section 4.3.3 the flanks of the magnetosheath can generate a set of eigenfrequencies which are very consistent with the most commonly observed FLR frequencies. The stability of the magnetosheath eigenmode frequencies seems plausible due to the limited motion of the bow shock and the pressure balance compensation between changes in magnetosheath conditions and magnetopause position. The apparent sensitivity of the waveguide eigenfrequencies to k_y is not a problem since only the small k_y eigenmodes are able to grow above the background continuum.

The localization of the small k_y eigenmodes in the flank region results in the transmission of monochromatic waves into the magnetosphere which have a broad spectrum of k_y values. This scenario explains the observation of FLRs at the same discrete frequencies but with very different k_y values. The event of October 6, 1993 (event #5 in Table 2.1) is a good example of a FLR occurring at a fixed frequency but with a variation in k_y. The localization of the magnetosheath eigenmodes to the flank region is also consistent with the observed locations and propagation directions of the FLRs.

Considering all of the above results, the magnetosheath waveguide model seems to be very successful in its ability to explain the existence of the discrete and stable FLRs.

5

Concluding Remarks

This thesis has presented a detailed experimental and theoretical analysis of the discrete field line resonance phenomenon. This phenomenon has in the past been a somewhat controversial topic. Some in the space science community have been hesitant to accept that discrete reproducible FLRs exist at all, claiming that they are an artifact of the data analysis methods. Hopefully the work presented in this thesis will bring an end to some of this controversy.

Based upon the observational results there can be no doubt that a discrete set of FLRs does exist at both large and small azimuthal wave numbers and that the frequency spectrum is extremely reproducible from event to event. The most common frequencies are 1.3 mHz, 1.9 mHz, and 2.5 mHz with some less common frequencies such as 0.8 mHz, 1.5 mHz, and 2.2 mHz. These frequencies are distinct given that the measurement error is ±0.1 mHz. The classification of the FLRs into two distinguishable groups: low-m and high-m, is a new and interesting result which has important implications regarding the source of the discrete FLRs. Previously high-m pulsations were attributed purely to a wave-particle interaction, however, the new results presented in this thesis confirm that both the high- and low-m discrete FLRs must have the same normal mode structure ruling out a pure wave-particle interaction.

Although a wave-particle interaction is not the mechanism initiating the discrete high-m FLRs, it does provide an extra internal driver to the coupled FLR-fast-wave system, and is responsible for the different growth and latitudinal phase shift characteristics of the high-m FLRs. Although initiated by a monochromatic fast wave in the outer magnetosphere, the high-m FLRs are able to couple to an internal driver which reverses the direction of the Poynting flux. It is the direction of the Poynting flux which determines the latitudinal phase shift of the FLR. In the low-m case the Poynting flux direction is from the fast wave into the FLR and down into the resistive ionosphere and results in a phase decrease with latitude across the resonance. In the high-m case the Poynting flux direction is reversed, i.e. it points from the internal driver into the FLR and out into the fast wave. The reversal of the Poynting flux direction causes a reversal of the latitudinal phase shift such that the phase increases with latitude. The presence of the internal driver also results in a net phase change which is much greater than the standard 180°.

In marginal steady state the low-*m* resonances decay with time because the finite energy of the fast wave is continuously lost to the resistive ionosphere. However, during the initial time development of the low-m mode coupling, the FLR will grow. The high-*m* resonances, on the other hand, will grow with time because the energy originating from the internal driver accumulates in the fast wave resulting in an increase in amplitude of both the fast wave and the FLR. The initial time development of the high-*m* FLRs will not be observed because the coupling efficiency between the fast wave and the high-*m* FLR is so low. This scenario is completely consistent with the observations that the low-*m* resonances generally decay with time always exhibiting an increasing latitudinal phase shift while the high-*m* resonances always grow with time and always exhibit a decreasing latitudinal phase shift.

The fact that almost all of the observed high-*m* FLRs propagate westward with phase speeds consistent with drift speeds of ring-current protons is strong evidence that the internal driver is in the form of a drift resonance between energetic ring-current protons and a pre-existing high-*m* FLR. The amplification of the high-*m* FLRs by this internal driver mechanism also explains why the high-*m* resonances are observable at all given that the coupling efficiency between fast wave and FLR is extremely low for such large *m* values.

The observed locations and propagation directions of the FLRs, i.e. anti-sunward propagating low-*m* FLRs located at dusk and dawn and westward propagating high-*m* FLRs located in the local afternoon and early morning regions, supports a source located at the flanks of the magnetosphere. Because the high- and low-*m* FLRs share similar characteristics, the most important being the similar discrete frequency spectrum, it has been concluded that they must also share the same initial generating mechanism. Thus, any model of the source must be able to explain localization at the flanks as well as the discrete, reproducible frequency spectrum independent of azimuthal wave number and local time.

By examining the magnetospheric waveguide model in terms of its ability to satisfy the observational requirements, it has been concluded that this model is not the solution to the FLR source problem at hand. The problems involved with the magnetospheric waveguide include the following: it is too dispersive and unstable; plasma densities are too low to generate the observed frequencies; and for the FLRs of interest the turning points generally fall outside of the magnetosphere leaving no room for a waveguide. This does not mean that a magnetospheric waveguide or cavity does not exist. However, if it does, the resulting FLRs will have frequencies greater than ~5

mHz and small azimuthal wave numbers on the order of m=1. In addition, the frequencies will vary with local time and different magnetospheric conditions.

A new model, the magnetosheath waveguide model, has been proposed as a source of the discrete, reproducible FLRs. It has been shown to satisfy many of the observational constraints. Its eigenfrequencies are consistent with the most commonly observed FLR frequencies and are stable due to the limited motion of the bow shock and pressure balance compensation at the magnetopause. Dispersion in the waveguide is irrelevant since only the small k_y eigenmodes are able to grow above the background continuum. Because of the bulk plasma flow in the magnetosheath, the magnetosheath eigenmodes are localized to the flank region providing a localized source of monochromatic waves at the magnetopause which may stimulate monochromatic fast waves with a broad range of k_y values within the magnetosphere. Thus the magnetosheath waveguide is a very good candidate for the source of the discrete high- and low-m FLRs.

One point that warrants discussion is the observation of the less common FLR frequencies such as 1.5 mHz and 2.2 mHz, which are not predicted by the magnetosheath waveguide model. The fact that these frequencies were rarely found to exist independently of the more common frequencies indicates that there may be some link between them. Ziesolleck and McDiarmid [1994] suggest that they may be sidebands adjacent to the fundamental frequency peaks produced by the amplitude modulation of the wave trains. However, the fact that they are seen at latitudes intermediate to the adjacent common frequencies suggests that they are not a result of amplitude modulations but are true FLRs themselves generated by the same mechanism as the more common frequencies. If the magnetosheath model were modified to include a phase change at one of its boundaries it is possible that wave modes with a total phase change of $(2n-1)\pi$ upon one reflection back and forth across the magnetosheath might correspond to a set of odd eigenmodes consistent with the less common FLR frequencies. However, further observations and further theoretical work are required before the less common FLRs are understood.

The magnetosheath waveguide model discussed here is just a simple one-dimensional model intended to introduce the potential of the magnetosheath as the source of the FLRs and is by no means a complete theoretical treatment. Thus some future directions for this model are as follows. A two-dimensional MHD simulation of the magnetosheath would be useful to see if magnetosheath eigenmodes are in fact able to grow and localize near the dusk and dawn flanks. It would be a further challenge to

add the magnetosphere to this model and see how the eigenmodes generated in the magnetosheath are able to enter the magnetosphere and couple to the FLRs. Of course on the experimental side of things confirmation that such magnetosheath waveguide modes exist would require direct measurement of the eigenmodes. The most obvious way of making such measurements is with satellites. There have been satellite studies of magnetic pulsations in the magnetosheath [*Gleaves and Southwood*, 1991; *Hubert et al.*, 1989] but they have generally concentrated on frequencies higher than those of interest here.

With regards to the internal driver involved with the high-m FLRs, further study is required as well. Although it was suggested that the source of the internal energy was being provided by a drift resonance between the FLR and energetic ring current protons, the form of the internal driver was taken to be general and was not specific to a wave-particle interaction with the ring current. The idea that a pre-existing monochromatic FLR provides the seed for a wave-particle instability with the ring current is a new concept and will certainly be a topic of future investigation.

The primary goals of this thesis have been achieved. A solid data base from the Super Dual Auroral Radar network has been accumulated and analyzed. As discussed above the data base has provided a set of FLR characteristics from which numerous conclusions about the FLR phenomenon have been made. Solutions to perplexing problems such as the reverse latitudinal phase shift of the high-m resonances and the source of the discrete FLRs have been provided. The work presented in this thesis has not only given us a better understanding of the discrete FLR phenomenon but has also provided new insight into how energy may be transported from the solar wind to the magnetosphere and into the ionosphere.

Bibliography

Allan, W., E. M. Poulter, and E. Nielsen, STARE observations of a Pc 5 pulsation with large azimuthal wave number, *J. Geophys. Res.*, *87*, 6163, 1982.

Baker, K. B., and S. Wing, A new magnetic coordinate system for conjugate studies of high latitudes, J. Geophys. Res., 94, 9139, 1989.

Chen, L., and A. Hasegawa, A theory of long-period magnetic pulsations, 1, Steady excitation of field line resonances, *J. Geophys. Res.*, *79*, 1024, 1974.

Chen, L., A. Hasegawa, On magnetospheric hydromagnetic waves excited by energetic ring-current particles, *J. Geophys. Res.*, *93*, 8763, 1988.

Cheng et al., Ballooning-mirror instability and internally driven Pc 4-5 wave events, *J. Geomag. Geoelectr.*, *46*, 997, 1994.

Ding, D. Q., R. E. Denton, M. K. Hudson, R. L. Lysak, An MHD simulation study of the poloidal mode field line resonance in the Earth's dipole magnetosphere, *J. Geophys. Res.*, *100*, 63, 1995.

Eastman, T. E., B. Popielawska, and L. A. Frank, Three-dimensional plasma observations near the outer magnetospheric bounday, *J. Geophys. Res.*, *90*, 9519, 1985.

Fejer, B. G., and M. C. Kelley, Review of Ionospheric Irregularities, *Rev. of Geophys. and Space Phys. 18*, 401, 1980.

Fenrich, F. R., J. C. Samson, G. Sofko, R. A. Greenwald, ULF high- and low-*m* field line resonances observed with the Super Dual Auroral Radar Network, *J. Geophys. Res.*, *100*, 21535, 1995.

Forslund, D., J. M. Kindel, K. Lee, E. L. Lindman, and R. L. Morse, Theory and simulation of absorption in a hot plasma, *Phys. Rev. A*, *11*, 679, 1975.

Gleaves, D. G., and D. J. Southwood, Magnetohydrodynamic fluctuations in the Earth's magnetosheath at 1500 LT: ISEE 1 and ISEE 2, *J. Geophys. Res.*, *96*, 129, 1991.

Grant, I. F., D. R. McDiarmid, and A. G. McNamara, A class of high-*m* pulsations and its auroral radar signature, *J. Geophys. Res.*, *97*, 8439, 1992.

Greenwald, R. A., K. B. Baker, J. R. Dudeney, M. Pinnock, T. B. Jones, E. C. Thomas, J.

-P. Villain, J. -C. Cerisier, C. Senior, C. Hanuise, R. D. Hunsucker, G. Sofko, J. Koehler, E. Nielsen, R. Pellinen, A. D. M. Walker, N. Sato, H. Yamagushi, DARN/ SUPERDARN A global view of the dynamics of high-latitude convection, *Space Sci. Rev., 71*, 761, 1995.

Harrold, B. G., C. K. Goertz, R. A. Smith, and P. J. Hansen, Resonant Alfvén wave heating of the plasma sheet boundary layer, *J. Geophys. Res., 95*, 15039, 1990.

Harrold, B. G., J. C. Samson, Standing ULF Modes in the magnetosphere: A theory, *Geophys. Res. Lett., 19*, 1811, 1992.

Hasegawa, A., Drift mirror instability in the magnetosphere, *Phys. Fluids, 12*, 2642, 1969.

Hubert, D., C. C. Harvey, and C. T. Russell, Observations of magnetohydrodynamic modes in the Earth's magnetosheath at 0600 LT, *J. Geophys. Res., 94*, 17305, 1989.

Kivelson, M. G., J. Etcheto, and J. B. Trotignon, Global compressional oscillations of the terrestrial magnetosphere: The evidence and a model, *J. Geophys. Res., 89*, 9851, 1984.

Kivelson, M. G., and D. J. Southwood, Resonant ULF waves: A new interpretation, *Geophys. Res. Lett., 12*, 49, 1985.

Kivelson, M. G., and D. J. Southwood, Coupling of global magnetospheric MHD eigenmodes to field line resonances, *J. Geophys. Res., 91*, 4345, 1986.

Kivelson, M. G. and C. T. Russell, Eds., *Introduction to Space Physics*, Cambridge University Press, New York, 1995.

Kremser, G., A. Korth, J. A. Fejer, B. Wilken, A. V. Gurevich, and E. Amata, Observations of quasi-periodic flux variations of energetic ions and electrons associated with Pc 5 geomagnetic pulsations, *J. Geophys. Res., 86*, 3345, 1981.

Lin, C. S. and G. K. Parks, The coupling of Alfvén and compressional waves, *J. Geophys. Res., 83*, 2628, 1978.

McDiarmid, D. R., T. K. Yeoman, I. F. Grant, and W. Allan, Simultaneous observation of a traveling vortex structure in the morning sector and a field line resonance in the postnoon sector, *J. Geophys. Res. 99*, 8891, 1994.

McKenzie, J. F., Hydromagnetic wave interaction with the magnetopause and the bow shock, *Planet. Space Sci., 18,* 1, 1970.

McPherron, R. L., Magnetospheric dynamics, in *Introduction to Space Physics*, Cambridge University Press, New York, 1995.

Nielsen, E., and W. Allan, A double-resonance Pc 5 pulsation, *J. Geophys. Res., 88,* 5760, 1983.

Parker, E. N., Dynamics of the interplanetary gas and magnetic fields, *Astrophys. J., 128,* 664, 1958.

Parks, G. K., *Physics of Space Plasmas an Introduction*, Addison-Wesley Publishing company, Redwood City, 1991.

Peredo, M., J. A. Slavin, E. Mazur, and S. A. Curtis, Three-dimensional position and shape of the bow shock and their variation with Alfvénic, sonic and magnetosonic Mack numbers and interplanetary magnetic field orientation, *J. Geophys. Res., 100,* 7907, 1995.

Poulter, E. M., Pc 5 micropulsation resonance regions observed with the STARE radar, *J. Geophys. Res., 87,* 8167, 1982.

Prikryl, P., R. A. Greenwald, G. J. Sofko, J. P. Villain, and C. W. S. Ziesolleck, Observations of solar-wind-driven field line resonances and ionospheric flows in the cusp/cleft, SuperDARN Annual Meeting, Ellicott City, MD, 1996.

Rankin, R., B. G. Harrold, J. C. Samson, and P. Frycz, The nonlinear evolution of field line resonances in the Earth's magnetosphere, *J. Geophys. Res., 98,* 5839, 1993.

Ruohoniemi, J. M., R. A. Greenwald, K. B. Baker, J. P. Villain, M. A. McCready, Drift motions of small-scale Irregularities in the high-latitude F region: an experimental comparison with plasma drift motions, J. Geophys. Res., 92, 4553, 1987.

Ruohoniemi, J. M., R. A. Greenwald, and K. B. Baker, HF radar observations of Pc 5 field line resonances in the midnight/early morning MLT sector, *J. Geophys. Res., 96,* 15697, 1991.

Samson, J. C., R. A. Greenwald, J. M. Ruohoniemi, T. J. Hughes, and D. D. Wallis, Magnetometer and radar observations of MHD cavity modes in the Earth's

magnetosphere, *Can J. Phys., 69*, 929, 1991.

Samson, J. C., D. D. Wallis, T. J. Hughes, F. Creutzberg, J. M. Ruohoniemi, and R. A. Greenwald, Substorm intensifications and field line resonances in the nightside magnetosphere, *J. Geophys. Res. 97*, 8495, 1992a.

Samson, J. C., B. G. Harrold, J. M. Ruohoniemi, R. A. Greenwald, and A. D. M. Walker, Field line resonances associated with MHD waveguides in the magnetosphere, *Geophys. Res. Lett., 19*, 441, 1992b.

Samson, J. C., L. L. Cogger, Q. Pao, Observations of field line resonances, auroral arcs, and auroral vortex-structures, *J. Geophys. Res.*, 101, 17373, 1996.

Sibeck, D. G., R. E. Lopez, and E. C. Roelof, Solar wind control of the magnetopause shape, location and motion, *J. Geophys. Res., 96*, 5489, 1991.

Southwood, D. J., Some features of field line resonances in the magnetosphere, *Planet. Space Sci., 22*, 483, 1974.

Southwood, D. J., A general approach to low-frequency instability in the ring current plasma, *J. Geophys. Res., 81*, 3340, 1976.

Speziale, T., and P. J. Catto, Linear wave conversion in an unmagnetized, collisionless plasma, *Phys. Fluids, 20*, 990, 1977.

Tamao, T., Transmission and coupling resonance of hydromagnetic disturbances in the non-uniform Earth's magnetosphere, Sci. Rep. Tohoku Univ., Ser. 5, 17, 43, 1966.

Tian, M., T. K. Yeoman, M. Lester, and T. B. Jones, Statistics of Pc5 pulsation events observed by SABRE, *Planet. Space Sci., 39*, 1239, 1991.

Tsyganenko, N. A., Global quantitative models of geomagnetic field in the cislunar magnetosphere for different disturbance levels, *Planet. Space Sci., 35*, 1347, 1987.

Waldock, J. A., T. B. Jones, E. Nielsen, and D. J. Southwood, First results of micropulsation activity observed by SABRE, *Planet. Space Sci., 31*, 573, 1983.

Walker A. D. M., R. A. Greenwald, W. F. Stuart, and C. A. Green, STARE auroral radar observations of Pc 5 geomagnetic pulsations, *J. Geophys. Res., 84*, 3373, 1979.

Walker, A. D. M., R. A. Greenwald, A. Korth, and G. Kremser, STARE and GEOS 2 observations of a storm time Pc 5 pulsation, *J. Geophys. Res., 87*, 9135, 1982.

Walker, A. D. M., J. M. Ruohoniemi, K. B. Baker, R. A. Greenwald, Spatial and temporal behavior of ULF pulsations observed by the Goose Bay HF radar, *J. Geophys. Res., 97*, 12187, 1992.

Walker, A.D.M., Theory of magnetospheric standing hydromagnetic waves with large azimuthal wave number, 3, Particle resonance and instability, *J. Geophys. Res., 99*, 11105, 1994.

Waters, C. L., J. C. Samson, E. F. Donovan, The temporal variation of the frequency of high latitude field line resonances, *J. Geophys. Res., 100*, 7987, 1994.

Woch, J., G. Kremser, A. Korth, A comprehensive investigation of compressional ULF waves observed in the ring current, *J. Geophys. Res., 95*, 15113, 1990.

Wright, A. N., Dispersion and wave coupling in inhomogeneous MHD waveguides, *J. Geophys. Res., 99*, 159, 1994.

Yeoman, T. K., M. Tian, M. Lester, and T. B. Jones, A study of Pc 5 hydromagnetic waves with equatorward phase propagation, *Planet. Space Sci., 40*, 797, 1992.

Ziesolleck, C. W. S., and D. R. McDiarmid, Auroral latitude Pc 5 field line resonances: Quantized frequencies, spatial characteristics, and diurnal variation, *J. Geophys. Res., 99*, 5817, 1994.

Appendix A

Reflection and Transmission at a Perpendicular Shock

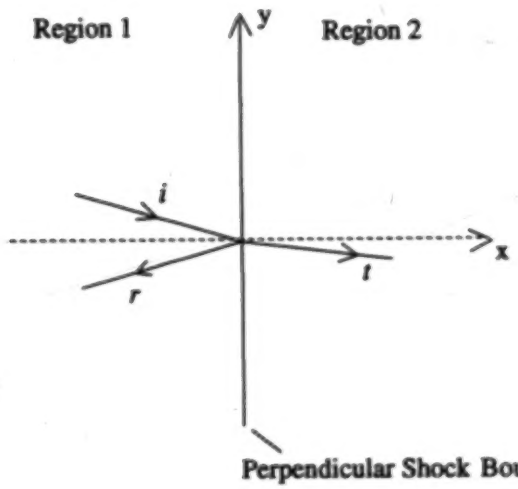

Consider the reflection and refraction of a fast magnetoacoustic wave at a perpendicular shock boundary such as the dusk bowshock. If there is reflection, the impinging wave (denoted by the superscript i) will give rise to both a reflected wave (denoted by r) and a transmitted wave (denoted by t). As discussed in Chapter 4, the magnetosheath eigenmodes will have small k_y and k_z. Therefore, in the following derivation it will be assumed that k_y and k_z are zero. At a perpendicular shock the following boundary conditions hold.

Normal magnetic field is zero on both sides:

$$B_{n1} = B_{n2} = 0 \,. \tag{A.1}$$

Mass flux is conserved across the boundary:

$$[\rho V_n] = 0 \,. \tag{A.2}$$

Momentum is conserved across the boundary:

$$\left[\rho\,(V\bullet n)\,V+\left(p+\frac{B^2}{2\mu_o}\right)n-\frac{B_nB}{\mu_o}\right]=0\ . \tag{A.3}$$

In the above equations n is the normal vector to the boundary surface and the square brackets [] represent the difference between that quantity on either side of the boundary.

The amplitudes of the reflected and transmitted waves can now be determined by applying the above conditions. Assuming small perturbations and linearizing, these become:

$$\delta B_{x1}^{(i)}+\delta B_{x1}^{(r)}=\delta B_{x2}^{(t)}=0 \tag{A.4}$$

$$V_{x1}(\delta\rho_1^{(i)}+\delta\rho_1^{(r)})+\rho_1(\delta V_{x1}^{(i)}+\delta V_{x1}^{(r)})=V_{x2}\delta\rho_2^{(t)}+\rho_2(\delta V_{x2}^{(t)}) \tag{A.5}$$

$$\begin{aligned}&\delta p_1^{(i)}+\delta p_1^{(r)}+V_{x1}^2(\delta\rho_1^{(i)}+\delta\rho_1^{(r)})+2\rho_1V_{x1}(\delta V_{x1}^{(i)}+\delta V_{x1}^{(r)})\\&+B_{y1}(\delta B_{y1}^{(i)}+\delta B_{y1}^{(r)})=\delta p_2^{(t)}+V_{x2}^2\delta\rho_2^{(t)}+2\rho_2V_{x2}\delta V_{x2}^{(t)}+B_{y2}\delta B_{y2}^{(t)}\end{aligned} \tag{A.6}$$

where $\delta\rho$, δp, δB_x and δV_x are, respectively, the perturbed amplitudes of mass density, pressure, and the x components of magnetic field and fluid velocity. Note that only the normal part of (A.3) has been used in (A.6).

The x-component of the momentum equation given by

$$\rho\delta V_x(\omega-k_xV_x)=k_x(\delta p+\frac{B\bullet\delta B}{\mu_o}) \tag{A.7}$$

holds for each plane wave (incident, transmitted, and reflected) thus providing 3 additional equations. Similarly, the continuity equation

$$\frac{\omega}{k_x}\delta\rho=V_x\delta\rho+\rho\delta V_x \tag{A.8}$$

also provides 3 more equations, one for each plane wave. Substituting equation (A.7)

into (A.6) and using $k_{xl}^{(r)}=-k_{xl}^{(i)}$ yields:

$$\frac{\rho_1\omega}{k_{x1}^{(i)}}(\delta V_{x1}{}^{(i)}-\delta V_{x1}{}^{(r)})+V_{x1}(\rho_1(\delta V_{x1}^{(i)}+\delta V_{x1}^{(r)})+V_{x1}(\delta\rho_1^{(i)}+\delta\rho_1^{(r)}))$$

$$=\frac{\rho_2\omega}{k_{x2}^{(i)}}\delta V_{x2}{}^{(i)}+V_{x2}(\rho_2\delta V_{x2}^{(i)}+V_{x2}\delta\rho_2^{(i)}) \qquad \text{(A.9)}$$

Now, substituting (A.8) into (A.5) gives:

$$(\delta\rho_1^{(i)}-\delta\rho_1^{(r)}) = \frac{k_{x1}^{(i)}}{k_{x2}^{(i)}}(\delta\rho_2^{(i)}) \qquad \text{(A.10)}$$

and substituting (A.8) into (A.9) gives:

$$(\delta\rho_1^{(i)}+\delta\rho_1^{(r)}) = \left(\frac{k_{x1}^{(i)}}{k_{x2}^{(i)}}\right)^2(\delta\rho_2^{(i)}) \cdot \qquad \text{(A.11)}$$

Solving these two equations, (A.10) and (A.11), for the reflection coefficient for the density perturbation, R_ρ, defined by

$$R_{(\rho)} = \frac{\delta\rho_1^{(r)}}{\delta\rho_1^{(i)}} \qquad \text{(A.12)}$$

and the transmission coefficient for the density perturbation, T_ρ, defined by

$$T_{(\rho)} = \frac{\delta\rho_2^{(i)}}{\delta\rho_1^{(i)}} \qquad \text{(A.13)}$$

yields:

$$R_{(\rho)} = 1-\frac{2}{1+k_{x1}^{(i)}/k_{x2}^{(i)}}$$

$$T_{(\rho)} = \frac{2}{(k_{x1}^{(i)}/k_{x2}^{(i)})\,(1+k_{x1}^{(i)}/k_{x2}^{(i)})} \qquad \text{(A.14)}$$

Using equation (A.8) and the above relations for R_ρ and T_ρ, the reflection and transmission coefficients for the perturbed flow can be determined to be

$$R_{(V_x)} = \left(\frac{\omega + k_{x1}^{(i)} V_{x1}}{\omega - k_{x1}^{(i)} V_{x1}}\right)\left(\frac{2}{1 + k_{x1}^{(i)}/k_{x2}^{(i)}} - 1\right)$$

$$T_{(V_x)} = \left(\frac{\rho_1 k_{x1}^{(i)}}{\rho_2 k_{x2}^{(i)}}\right)\left(\frac{\omega - k_{x2}^{(i)} V_{x2}}{\omega - k_{x1}^{(i)} V_{x1}}\right)\left(\frac{2}{(k_{x1}^{(i)}/k_{x2}^{(i)})\,(1 + k_{x1}^{(i)}/k_{x2}^{(i)})}\right) \qquad \text{(A.15)}$$

In the above equations, k_x on either side of the shock boundary must satisfy the following dispersion relation

$$k_x^2 = \frac{\omega^2}{(C_s^2 + V_A^2)} \qquad (k_y = k_z = 0)\,. \qquad \text{(A.16)}$$